UNIVERSITY OF CALIFORNIA

Santa Barbara

# The Study of Excited-State Intramolecular Charge Transfer in Organic Molecules and the Development of a Novel Sub-Micron Sampling and Offline Chemical Analytical Technique

A dissertation submitted in partial satisfaction of the

requirements for the degree Doctor of Philosophy

in Chemistry

by

Trevor Elijah Cohen

Committee in charge:

Professor Mattanjah de Vries, Chair

Professor Michael Gordon

Professor Steven Burrato

Professor Songi Han

Professor Peter Ford

September 2023

The dissertation of Trevor Elijah Cohen is approved.

_____

Peter Ford

_____

Songi Han

_____

Steven Burrato

_____

Michael Gordon

_____

Mattanjah de Vries, Committee Chair

September 2023

The Study of Excited-State Intramolecular Charge Transfer in Organic Molecules and the Development of a Novel Sub-Micron Sampling and Offline Chemical Analytical Technique



by

Trevor Elijah Cohen

ACKNOWLEDGEMENTS

It is tough to put into words how grateful I am for the community of people in my life that have helped me become the scientist I am today. To my parents who have supported me throughout my entire life and have always diligently tried to understand my research. To my partner, Jess, who has been a person who I could always lean on when the times are tough and excited to celebrate me when I succeed. To Mattanjah and Mike, thank you for always providing constructive guidance on the research I performed. To Greg, Michael, and Jake, who have mentored me on the skills necessary to efficiently perform research as well have helped guide me in professional development. To Nathan, who without his vast knowledge of the instruments in the lab, I would not have been able to successfully complete the projects I did at such a fast rate. And to the many undergraduates and newer graduate students, especially Charlie, Ana, and Julia, who helped in the lab and that assisted me in my academic research.

VITA OF Trevor Elijah Cohen (He/Him)
September 2023

## SUMMARY

Chemistry Ph.D. candidate in his 5th year graduating in August looking to join a collaborative environment to contribute to the development of novel optics and photonics. Expertise in performing tandem gas phase spectroscopy and mass spectrometry under ultra-high vacuum systems measuring the excited state dynamics of large organic molecules. Extensive experience developing a novel sub-micron surface sampling technique and other laser-based experiments from the ground up to characterize and measure surface properties of various materials. Served as interim facility manager of the core mass spectrometry facility in the Department of Chemistry where he was involved in the running of the facility and responsible for characterizing various sample types.

## RESEARCH & PROFESSIONAL EXPERIENCE

**University of California Santa Barbara de Vries Lab** (Santa Barbara, CA)

*Gas Phase Spectroscopist* January 2018 - Expected August 2023

- Proposed and performed gas phase multi-photon spectroscopic studies which required routine alignment of up to 4 pulsed lasers to measure tautomer specific high resolution vibronic transitions and the excited state dynamics of large organic molecules.
- Configured optical layouts and laser parameters such as wavelength, power, and beam shape to enable collaborators at the university to perform considerably different photo-induced materials evolution studies and optical device characterization from high-powered laser lift off to low powered lasing experiments.-Crucial for the optical experiments described. I am capable of very precise alignment and tuning of laser systems as well as optics choice for the most efficient experiments.
- Extensive experience running, maintaining, repairing, and acquiring data with high-powered pulsed laser systems, ultra-high vacuum systems, time-of-flight mass spectrometers, and high voltage electronics.-Have spent many weeks fixing vacuum systems, leak detecting, troubleshooting etc. Capable of interpreting data from complex experiments such as excited-state dynamics studies.
- Acquired specialization in manipulating lasers in time and space to optimally interact with analytes moving at supersonic speeds entrained in a cold gas.-Crucial not for my ability to hit fast targets, but to work with lasers in high vacuum systems.
- Designed new experiments that required multiple beams of different wavelength to be collinear and temporally synchronized by controlling polarization and beam diameter through telescoping and focusing, using accumulated knowledge of various optics materials such as dichroics, metals, and fused silica from the deep UV to NIR for μJ to mJ powers. -Can talk about here having to design intricate beam paths so

that beams from multiple sources can reach the destination at the same time. Alignment of mechanical delay stages for example. Precise detection with photodiode detectors and oscilloscopes.

- Proficiency in tuning non-linear optics to produce up to the 5$^{th}$ harmonic wavelength of Nd:YAG lasers and optimization of broadband OPO/OPA systems. -Can talk here learning from field technicians that came to tune our laser systems and then being able to apply things I picked up from them to detect where problems are occurring as well as how to tune the optics. Used 5$^{th}$ harmonic generators for my spectroscopic studies almost daily. Worked on the restoration of a broken OPO/OPA system in the lab. Required understanding of each component of the optical layout and their purpose.
- Obtained experience and knowledge in laser engineering and optics theory such as q-switching and collimating a beam as well as spectroscopy techniques in the solution and gas phase from the nano to femtosecond time scale. -I imagine my know-how of laser theory will be useful when consulting on the types of experiments we need to run as well as fine tuning experiments on the spot.
- Gained experience using Labview, Mathematica, Origin, and Python for data acquisition, analysis, and exponential decay fitting for detailed reporting of findings.

*Novel Development of Tip Enhanced Laser Desorption* January 2018 - Expected August 2023

- Developed a state-of-the-art sub-micron surface sampling technique that required devising an optical layout that most efficiently delivers a high-powered laser pulse to a nanoscopic AFM probe.
- Investigated the underlying mechanism of Tip Enhanced Laser Desorption by performing a multitude of studies varying different materials and laser parameters such as focus, pulse width, and wavelength.-Both of these points compliment my previous thoughts. Shows flexibility in the type of laser experiments I can perform. Very different purpose and therefore required a different process to produce results. More beam manipulation skills hitting an AFM probe with a laser.
- Created image analysis protocols to measure the craters produced post desorption using Gwyddion.

**University of California Santa Barbara Mass Spectrometry Facility**

*Interim Facility Manager* August 2021 -December 2022

- Prepared and ran GC-MS and MALDI-MS samples ranging from small organic molecules to large biomolecules such as polymers and proteins for research groups.
- Consulted with research groups at UCSB and local private companies to optimize sample preparation and characterization techniques for their projects resulting in publication acknowledgement.

**Scientific Presentations**

- JSU-UCSB Workshop on Gas Phase Spectroscopy and Theoretical Approaches January 2017: "*The Role of Isocytosine and Isoguanine on an Early Earth"*
- University of California Chemical Symposium 2020: "The Development of Tip Enhanced Laser Desorption for Spatially Resolved Sampling and Analysis"
- Summer ACS 2020 Conference: Poster Presentation: "The Development of Tip Enhanced Laser Desorption for Spatially Resolved Sampling and Analysis"
- Spectroscopy and Dynamics 2022: *"The Effects of Deuteration on the Excited State Hydrogen Transfer of Indigo in the Gas Phase"*

**Summer JUMP Program, UC Santa Barbara, de Vries Lab**

*Research Mentor* June 2019 - Present

- Mentored and lead undergraduate researchers from Jackson State University through research and guided in the creation of experiments and projects.

**Summer Institute in Mathematics and Science, UCSB CSEP**

*Resident and Research Assistant* August 2018

- Prepared summer interns to give a research presentation to a scientific audience.
- Guided discussions on how to succeed as an undergraduate at UCSB, tutored students, and acted as a liaison between individual students and their graduate student mentors.

**EDUCATION**

---

**University of California, Santa Barbara** (Santa Barbara, CA)

*M.S./Ph.D. in Physical Chemistry* September 2018-Expected May 2023

- Service to the Department of Chemistry, 2020 and 2022

*B.S. in Chemistry from the College of Creative Studies* October 2014 - June 2018

- Norman F. Sprague III Fellow SURF scholar, 2017

**PUBLICATIONS**

---

1. Cohen, T.; Svadlanak, N.; Kincaid, J.; Smith, C.; Lipshutz, B.; Rode, T.; de Vries, M. S., *"The Effects of Deuteration on the Excited State Hydrogen Transfer of Indigo in the Gas Phase"*
2. Cohen, T.; Parejo, A.;de Vries, M. S.; Gordon, M. J., *Spatially resolved surface sampling using Tip Enhanced Laser Desorption for ex-situ analysis* (In Preparation)
3. Cohen, T.; Didziulis, J.; Parejo, A.; Szabla, R.; de Vries, M. S., *"The Excited State Dynamics of Guanosine, Adenosine, and their Analogues"* (In Preparation)

4. Cohen, T.; Parejo, A.; Didziulis, J.; Szabla, R.; de Vries, M. S., *"The Excited State Dynamics of 6,6'-Dibromoindigo: Exploring how Tyrian Purple has Survived on Art the Ages"* (Submitted)

5. Svadlanak, N.; Cohen, T.; Parejo, A.; de Vries, M. S., *"Conformer selective photodissociation in FGG tripetide ions"* (Manuscript Written)
6. Li, P.; Zhang, H.; Li, H.; Cohen, T.; Anderson, R.; Wong, M.; Trageser, E.; Chow, Y. ; De Vries, M. S.; Nakamura, S.; DenBaars, *"Demonstration of Yellow (568 nm) Stimulated Emission from Optically Pumped InGaN/GaN Multi-Quantum Wells.* Applied Physics Letters: **2022**
7. Berenbeim, J. A.; Boldissar, S.; Siouri, F. M.; Gate, G.; Haggmark, M. R.; Aboulache, B.; Cohen, T.; de Vries, M. S., Excited State Intramolecular Proton Transfer in Hydroxyanthraquinones: Toward Predicting Fading of Organic Red Colorants in Art. Science Advances: **2019**
8. Berenbeim, J. A.; Boldissar, S.; Siouri, F. M.; Gate, G.; Owens, S; Haggmark, M. R.; Cohen, T.; Rode, M.F.; Patterson, C. Shmidt; de Vries, M. S., Excited-State Dynamics of Isocytosine: A Hybrid Case of Conical Nucleobase Photodynamics. The Journal of Physical Chemistry Letters: **2017**

ABSTRACT

The Study of Excited-State Intramolecular Charge Transfer in Organic Molecules and the Development of a Novel Sub-Micron Sampling and Offline Chemical Analytical Technique

by

Trevor Elijah Cohen

A molecule's ability to survive upon irradiation is intrinsically tied to how quickly it can release the energy it has absorbed, as prolonged excitation leads to damaging reactions with its surroundings. To probe how unique structural moieties of various biomolecules and organic dye molecules mechanistically relax after photoexcitation in a solvent-free environment, Resonance Enhanced Multi-Photon Ionization (REMPI) was used. REMPI is a powerful spectroscopy technique that describes photon events involving two to three photons sequentially absorbed by the sample to excite and ionize the molecule of interest along various trajectories. These spectroscopic studies employ lasers ranging from the UV-IR with either picosecond or nanosecond pulse width to analyze the absorption spectrum, tautomeric structure, and the excited-state dynamics of the molecules. In collaboration with theoretical calculations modelling the excited-state potential energy surface and dynamics, it becomes possible to draw conclusions on how electronically and structurally a molecule relaxes.

Upon excitation, a molecule can utilize various mechanisms to reach the ground state. For example, the canonical nucleobases utilize fast internal conversion to reach conical

intersections leading back to the ground state. A study of the alternative nucleobase, isocytosine, was performed comparing its dynamics to guanine and cytosine. Another relaxation mechanism used is excited-state intramolecular hydrogen, proton, and charge transfer (ESIHT, ESIPT, and ESICT respectively), which describes the movement of a charge or hydrogen atom from a donor to acceptor site. This process produces new photoproducts, each with new available relaxation pathways to the ground state. Intramolecular charge and atom transfer are typically ultrafast processes and are too fast to measure with the picosecond laser systems available but are slowed by several orders of magnitude when quantum tunneling is involved. Measurements of the photoproducts post transfer can also provide insight into the mechanism. These studies focus on how various structural moieties in organic dyes, nucleosides, and polypeptides and substituents such as methylation, deuteration, halogenation, and changes in secondary structure affect the rate of excited-state intramolecular transfer. Selective placement of the substituent groups at or near the transfer site provides precise control of the dynamics that when combined with theoretical calculations can develop detailed models of the mechanism.

REMPI is a powerful chemical characterization tool that provides both highly specific mass, absorption, and structural information of a sample. However, the technique cannot distinguish spatial features on the surface of the sample material. The development of a novel sub-micron sampling technique, Tip Enhanced Laser Desorption (TELD), is described below. TELD is an off-line sampling process in which a sample is first imaged with an AFM, then a laser is focused and fired at the probe desorbing the surface beneath it, and then the vaporized material is collected and redeposited onto a new substrate for further analysis. Separation of the sampling and chemical characterization techniques results in independent

optimization of the samples collected depending on the analytical technique chosen. Detailed experiments into various parameters of the technique such as laser power, number of pulses fired, tip material, and the forced applied between the tip and surface providing insight into the underlying mechanism of energy transfer.

The synthesis and characterization of InGaN multi-quantum wells and the lasing wavelength of the material was also studied. Pumping of the material with a 355 nm pulsed laser revealed a pumping threshold of 1.5 $MW/cm^2$ and a lasing wavelength of 568 nm, a spectral region previously not producible with semi-conducting laser materials.

TABLE OF CONTENTS

# I. Introduction

Electromagnetic radiation produced by the sun is both necessary for life and the production of organic compounds, but also can cause irreparable damage to these biomolecules. Similarly, materials such as dyes and pigments cannot be colored without absorbing potentially harmful light. As such, the structure of these molecules must strike a balance between functionality and a molecule's ability to release energy post photo absorption.

Spectroscopy is a powerful tool that illuminates the structural moieties of a molecule influence the trajectories available to reach the ground state. Use of IR and Raman spectroscopy, for example can unveil through measurements of the vibrational modes of the molecule, the conformers present in the experiment. Upon vibronic photoexcitation, molecules perform various processes to return to the ground state often at ultrafast timescales. To characterize these fast interactions, such as fluorescence or the contortions of a heterocycle, equally fast and sensitive tools are necessary to observe these dynamic events. One such method capable of measuring these excited-state dynamics is Resonance Enhanced Multi-Photon Ionization (REMPI). REMPI is a multi-faceted technique capable of characterizing and measuring the dynamics of a gaseous sample cooled to approximately 15 K through stepwise excitation, ionization, and detection in a time-of-flight mass spectrometer. Through careful selection of wavelength and pulse width of the lasers used for excitation and ionization, it is possible to measure the absorption spectra, determine the conformations present in the sample, and measure the excited-state lifetimes of each of these conformations. Collaborative work calculating the excited-state trajectories and structural

analysis of the sample also allows for a thorough understanding and model of the complex motions available to excited molecules.

In the following works, the excited-state dynamics and relaxation mechanisms of a variety of organic compounds including pigments, nucleosides, alternative nucleobases, and tripeptides were elucidated. For the organic pigments, nucleosides, and tripeptides, the dominant process in the relaxation mechanism is excited-state intramolecular hydrogen, proton, and charge transfer (ESIHT, ESIPT, and ESICT). Removal and substitution of functional groups at or near the transfer site of the molecule modify the excited-state lifetimes illuminating upon key features that influence this ultrafast process and subsequently the potential energy surface of each molecule. Measurement of the excited-state dynamics of alternative nucleobases such as isocytosine similarly reveal the importance of light as a selective evolutionary pressure of the canonical nucleobases as the building blocks of DNA and RNA.

REMPI provides detailed chemical analysis of compounds capable of simultaneously distinguishing between isomers as well as compounds capable of absorbing the same wavelength of light. However, the technique provides no spatial or surface analysis of the sample. Tip Enhanced Laser Desorption (TELD), a novel sub-micron sampling technique, was developed as an off-line compliment to REMPI capable of producing detailed surface analysis, selection of material on the surface with approximately 200 nm lateral resolution, and femtomole levels of detection.

Finally, a brief study of the lasing properties of InGaN/GaN was characterized using an ultrafast pump laser source, revealing a new lasing wavelength at 568 nm, a region previously not producible with solid-state lasers.

## II. Excited-State Intramolecular Proton Transfer of Organic Pigments and Dyes

The combination of available trajectories a molecule can utilize to relax after excitation are often unique to each compound. However, it is possible to predict the likely relaxation mechanisms a molecule can use based on its structure. In the following studies, excited-state intramolecular hydrogen, proton, and charge transfer was found to be a prominent mechanism available to the indigotin and hydroxyanthraquinone family of dyes. Previously, the dynamics of indigotin were studied revealing two possible trajectories the molecule can take to reach the ground state, ESIPT and ESIHT. To further detail the relaxation mechanism process, the excited-state transfer sites were deuterated revealing a kinetic isotope effect for one of the lifetimes measured, suggesting tunneling. Molluscan purple, also known as Tyrian purple, produces its vibrant and historic color from the chromophore, 6,6'-dibromo indigotin, and can still be traced on ancient art to this day. The dynamics and influence of bromination of indigotin on the ESIPT and ESIHT process are reported. Finally, hydroxyanthraquinone dyes, like the indigotin family, have cultural relevance and are responsible for the reds and yellows found on many older pieces of art. However, the excited-state lifetimes and subsequently their photostability greatly differ between small changes in their structure. Study of these dyes revealed the structural moieties that influence the trajectories the molecules can take to quickly relax to the ground state.

# I. Excited-state Dynamics of Deuterated Indigo

Trevor Cohen[1], Nathan Svadlenak[1], Charles Smith[1], Krystal Vo[1], Si-Young Lee[1], Ana Parejo-Vidal[1], Joseph Kincaid[1], Andrzej Sobolewski[2], Michal F. Rode[2], and Mattanjah S. de Vries[1*]

[1] *Department of Chemistry and Biochemistry, University of California Santa Barbara, CA 93106*- transfer sites and monitored the photo-reaction pathways of mono- and di-deuterated indigo *9510, USA* [2] *Institute of Physics, Polish Academy of Sciences, Warsaw, Poland*

***Abstract***

Indigo, a rich blue dye, is an incredibly photostable molecule that has survived in ancient art for centuries. It is also unique in that it can undergo both an excited-state hydrogen and proton transfer on the picosecond timescale followed by a ground state back transfer. Previously, we performed gas phase excited-state lifetime studies on indigo to study these processes in a solvent-free environment, combined with excited-state calculations. We found two decay pathways, a fast sub-nanosecond decay and a slow decay on the order of 10ns. Calculations of the excited-state potential energy surface found that both hydrogen and proton transfer are nearly isoenergetic separated by a 0.1 eV barrier. To further elucidate these dynamics, we now report a study with deuterated indigo, using resonance enhanced multi-photon ionization and pump-probe spectroscopy with mass spectrometric isotopomer selection. From new calculations of the excited-state potential energy surface, we find sequential double proton or hydrogen transfer, whereby the trajectory to the second transfer, passes a second barrier and then encounters a conical intersection that leads back to the ground state. We find that deuteration only increases the excited-state lifetimes of the fast decay channel, suggesting tunneling through the first barrier, while the slower channel is not affected and may involve a different intermediate state.

### *1. Introduction*

Since antiquity, dyes obtained from animal parts, bugs, and plants have been used to produce vibrant colors for painting on a variety of art media. One such dye, indigo, has been used in many ancient civilizations such as the Roman and Maya empires and was highly sought after for its brilliant deep blue color.[1] Indigo can be observed throughout history due to its stability, especially against photodamage, rendering it still visible on many pieces of art.[2] This inherent stability also explains the popularity of this dye to this day. High photostability is directly correlated with a fast excited-state relaxation mechanism which can be modeled through excited-state dynamics studies.

Upon absorption of light, a molecule must be able to return to the ground state at a fast rate to prevent other damaging reactions from occurring. Such fast internal conversion often proceeds via conical intersections.[3] In the case of indigo, the excited molecule initially undergoes an excited-state intramolecular hydrogen or proton transfer (ESIHT or ESIPT) tautomerizing from the diketo to the keto-enol conformer. Yamazaki et al. followed by Moreno et al. were the first to calculate this relaxation mechanism through excited-state calculations mapping part of the energy surface.[4] Berenbeim et al. showed that blocking the path to excited-state intramolecular proton transfer through hydroxyl substitution in anthraquinone dyes greatly increased the excited-state lifetimes.[5] The excited-state lifetimes of various forms of indigo such as indigo carmine and leuco-indigo were measured in solution and was found to depend on solvent polarity.[6]

Previously, we studied the excited-state dynamics of indigo in the gas phase using resonance enhanced two-photon ionization (R2PI) in combination with excited-state

calculations.[7] Pump-probe spectroscopy performed in both the picosecond and nanosecond time regimes revealed two distinct decay channels. While the calculated potential energy surfaces reveal that indigo can undergo ESIPT or ESIHT, both processes are generally known to be sub-picosecond events and would therefore be too fast to directly measure with our laser systems. We therefore proposed that the two measured lifetimes reflect dynamics of the keto-enol tautomer that forms from these transfers, with the faster decay tentatively assigned to that of the tautomer formed from ESIPT and the slower from ESIHT. Excitation to a vibronic state below 800 $cm^{-1}$ resulted in lifetimes on the order of a nanosecond for the faster channel and 10-20 ns for the slower channel. Upon excitation at higher excess energy, we only observed a single fast decay that decreased in lifetime with increasing energy to 105 ps at 1456 $cm^{-1}$ and down to 60 ps at 1859 $cm^{-1}$.

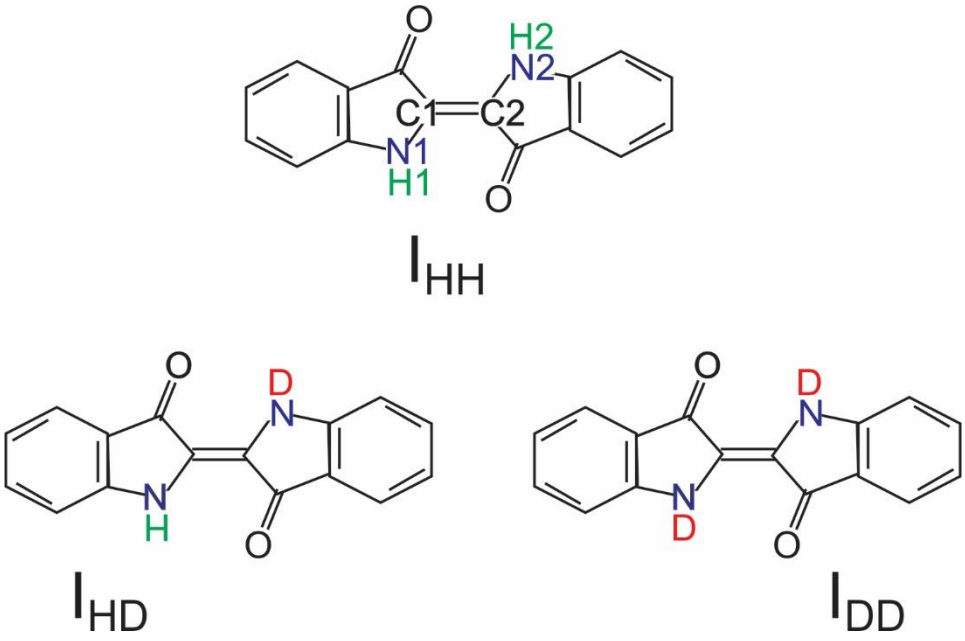


**Figure 1:** The chemical structures of $I_{HH}$, $I_{HD}$, and $I_{DD}$. All three forms of indigo are assumed to be only observable in the trans-diketo tautomer in the cold jet before excitation.

Deuteration has been used extensively in excited-state dynamics studies involving proton and hydrogen transfers to measure kinetic effects by increasing the mass of the transferring atom. Green et al. found deuteration of Criegee intermediates slowed the rate of formation of hydroxyl radicals indicating a proton transfer was involved.[8] Bodi et al. found that the deuteration of acetone ions slowed the PT tunneling process 100-fold completely shutting off the pathway to form methane.[9] In solution, studies of deuterated indigo carmine revealed a longer excited-state lifetime suggesting that the proton most likely tunneled through the barrier.[10] Excited-state calculations found that the barrier to proton transfer in indigo is dependent on the distance between the N and O atoms, revealing the amino hydrogens in the diketo form are the target site for the ESIPT and ESIHT.[11]

In this study, we deuterated the two sites on indigo capable of proton or hydrogen transfer to measure and analyze the effect on the excited-state dynamics (see Figure 1). Additionally, we present further calculations of the potential energy surface of indigo revealing that transfer of a second proton or hydrogen leads to a conical intersection region and back to the ground state. Using mass selective R2PI experiments, we independently measured the dynamics of indigo ($I_{HH}$), monodeuterated indigo ($I_{HD}$), and di-deuterated indigo ($I_{DD}$). We found that only the fast process showed a kinetic isotope effect, pointing to a different mechanism than previously proposed for the slow decay. $I_{HD}$ measurements revealed that the order of hydrogen or deuteron transfer has a major effect on the measured excited-state lifetimes suggesting the transfer mechanism is sequential, consistent with the shape of the excited-state potential energy surface.

## *2. Methods*

### *2.1. Computational*

The equilibrium geometry of the most stable form of the indigo molecule in its closed-shell ground electronic state ($S_0$), the planar diketo form (Fig. 1A), was determined with the MP2 method[12] with $C_s$ symmetry constraint. The minimum energy of the $S_0$ state is the reference value for all other ground state and excited state structures. The excited state ($S_1$) equilibrium geometries were determined with the second-order algebraic diagrammatic construction ADC(2) method[13]. The correlation-consistent valence double zeta basis set with polarization functions on all atoms (cc-pVDZ)[14] was used in these calculations as well as in the calculations of potential energy profiles and surfaces.

To study the reaction paths of the two active protons in the excited state of the diketo form, relaxed potential energy profiles were calculated; first, along the first NH coordinate, $R_1$ (N1-H), and subsequently along the second NH coordinate, $R_2$ (N2-H). For each fixed value of a given NH coordinate the remaining internal nuclear coordinates were optimized.

To reveal the mechanism of the double proton transfer process, relaxed potential energy surfaces were calculated in the ground state and in the excited state. The two NH stretching coordinates $R_1$ and $R_2$ were fixed, while the remaining nuclear coordinates were optimized for a given state. All calculations were performed using the TURBOMOLE program package[15].

### *2.2. Experimental*

The deuterated indigo was synthesized in a two-step, one pot process (Figure 2). Indigo was purchased from Sigma Aldrich (95% purity). Because indigo has very low solubility

with most solvents in its base structure, it was reduced to leuco-indigo and dissolved in a bath of NaOH, sodium dithionate, and then deuterated at the target sites. After 3 hours of heating at 80°C, oxygen bubbled through the solution and the deuterated indigo was precipitated out. This resulting product consisted of a mixture of $I_{HH}$, $I_{HD}$, and $I_{DD}$. Each indigo was identified and present in the product and confirmed through monitoring in a time-of-flight mass spectrometer.

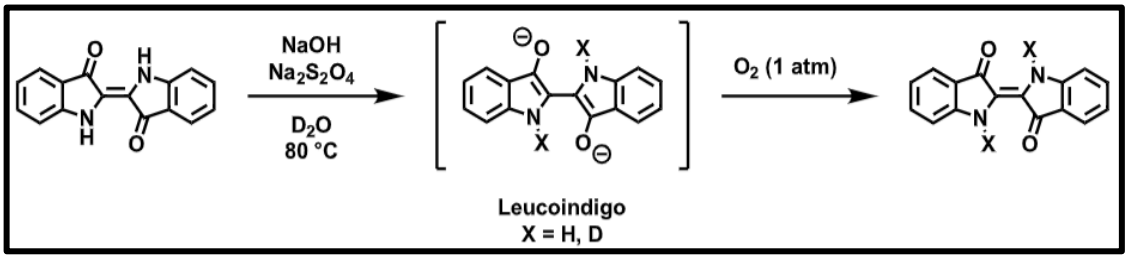


**Figure 2:** The reaction scheme for the synthesis of deuterated indigo. Indigo sample is reduced to its leuco-form, heated, and undergoes deuterium exchange with deuterated water. The solution is then oxidized resulting in a mixture of $I_{HH}$, $I_{HD}$, and $I_{DD}$.

We have described R2PI spectroscopy and pump-probe experiments in detail previously and will briefly summarize them here.[16] The deuterated indigo was placed on a graphite bar and loaded into the chamber (~$2x10^{-6}$ torr). A 1064 nm laser (Continuum Minilite I, 5 ns pulse width) is focused onto the graphite bar, desorbing and vaporizing the sample with minimal fragmentation. To continuously refresh the desorption area with new material, the sample stage is translated orthogonal to the desorption laser. To jet-cool the sample gas, a molecular beam of argon is pulsed into the chamber (8 atm backing pressure, 30 μs pulse width), entraining the sample in a supersonic jet. Through collisions with the argon, the sample is cooled to ~15K and directed into the sub-chamber of the mass spectrometer through a skimmer.

Both Resonant Two-Photon Ionization (R2PI) and pump-probe spectroscopy were used for characterization and analysis of the excited-state dynamics in the ns and ps time regime. For the R2PI experiments on the ps timescale, the third harmonic of an EKSPLA PL2251 Nd:YAG laser (30 ps pulse width, 1064 nm fundamental) pumped an EKSPLA PG-401 tunable optical parametric generator (OPG). This system produces 6.5 $cm^{-1}$ linewidth, 30 ps, ~600 μJ pulses in the visible wavelength region. The OPG is scanned from 500-560nm to resonantly excite the molecule to the S1 state. For ionization, the fundamental and second harmonic produced from the pump laser are combined to generate the $5^{th}$ harmonic (213nm). To measure excited-state lifetimes, the ionization laser is mechanically delayed with a Thorlabs 300mm mechanical delay stage with a retroreflector providing a delay of up to approximately 2,000 ps. For measurements with longer delay times, the scannable pulse generated from the ps OPG system was coupled with a 213 nm pulse generated from a Quantel DCR-11 Nd:YAG laser (5 ns, 8 mJ/pulse). The picosecond OPG pulse and ns DCR-11 pulse were delayed electronically with a Stanford Instruments DG-645 delay generator to measure ns pump probes. For both ns and ps pump probe experiments, the relative ion count is measured as a function of the delay of the ionization laser and convolved and fitted to either a monoexponential or biexponential decay in a Mathematica script.[17] The signal to noise in the data and the pulse width of the lasers limit the precision with which we can derive lifetimes from this fitting procedure. For the pump-probe spectra obtained with ps ionization pulses the precision is 100 ps; for the pump-probe spectra obtained with ns ionization pulses the precision is 3 ns.

## *3. Results*

### 3.1 Experimental results

Figure 3 shows the R2PI spectra for $I_{HH}$, $I_{HD}$, and $I_{DD}$, obtained with 213 nm, 30 ps ionization pulses. Excitation wavelength is given as excess energy beyond the origin, which for $I_{HH}$ is at 18,129 $cm^{-1}$. $I_{DD}$ blue shifts approximately 6-10 $cm^{-1}$ relative to $I_{HH}$. We observed vibronic lines up till about 1,800 $cm^{-1}$ excess energy, with decreasing excited state lifetimes beyond about 1,000 $cm^{-1}$ (vide infra). For $I_{HH}$ we previously found from IR-UV double resonant spectroscopy that the diketo tautomer of indigo was the only species observed in our experiment.[7] We assume the same holds true for $I_{HD}$ and $I_{DD}$. Thus, we assigned all the vibronic transitions in each of the isotopomers to this tautomer. The $I_{DD}$ excitation peaks shift approximately 6-10 $cm^{-1}$ to the blue of the corresponding $I_{HH}$ peaks, depending on the vibrational mode. The $I_{HD}$ peaks are broader than those for $I_{HH}$ and $I_{DD}$ and include the excitation wavelengths of both isotopomers. We interpret this observation as

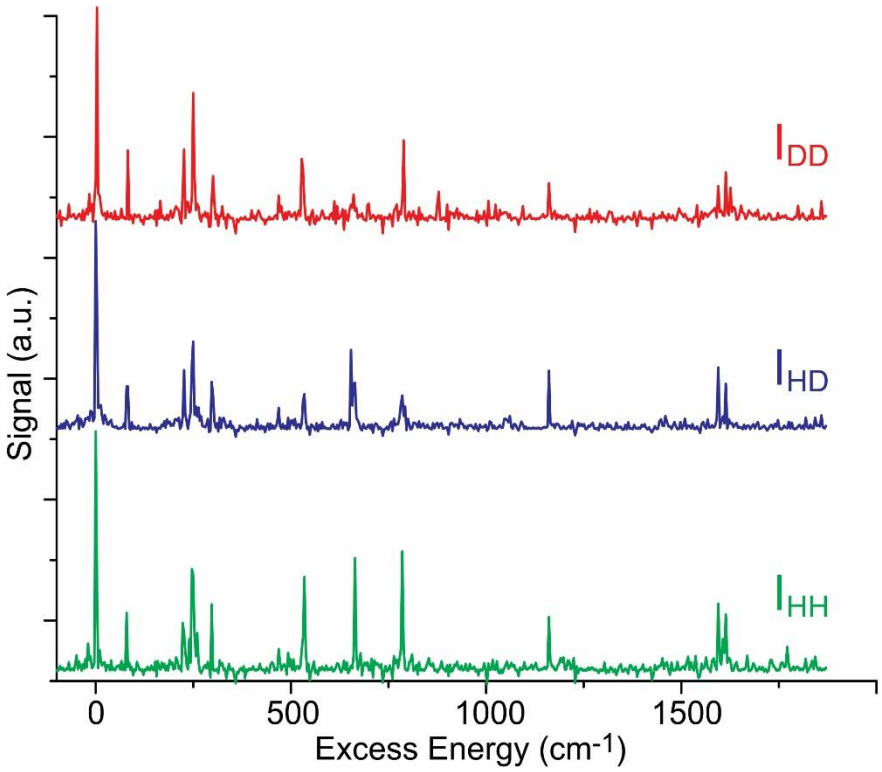


**Figure 3**: R2PI spectra for $I_{HH}$ (green), $I_{HD}$ (purple), and $I_{DD}$ (red), obtained with 30 ps excitation pulse and 213 nm, 30 ps ionization pulse

absorption by either the undeuterated or the deuterated chromophore. Therefore, the excitation wavelength selects whether the excited-state dynamics is initiated by the proton or the deuterium transfer, as further discussed below. The line width of the ps laser system (6.5 $cm^{-1}$) is too broad to fully resolve each peak corresponding to the hydrogen or deuterium chromophore excitation resulting in the broadened feature.

Figure 4 shows the R2PI spectra obtained with ns ionization (213 nm, 6 ns pulses). A nanosecond pulse width ionization laser cannot efficiently ionize excited states with lifetimes below 1 ns. In our previous work, with ns ionization we did not observe transitions beyond 725 $cm^{-1}$ excess energy, suggesting the existence of a barrier beyond which the excited state lifetime is too short for ns ionization. The current work revealed transitions up to 987 $cm^{-1}$ excess in energy. In $I_{HD}$ and $I_{DD}$ we measured transitions up to 1020 $cm^{-1}$ in excess energy.

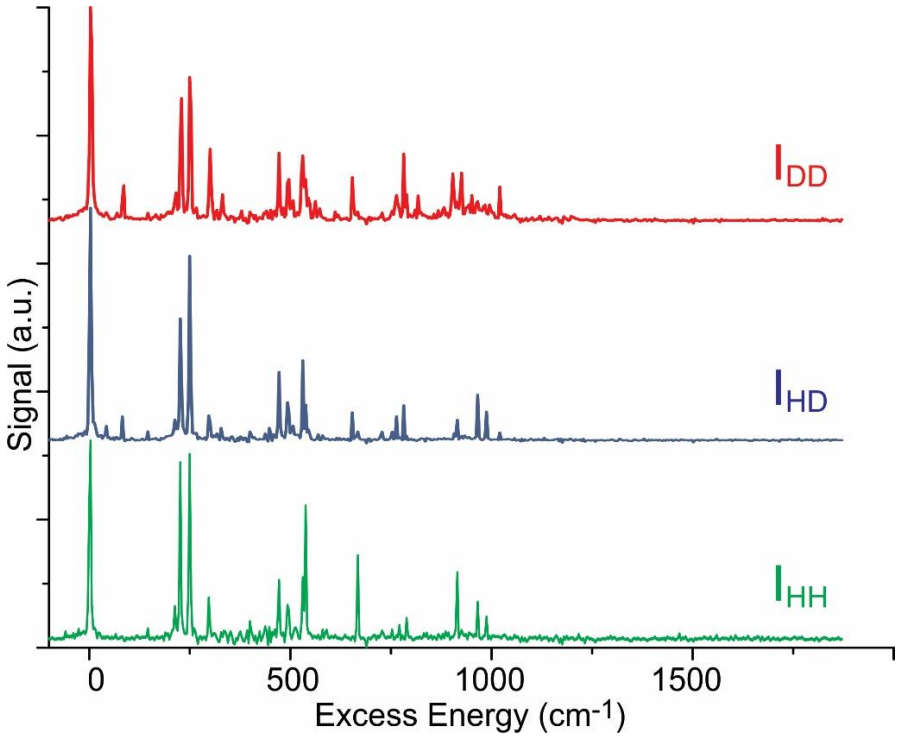

**Figure 4**: R2PI spectra for (green) $I_{HH}$, (purple) $I_{HD}$, and (red) $I_{DD}$, obtained with 30 ps excitation pulse and 213 nm, 6 ns ionization pulse without delay.

We measured the excited-state lifetimes of $I_{HH}$, $I_{HD}$, and $I_{DD}$ in the picosecond and nanosecond regimes at each vibronic transition in the R2PI spectrum using pump-probe spectroscopy. Figures 5 and 6 show sample picosecond and nanosecond pump-probe spectra and exponential fitting at the origin transition. Additional ps and ns pump probe spectra examining the PES of $I_{HD}$ and $I_{DD}$ can be found in Figures S1-4. Table 1 lists the excited-state lifetimes of $I_{HH}$ and $I_{DD}$ in the ps and ns regime as well as the corresponding ratios of those lifetimes, which represent the kinetic isotope effect (KIE). For the slow decay we do not observe a KIE, with the value equal to 1 within the margin of error. Like $I_{HH}$, $I_{DD}$ exhibits two lifetimes: A fast decay observed with ps ionization, which we denote as $\tau_{1H}$ and $\tau_{1D}$ and a slow decay observed with ns ionization, denoted as $\tau_{2H}$ and $\tau_{2D}$. The average kinetic isotope effect below the barrier was 4 for the faster decay while we observed no effect for the slower process. Beyond the 1000 $cm^{-1}$ excess energy transition, we did not observe the slow decay corresponding to $\tau_{2H}$ and $\tau_{2D}$, while for the fast decay both $\tau_{1H}$ and $\tau_{1D}$ decrease with increasing energy.

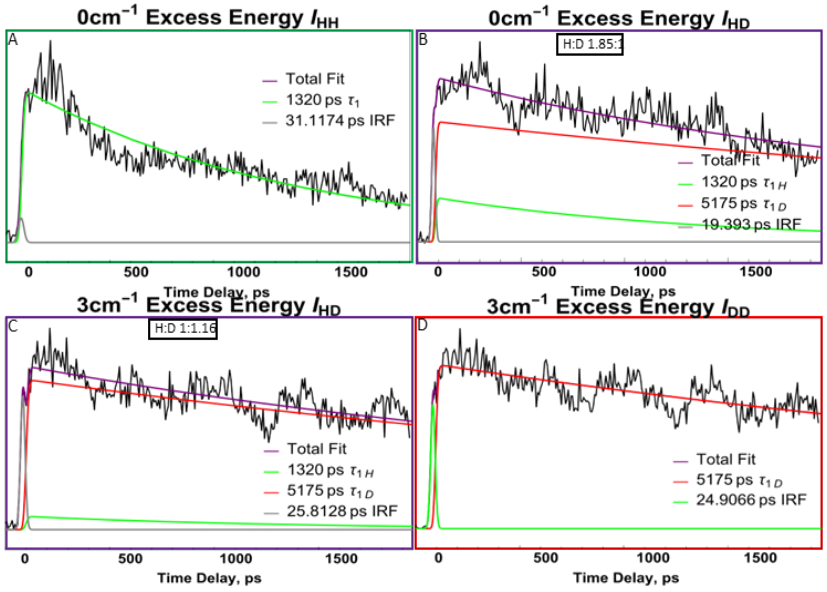

**Figure 5:** Picosecond pump-probe spectra for (A) $I_{HH}$, (B) and (C) $I_{HD}$, (D) $I_{DD}$. The experimental data in the case of $I_{HH}$ are those of reference 7. For each fit of the exponential decays, the faster hydrogen transfer decay is in green, the slower deuterium transfer in red, and the total fit in purple. The instrument response function (IRF) is gray.

In monodeuterated indigo, $I_{HD}$, it may make a difference whether the deuterated or the undeuterated chromophore is excited. Since the excitation of $I_{DD}$ is blue-shifted by 6 $cm^{-1}$, we assume that in the case of $I_{HD}$ the deuterated chromophore absorbs at 6 $cm^{-1}$ to the blue of the undeuterated chromophore. The two excitations were not fully resolvable since the linewidth of the laser was too broad, and therefore at each given wavelength a mixture of the deuterated and non-deuterated chromophores was excited resulting in a convolution of the two excited-state lifetimes which we analyzed as follows. For each vibronic $I_{HD}$ peak below the barrier, we measured two pump-probe spectra, one at the $I_{HH}$ wavelength and one at the $I_{DD}$ wavelength. We assumed that each decay trace corresponded to a combination of decays from each chromophore, whereby the contribution from the H-chromophore and D-chromophore is larger at the $I_{HH}$ and $I_{DD}$ wavelength respectively. Thus, using the lifetimes and the peak wavelength obtained for $I_{HH}$ and $I_{DD}$, we calculated the contribution of each chromophore excitation at a given transition. Table 2 lists these contributions for the ps and ns timescale, respectively.

The presence of C-13 isotopes complicates the interpretation of these spectra. The signal from the $I_{HH}$ mass spectrum is entirely due to $I_{HH}$, however, the $I_{HD}$ mass peak is formed by a combination of $I_{HD}$ molecules and $I_{HH}$ molecules with a C-13 isotope. For example, denoting molecules with a C-13 isotope with a prime, the signal at I+1 M/Z is the result of 13 abundance, 16.2% of all indigo molecules have at least one C-13 atom. The

occurrence of multiple C-13 isotopes on a single molecule is below our noise threshold. ($I_{HD}$ + $I'_{HH}$). The signal at the I+2 M/Z is the result of ($I_{DD}$ + $I'_{HD}$). With a 1.1% natural C-

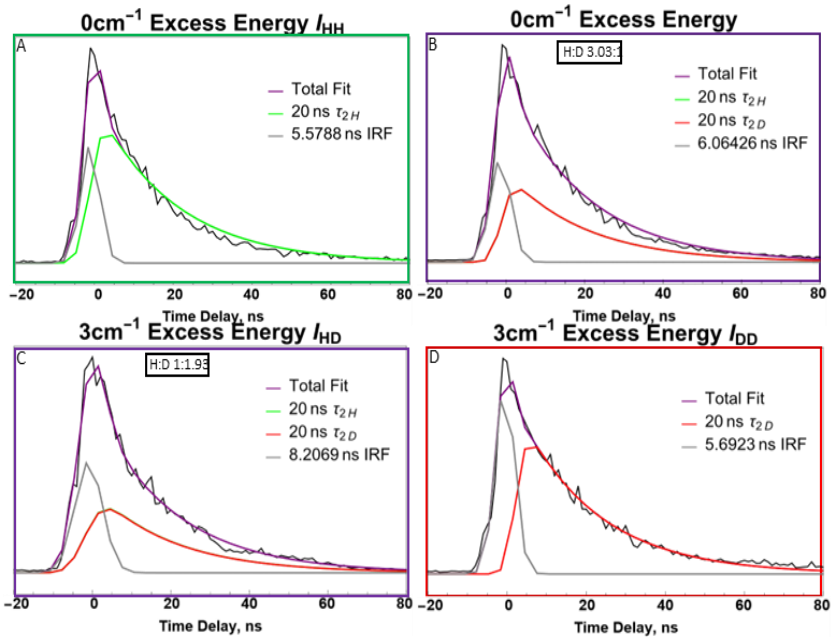


**Figure 6:** Nanosecond pump-probe spectra for (A) $I_{HH}$, (B) and (C) $I_{HD}$, (D) $I_{DD}$. For each fit of the exponential decays, the hydrogen transfer decay is in green, the deuterium transfer in red, and the total fit in purple. The instrument response function (IRF) is gray.

We derived the relative abundances of the deuterated chromophores by solving for all six species present in our mass signals: $I_{HH}$, $I'_{HH}$, $I_{HD}$, $I'_{HD}$, $I_{DD}$, $I'_{DD}$ ($I'_{DD}$ does not become convoluted with our other signals because it occurs at mass I+3), using the following equations:

$I = I_{HH}$

$I+1 = I_{DH} + I'_{HH}$

$I+2 = I_{DD} + I'_{HD}$

$(0.162)I_{HH} – (0.838)I'_{HH} = 0$

$(0.162)I_{HD} – (0.838)I'_{HD} = 0$

$(0.162)I_{DD} - (0.838)I'_{DD} = 0$

Solving for these variables allowed us to determine the relative abundances of the various deuterated species. This correction was only needed for the $I_{HD}$ signal, which was split between the I+1 and I+2 M/Z mass peaks.

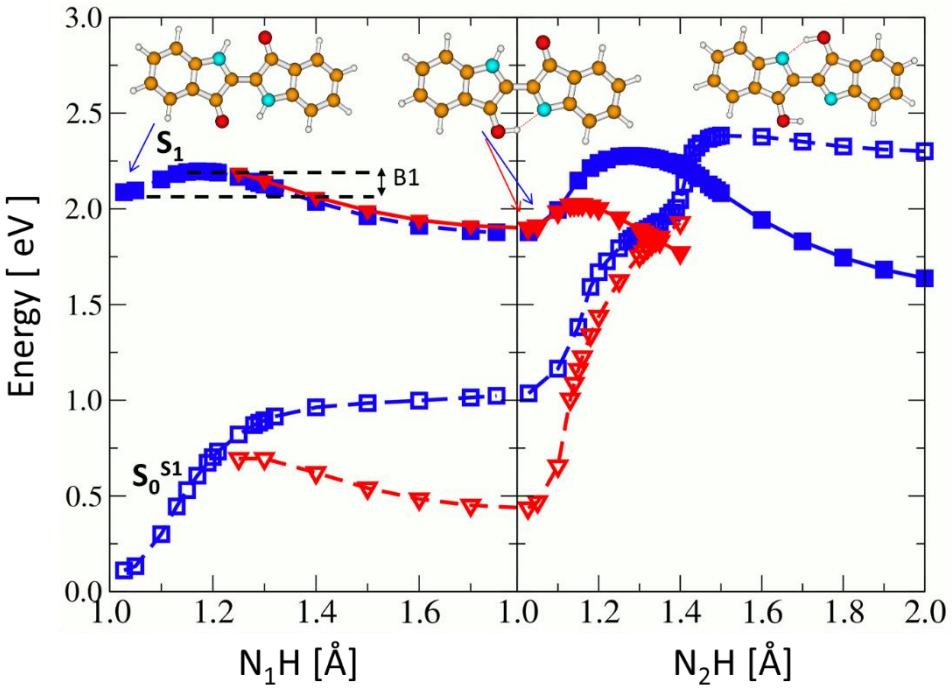


**Figure 7.** Two minimum energy profiles of indigo (calculated at the ADC(2)/cc-pVDZ level) plotted as a function of $N_1$-H distance (left panel, first ESIPT) and $N_2$-H distance (right panel, second ESIPT). Solid lines denote minimum-energy profiles of the $S_1$ state. Dashed lines ($S_0^{S1}$) denote energy profiles of the $S_0$ state computed at the optimized geometries of the $S_1$ state. See text for details.

### *3.2. Computational Results*

Figure 7 shows two minimum energy potential-energy (PE) profiles of the $S_0$ (dashed lines) and $S_1$ (solid lines) states of indigo calculated at the ADC(2)/cc-pVDZ level along

minimum-energy paths optimized in the S1 state. The NH coordinate was frozen in these calculations, while the rest of the parameters were optimized in the $S_1$ state. We obtained two PE profiles, which we denote as X (red) and Y (blue). The PE profiles of the X and Y conformers are represented by red triangles and blue squares, respectively. The left panel plots the PE profile along the $R_1$ coordinate, representing an initial excited state proton transfer for X and hydrogen transfer for Y. This profile has a barrier, B1, of approximately 0.1 eV. The right panel plots the PE profile along the second N-H coordinate, $R_2$, representing a subsequent second $H/H^+$ transfer. After the first transfer, indigo enters a local minimum forming the keto-enol tautomer, from which the second transfer can proceed towards the enol-enol tautomer.

The X and - profiles are nearly degenerate in the Frank-Condon region with a barrier between them of less than 0.01 eV [7]. However, these profiles deviate in energy along the second $H/H^+$ transfer coordinate. We identify X as the result of proton transfer and Y as the result of hydrogen transfer upon excitation. X and Y are further distinguished by a different C1-C2 distance for the keto-enol form, which is 1.454 Å for X and 1.382 Å for Y. This difference between X and Y is maintained along the entire range of both N1-H and N2-H stretching coordinates. The $S_1$-state proton transfer profile, X, is characterized also by geometries with a larger $S_1$-state dipole moment, $\mu_e$, than for the $S_1$-state hydrogen transfer, Y. In the enol-keto form $\mu_e$ equals 6.8D for X and 3.4D for Y. Along the path of second the $H/H^+$ transfer we found a barrier (B2) of 0.124 eV for X at N2H=1.14 Å and significantly higher barrier of 0.401 eV for Y at N2H=1.28 Å. Beyond that barrier we found a conical intersection along both X and Y reaction paths that leads back to the ground state followed by ground state intramolecular proton or hydrogen transfer back to the diketo form.

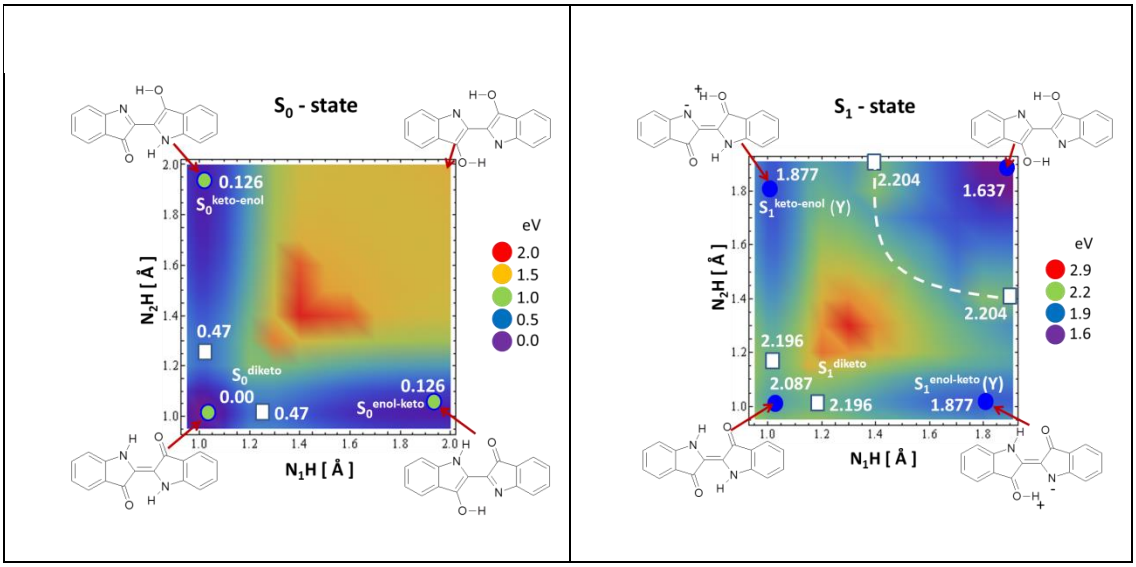


**Figure 8.** Relaxed potential-energy surfaces of (A) the electronic ground state and (B) the lowest excited state of the indigo molecule, both in the Y form, plotted as a function of the two stretching coordinates $R_1$ and $R_2$. Green circles represent ground-state diketo (global) and single-proton transferred enol-keto (local) minima. Blue circles represent $\mathbf{S_1^{diketo}}$, $\mathbf{S_1^{enol\text{-}keto}}$ and $\mathbf{S_1^{dienol}}$ minima. The dashed white line shows the $S_1/S_0$ conical intersection seam. The results were obtained with the ADC(2)/cc-pVDZ method for the excited state and with the MP2/cc-pVDZ method for the ground state. Relative energies of minima and barriers are given in eV.

Figure 8 shows relaxed potential-energy surfaces of (A) the electronic ground state and (B) the lowest excited state of the Y form, plotted as a function of the two stretching coordinates $R_1$(N1-H) and $R_2$(N2-H). As the molecule is symmetric with respect to exchange of these two coordinates the plots keep the same symmetry as well. As can be seen in panel A, the diketo form is the lowest energy tautomer in the $S_0$ ground state, and it is the dominant population in our experiment. In both $S_0$ and $S_1$ there is a very large barrier for a concerted double proton or hydrogen transfer to form the dienol tautomer which would be represented by a diagonal movement up and to the right in Figure 8. The barrier calculated

along this path is significantly higher in energy than the barrier for the sequential double transfer and this process therefore is not probable. Thus, the shape of the PE surfaces indicates the possible mechanism of sequential two proton/hydrogen transfer processes, both in the $S_0$ and $S_1$ electronic states as exothermic pathways. Figure S3 in supplemental information shows the IR-vibrational modes, that involve N-O or O-H motion, calculated with the TD-DFT/B3-LYP/cc-pVDZ method, for the $S_1$, diketo form.

**4. Discussion**

We previously calculated intramolecular proton or hydrogen transfer pathways along a single NH coordinate, essentially covering only the left-hand panel in Figure 7. That work did not elucidate a clear mechanism down to the ground state. We hypothesized that keto-enol indigo could undergo a non-radiative process back to the ground state potential and that decay in the Y form would be faster based on a smaller energy gap between the excited and ground states compared to X. In this work we extended the computations to include a second proton transfer, represented in the right-hand panel of Figure 7. We conclude that the X and Y trajectories differ along that second coordinate and that there is a conical intersection with the ground state along that part of the trajectory behind a barrier, B2. For the Y form the conical intersection is at higher energy and B2 is higher than for the X form. Experimentally, we measured excited-state lifetimes for deuterated indigo and observed a KIE for the faster decay and not for the slower decay. A complete modeling of these new observations will require future dynamics calculations, but absent those we can speculate about some possible explanations.

Based on our original double resonant spectroscopy, only the diketo tautomer is observed in our experiment, implying that both measured decays must derive from

excitation of this same species. If the two lifetimes would originate from decay of the same initial excited state, the significantly slower 20 ns decay would have an order of magnitude smaller quantum yield and would not be observed in this experiment, since most signal would derive from the faster mechanism. We therefore propose that, following excitation to the keto-keto excited state, a bifurcation takes place in which one trajectory follows the X part of the S1 surface with proton transfer, exhibiting a larger dipole moment, $\mu_e$, and stretching of the C1-C2 bond, and the other trajectory follows the Y part with hydrogen transfer, a smaller $\mu_e$ and a shorter C1-C2 distance. Each trajectory leads to a different form of keto—enol indigo, each with different excited-state lifetimes.

It is possible for the X trajectory to proceed through the conical intersection as indicated by the red curves in Figure 7. Our earlier work indicated that the ground state X PE surface involves a hydrogen (rather than proton) transfer, which implies that the transition from $S_1$ to $S_0$ along this path involves an electron transfer. If we assume that the first proton transfer is sub-picosecond then with our lifetime measurements we are merely observing the dynamics of the resulting KE tautomer that is formed, with X decaying faster than Y. However, if we assume that the observed KIE is due to passing (or tunneling through) the first barrier then the shorter lifetimes reflect the dynamics of the first part of the X trajectory, which is dominated by the first proton transfer but not at sub picosecond rates.

Assigning the slower decay to the Y form, we note that the initial part of the trajectory is almost identical to that of the X form, but with hydrogen rather than proton transfer. We would still expect a similar KIE effect for that first part of the trajectory but if the decay of the subsequent keto-enol form does not exhibit a KIE we would not observe the initial small

change of lifetime in our ns timescale measurements. There are a number of possible models for the slower decay of the keto-enol Y form.

(1) We rule out tunneling through the large, 0.4 eV second barrier, B2, to reach the conical intersection on the Y profile because we observe no KIE on the long lifetime decay. (2) When the system is trapped in the excited state keto-enol minimum it may interconvert by non-adiabatically populating the X form, from which it can decay to the ground state. (3) Another pathway from the long-lived Y keto-enol excited state could be fluorescence. From the energy and oscillator strength computed at the optimized geometries of the S1 state (CC2/cc-pVDZ optimization of the S1 state) we estimate a radiative lifetime of 11.2ns. This qualitatively reflects our observation. We note that for the keto-keto form the calculated radiative lifetime is 5.5 ns so while we cannot rule out fluorescence for this form it is an unlikely explanation given the observed KIE. (4) These scenarios do not explain the fact that the slow channel cannot be observed in the ns regime above about 0.1 eV excess energy. Therefore, we should also consider the possibility of exploring other parts of the PE landscape along other internuclear coordinates that might lead to population of other long-lived states, such as an nπ* state or a triplet state.

$I_{HD}$ provides a unique system since it breaks the symmetry of the molecule. Deuteration of only one of the chromophores acts as a spectroscopic tag that reveals which of the two chromophores is excited at a given transition. Even though the bandwidth of our ps laser system is limited, excitation at the $I_{HH}$ peak wavelength will preferentially excite the hydrogen containing chromophore ($\Phi_H$), while excitation at the $I_{DD}$ peak wavelength will preferentially excite the deuterated chromophore ($\Phi_D$). When $\Phi_H$ is excited H (or $H^+$) will transfer first; when $\Phi_D$ is excited D (or $D^+$) will transfer first. Analysis of the $I_{HD}$ decays in

the picosecond regime shows that when exciting $\Phi_D$, the decay is slower than when exciting $\Phi_H$, consistent with the model in which the decay rates are dominated by the first transfer, rather than the second. This result is consistent with the calculations that predict a concerted double proton or hydrogen transfer is not occurring, as in that case the rate would not change between each chromophore excitation unlike other similar double proton transfer mechanisms.[18]

### *5. Conclusions*

We have reported the R2PI spectra for $I_{HD}$ and $I_{DD}$ as well as their excited state lifetimes at each measured vibronic transition. There are two decay channels, a faster and a slower one. Deuterating both chromophores results in a KIE of ~4 for the faster channel but has no effect on the slower channel. Directly comparing the excited state lifetimes of each chromophore independently in $I_{HD}$ reveals that exciting the deuterated chromophore increases the excited state lifetime. Calculations of the excited state potential energy surfaces show trajectories with sequential double proton or hydrogen transfer. Along the path to the second transfer a conical intersection occurs to the ground state with a barrier approximately 0.1 eV high. Two potential-energy profiles are involved, X and Y with different C1-C2 distances and characterized by excited state proton transfer for X and hydrogen transfer for Y. The barrier to the conical intersection for Y is significantly higher than for X, most likely indicating that for the fast decay excited indigo relaxes to the ground state along the X potential. The longer lifetime channel likely reflects the decay from the keto-enol form along the Y potential energy profile. Further insights will be expected from excited-state dynamics computations to model of these results.

***Acknowledgment***

Calculations were performed at the PL-Grid Infrastructure. This work was supported by the National Science Foundation under CHE- 2154787. The authors thank prof. Wolfgang Domcke for helpful discussions.

**Author contributions**

TC: Performed experiments and analysis, wrote manuscript, NS contributed to experiments, analysis and manuscript, CS, KV, SYL, and APV performed experiments, JK conceived of and performed synthesis, AS and MR developed theoretical model, MR performed computations, MdV provided experimental setup, performed analysis, and edited final version of manuscript.

***References***

1. R. J. H. Clark, C. J. Cooksey, M. A. M. Daniels, and R. Withnall, Endeavour **17** (4), 191 (1993);
2. J. C. Splitstoser, T. D. Dillehay, J. Wouters, and A. Claro, Sci Adv **2** (9), e1501623 (2016).
3. R. M. Christie, Biotech Histochem **82** (2), 51 (2007).
4. J. A. Otterstedt, J Chem Phys **58** (12), 5716 (1973).
5. S. Yamazaki, A. L. Sobolewski, and W. Domcke, Physical Chemistry Chemical Physics **13** (4), 1618 (2011);
6. M. Moreno, J. M. Ortiz-Sanchez, R. Gelabert, and J. M. Lluch, Phys Chem Chem Phys **15** (46), 20236 (2013).
7. J. Berenbeim, S. Boldissar, S. Owens, M. R. Haggmark, C. Gatto, F. M. Siouri, T. Cohen, M. F. Rode, C. Schmidt Patterson, and M. S. de Vries, Sciennce Advances **5**, eaaw5227 (2019).
8. J. Pina, D. Sarmento, M. Accoto, P. L. Gentili, L. Vaccaro, A. Galvao, and J. S. S. de Melo, J Phys Chem B **121** (10), 2308 (2017);
9. N. D. Bernardino, S. Brown-Xu, T. L. Gustafson, and D. L. A. de Faria, Journal of Physical Chemistry C **120** (38), 21905 (2016);
10. I. Iwakura, A. Yabushita, and T. Kobayashi, Chem Lett **38** (11), 1020 (2009);
11. J. S. de Melo, A. P. Moura, and M. J. Melo, J Phys Chem A **108** (34), 6975 (2004);
12. P. P. Roy, J. Shee, E. A. Arsenault, Y. Yoneda, K. Feuling, M. Head-Gordon, and G. R. Fleming, J Phys Chem Lett **11** (10), 4156 (2020);
13. Y. Nagasawa, R. Taguri, H. Matsuda, M. Murakami, M. Ohama, T. Okada, and H. Miyasaka, Physical Chemistry Chemical Physics **6** (23), 5370 (2004).

14. M. R. Haggmark, G. Gate, S. Boldissar, J. Berenbeim, A. L. Sobolewski, and M. S. de Vries, Chemical Physics **515**, 535 (2018).
15. A. M. Green, V. P. Barber, Y. Fang, S. J. Klippenstein, and M. I. Lester, P Natl Acad Sci USA **114** (47), 12372 (2017).
16. A. Bodi, T. Baer, N. K. Wells, D. Fakhoury, D. Klecyngier, and J. P. Kercher, Physical Chemistry Chemical Physics **17** (43), 28505 (2015).
17. A. S. Chatterley, D. A. Horke, and J. R. R. Verlet, Physical Chemistry Chemical Physics **14** (46), 16155 (2012);
18. I. Iwakura, A. Yabushita, and T. Kobayashi, Chem Phys Lett **484** (4-6), 354 (2010).
19. A. Douhal, F. Lahmani, and A. H. Zewail, Chem Phys **207** (2-3), 477 (1996); J.A. Syage, J Phys Chem-Us **99** (16), 5772 (1995).
20. C. Moller and M. S. Plesset, Physical Review **46**, 618 (1934).
21. C. Hattig, Advances in Quantum Chemistry, Vol 50 **50**, 37 (2005);
22. J. Schirmer, Physical Review A **26** (5), 2395 (1982);
23. A. B. Trofimov and J. Schirmer, Journal of Physics B-Atomic Molecular and Optical Physics **28** (12), 2299 (1995).
24. T. H. Dunning, Journal of Chemical Physics **90** (2), 1007 (1989).
25. TURBOMOLE (2016).
26. G. Meijer, M. S. Devries, H. E. Hunziker, and H. R. Wendt, Applied Physics B-Photophysics and Laser Chemistry **51** (6), 395 (1990).
27. F. M. Siouri, S. Boldissar, J. A. Berenbeim, and M. S. de Vries, J Phys Chem A **121** (28), 5257 (2017).
28. K. Sakota and H. Sekiya, J Phys Chem A **109** (12), 2722 (2005).

T**able 1:** Excited-state lifetimes for $I_{HH}$ and $I_{DD}$ at various relative energies above the origin transition as well as the calculated kinetic isotope effect (KIE). The excess energies with corresponding $I_{DD}$ vibronic transitions are in parentheticals. The lifetimes of the fast decay for $I_{HH}$ and $I_{DD}$ are denoted $\tau_{1H}$ and $\tau_{1D}$ and $\tau_{2H}$ and $\tau_{2D}$ for the slow decay.

| Excess energy above $I_{HH}$ origin ($cm^{-1}$) | $\tau_{1H}$ (ps) | $\tau_{1D}$ (ps) | KIE $\tau_1$ | $\tau_{2H}$ (ns) | $\tau_{2D}$ (ns) | KIE $\tau_2$ | Excess energy above $I_{DD}$ origin ($cm^{-1}$) |
|---|---|---|---|---|---|---|---|
| 0 | 1320 | 5172 | 3.9 | 20.0 | 20.0 | 1.0 | 3 |
| 79 | 887 | 4999 | 5.6 | 22.4 | 20.6 | 0.9 | 83 |

| | | | | | | | |
|---|---|---|---|---|---|---|---|
| 297 | 1353 | 2209 | 1.6 | 9.2 | 15 | 1.6 | 300 |
| 531 | 2017 | 5779 | 2.9 | 13.3 | 16 | 1.2 | 527 |
| 654 | | 2092 | | | 14 | | |
| 664 | 1540 | | | 8.6 | | | |
| 785 | 692 | 1955 | 2.8 | 8.6 | 8.4 | 0.95 | 789 |
| 1161 | 168 | 638 | 3.8 | | | | |
| 1595 | | 321 | | | | | |
| 1614 | 79 | 314 | 4.0 | | | | |

**Table 2:** Observed picosecond lifetimes for $I_{HD}$. Since the respective H and D chromophores were not fully resolvable, the lifetimes in the fitted decays were fitted to the $I_{HH}$ and $I_{DD}$ lifetimes and the ratio of the normalized pre-exponential factors are reported. For peaks that were fully resolvable and showed monoexponential decay, the excited-state lifetimes were reported in the τ1 column.

| Excess Energy($cm^{-1}$)(Chromophore excited labeled with H or D) | Wavelength(nm) | $\tau_1$ (ps) | $\tau_{1H}$:$\tau_{1D}$ | $\tau_2$ (ns) | $\tau_{2H}$ :$\tau_{2D}$ |
|---|---|---|---|---|---|
| 0(H) | 551.6 | | 1.0:2.7 | | 3.0:1 |
| 3(D) | 551.5 | | 1.0:11 | | 1:1.9 |
| 79(H) | 549.2 | | 2.0:1 | | 1:60 |
| 83(D) | 549.1 | | 1.2:1 | | 28:1 |
| 297(H) | 542.7 | | 1.0:7.7 | | 8200:1 |
| 300(D) | 542.6 | | 2.8:1 | | 2.0:1 |
| 527(H) | 536 | | 1:4.5 | 13 | |
| 664(D) | 532.4 | 973 | | | |
| 667(H) | 532.3 | 717 | | 10 | |
| 785(D) | 528.7 | | 2.8:1 | | 100:1 |

| | | | | | |
|---|---|---|---|---|---|
| 789(H) | 528.6 | | 4600:1 | | 500:1 |
| 1161(H) | 518.4 | 170 | | | |
| 1595(H) | 507 | 77 | | | |
| 1614(H) | 506.5 | 89 | | | |

Supplemental Information

Figure S1: The pump probe transients of $I_{HD}$ on the ps timescale. The decays were fit exponentially fixing each lifetime to the corresponding $I_{HH}$ and $I_{DD}$ lifetimes.

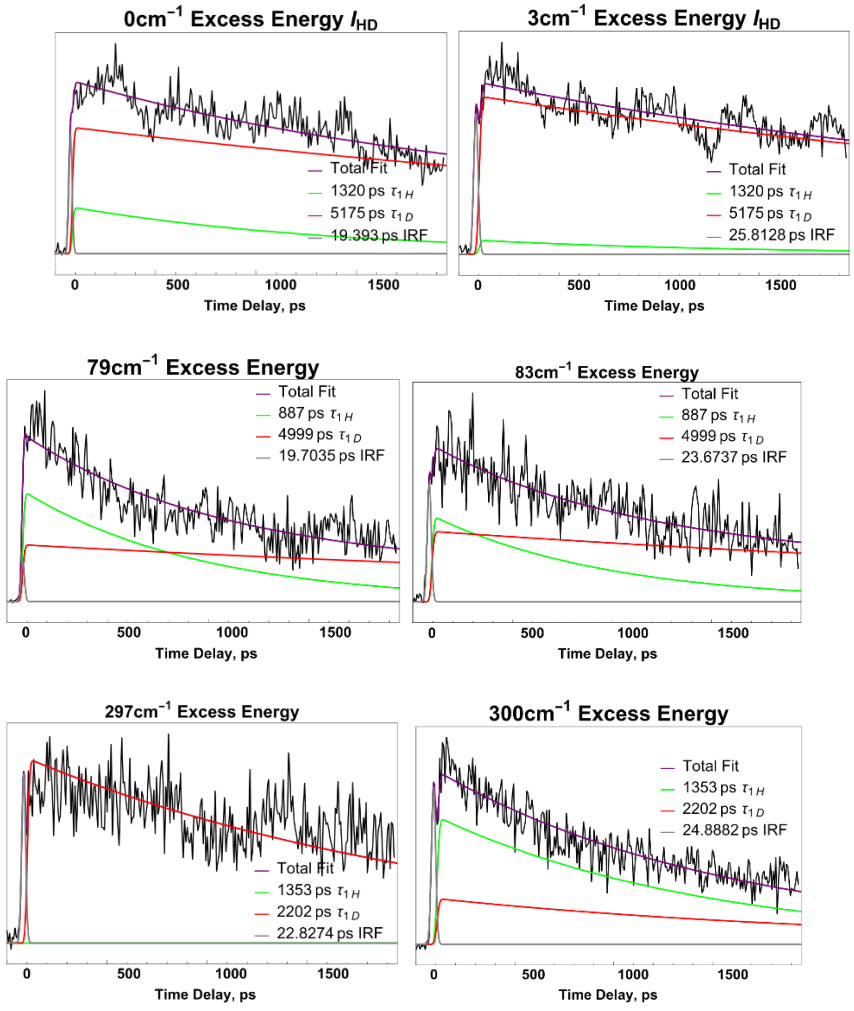

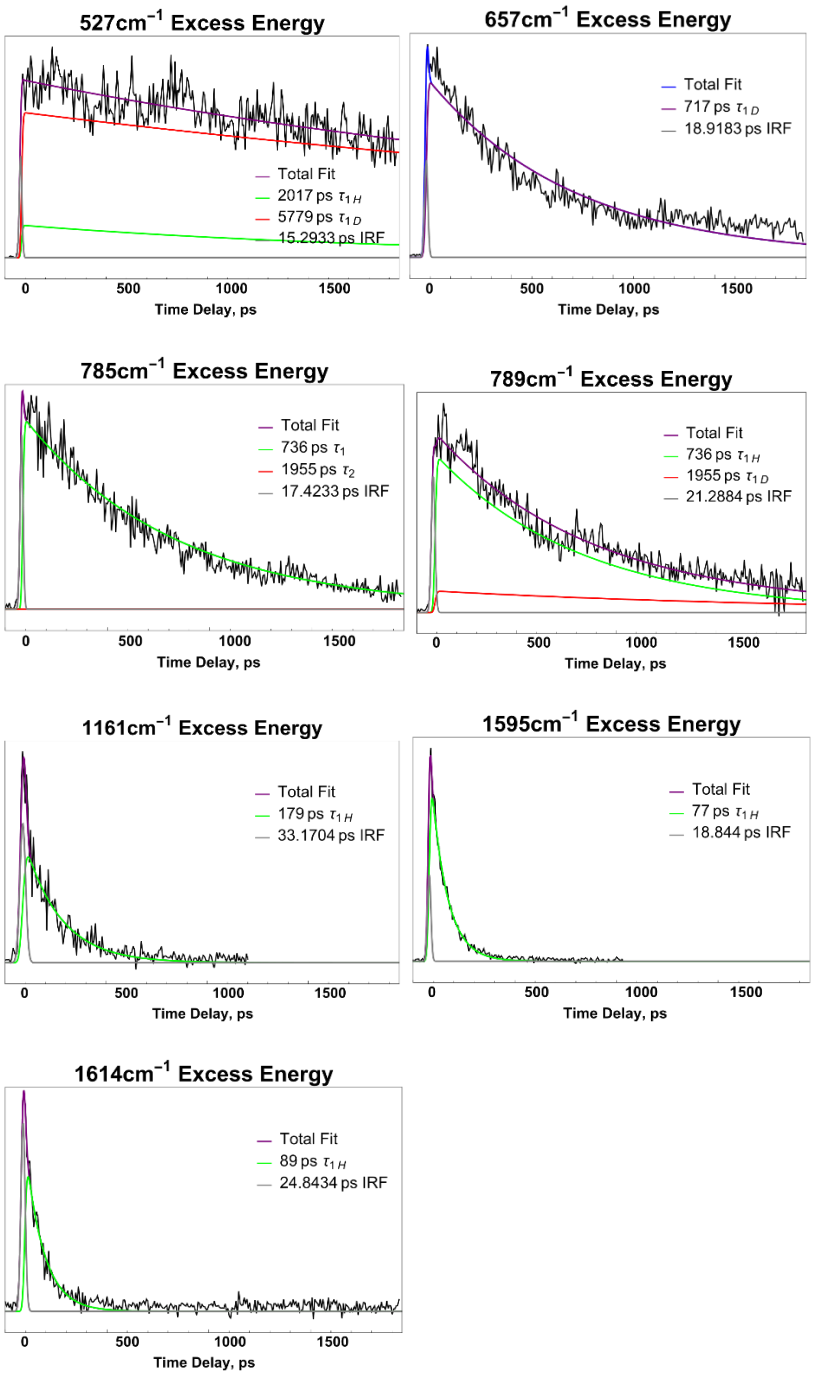


Figure S2: The pump probe transients of $I_{DD}$ on the picosecond timescale.

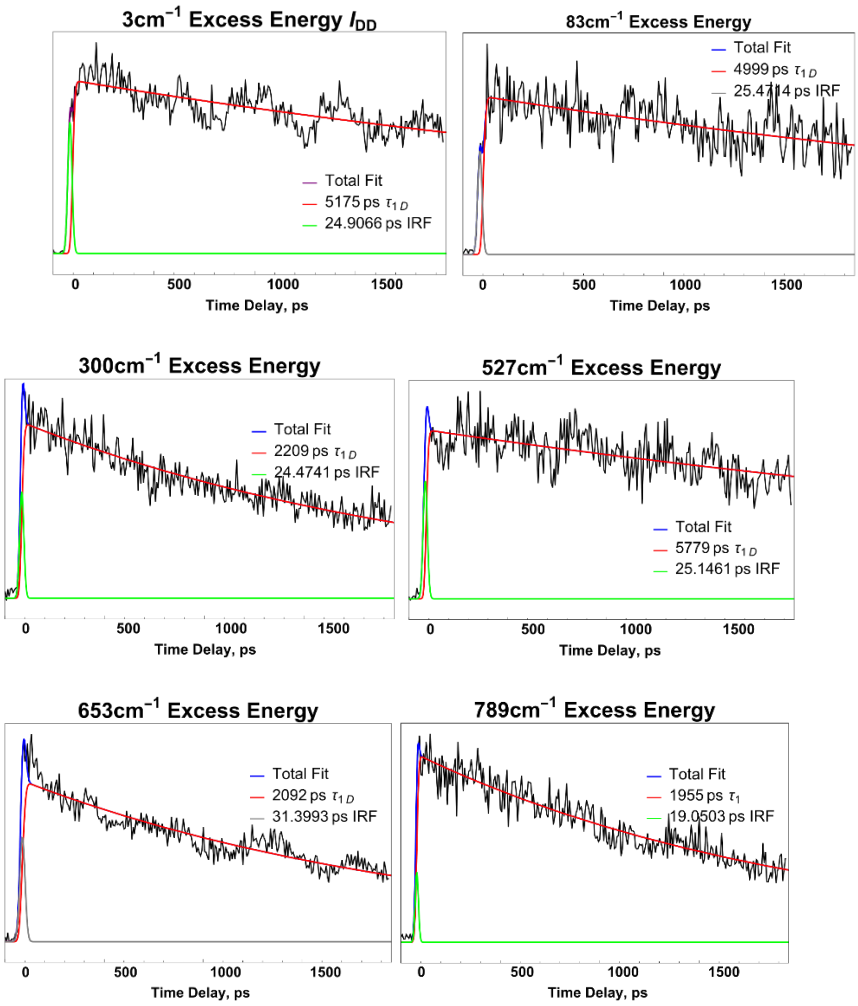


Figure S3: The pump probe transients of $I_{HD}$ on the nanosecond timescale.

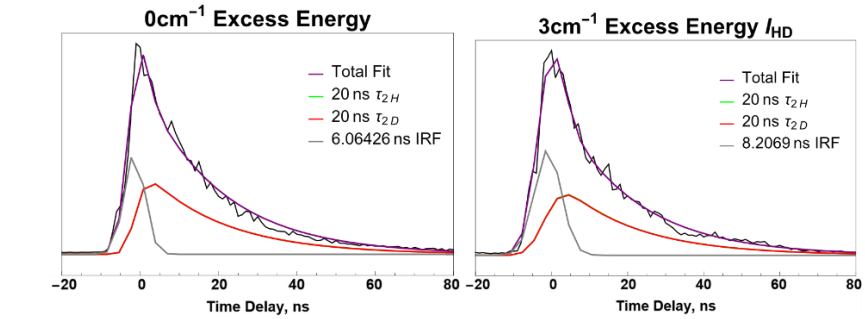
0cm$^{-1}$ Excess Energy
Total Fit
20 ns $\tau_{2H}$
20 ns $\tau_{2D}$
6.06426 ns IRF
3cm$^{-1}$ Excess Energy $I_{HD}$
Total Fit
20 ns $\tau_{2H}$
20 ns $\tau_{2D}$
8.2069 ns IRF
−20 0 20 40 60 80
Time Delay, ns

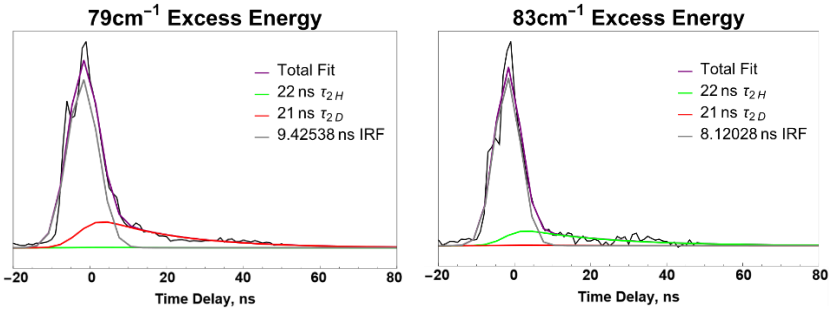
79cm$^{-1}$ Excess Energy
Total Fit
22 ns $\tau_{2H}$
21 ns $\tau_{2D}$
9.42538 ns IRF
83cm$^{-1}$ Excess Energy
Total Fit
22 ns $\tau_{2H}$
21 ns $\tau_{2D}$
8.12028 ns IRF
−20 0 20 40 60 80
Time Delay, ns

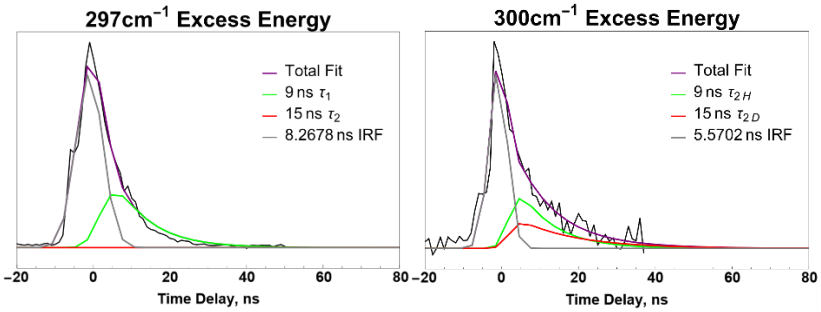
297cm$^{-1}$ Excess Energy
Total Fit
9 ns $\tau_1$
15 ns $\tau_2$
8.2678 ns IRF
300cm$^{-1}$ Excess Energy
Total Fit
9 ns $\tau_{2H}$
15 ns $\tau_{2D}$
5.5702 ns IRF
−20 0 20 40 60 80
Time Delay, ns

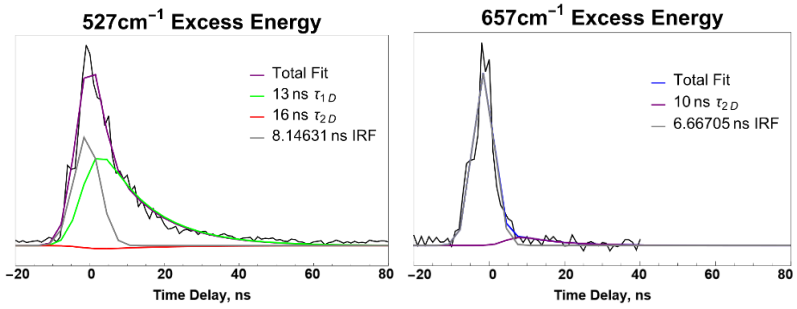
527cm$^{-1}$ Excess Energy
Total Fit
13 ns $\tau_{1D}$
16 ns $\tau_{2D}$
8.14631 ns IRF
657cm$^{-1}$ Excess Energy
Total Fit
10 ns $\tau_{2D}$
6.66705 ns IRF
−20 0 20 40 60 80
Time Delay, ns

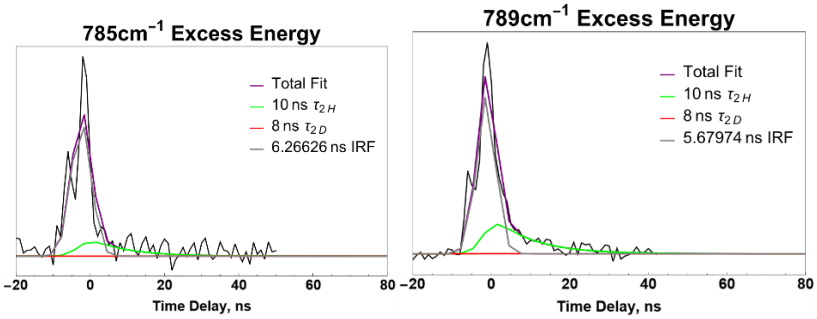
785cm$^{-1}$ Excess Energy
Total Fit
10 ns $\tau_{2H}$
8 ns $\tau_{2D}$
6.26626 ns IRF
789cm$^{-1}$ Excess Energy
Total Fit
10 ns $\tau_{2H}$
8 ns $\tau_{2D}$
5.67974 ns IRF
−20 0 20 40 60 80
Time Delay, ns

**Figure S4**: The pump probe transients of $I_{DD}$ on the nanosecond timescale.

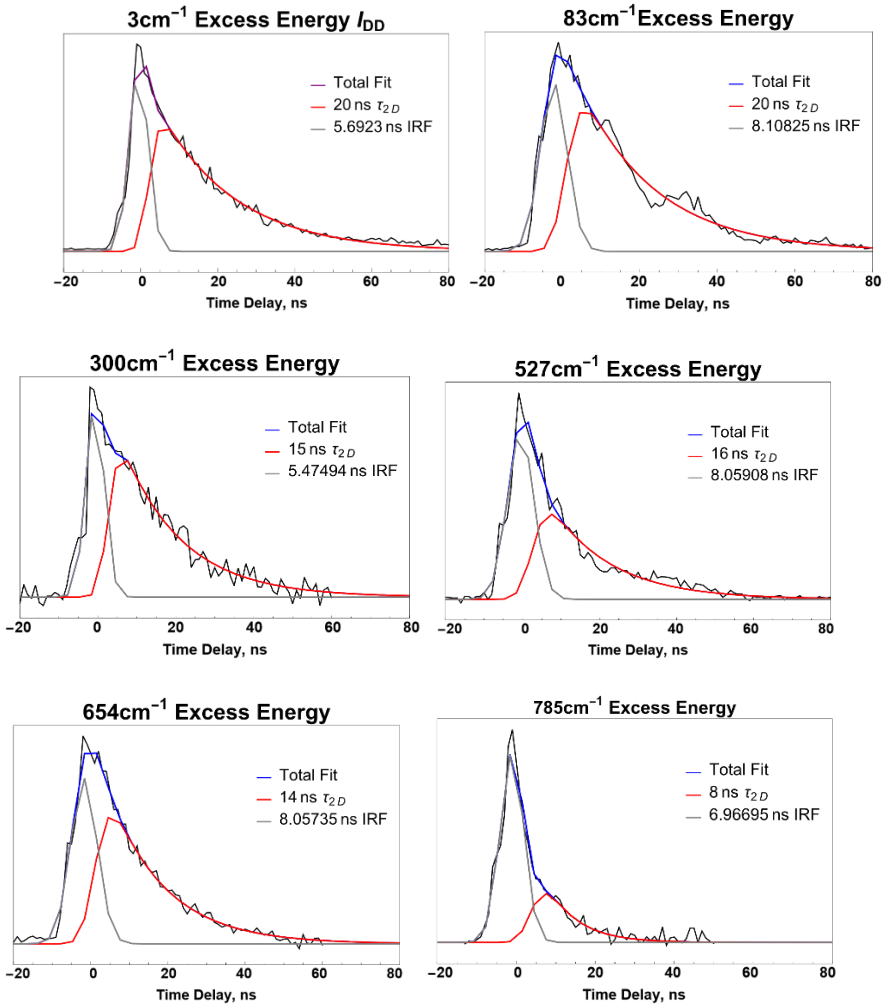


***II. The Excited State Dynamics of 6,6'-Dibromoindigotin: Exploring how Molluscan Purple has Survived throughout the Ages***

*Trevor Cohen, Julia Didziulis, Charles Smith, Michal Rhode[2], Mattanjah de Vries[1]*

*[1] Department of Chemistry and Biochemistry, University of California Santa Barbara,*

*CA 93106*- transfer sites and monitored the photo-reaction pathways of mono- and di-deuterated indigo *9510, USA [2] Institute of Physics, Polish Academy of Sciences, Warsaw, Poland*

**Abstract**

The color purple has long been used as a symbol of royalty and power in art, fashion, and architecture. This correlation with aristocracy can be traced back to the use of molluscan purple, a rich purple dye that is still presently more expensive than gold, by royalty as early as 1200 B.C. While the molluscan purple dye is composed of a mixture of various proteins, its color is derived from the molecule, 6,6'-dibromoindigotin, an analogue of the indigotin dye which is also widely used in various modern industries. Both dyes can exhibit high stability, in particular against photodamage from UV and Visible radiation. In this study, we present the gas phase absorption spectrum and excited-state lifetimes of 6,6'-dibromoindigotin combined with static calculations of the excited and ground-state potential energy surfaces. The lifetime measurements reveal that molluscan purple has nearly the same relaxation rate as indigotin providing new insights in the possible relaxation mechanisms of the indigotin family of dye molecules.

## 1. Introduction

The use of molluscan purple in wall paintings and textiles dating back up to the 18$^{th}$ century BC, has been directly proven through archaeometric investigations which reported the chemical identification of the purple pigment in archaeological fragments and, moreover, it is supported by the several heaps of molluscan shells found in archaeological sites of the Mediterranean (e.g. in Coppa Nevigata, Aegean islands, Phoenicia, etc).[1-3] Molluscan (or shellfish) purple is known also as Tyrian purple, because of its significant role in the history of the maritime Phoenician trade, as well as royal/imperial purple, as the expensive purple-dyed textiles were status symbols. It should be stressed, however, that the message derived from the terms *royal* or *imperial* purple might be misleading, because in certain historical periods and geographical areas molluscan purple was not reserved exclusively for members

of the royal family. For example, the studied purple fragments of (i) wall paintings in Raos-Thera site (Late Bronze Age), (ii) a textile in Lakkoma (Hellenistic period) and (iii) a textile in Thessaloniki (Roman period) are not linked to members of royal families, but rather to prominent citizens and high-ranking officials.[1,2,4,5]

The cultural relevance and trade of molluscan purple can be well tracked throughout history due to the structural stability of the primary chromophores providing its color on a multitude of art media such as pottery, paintings, and textiles.[8,9] The chemical identification of molluscan purple is achieved by the detection of brominated-indigotins, such as the 6,6′-dibromoindigotin (Figure 1) which was reported as a coloring constituent of *Murex brandaris* extracts at the beginning of the 20$^{th}$ century.[6,7] Apart from the brominated-indigotins, the color of molluscan purple, is furthermore affected by the brominated-indirubins which, however, are usually reported in small amounts.[4]

One of the most prominent environmental pressures on pigments used in art is their exposure to the sun's rays.[10] However, a material cannot be colored without absorbing visible light. The photostability of a molecule is often inversely related to its excited-state lifetime, which is a measure of how quickly a molecule can return to the ground state upon photoexcitation.[11] While 6,6'-dibromoindigotin has scarcely been studied due to its cost to either synthesize or harvest, the dynamics of indigotin is well established. Initial calculations of the excited-state potential energy surface revealed that the molecule undergoes an intramolecular proton and hydrogen transfer tautomerizing from the diketo to the keto-enol conformation.[12,13] The potential energy surface and the barrier to transfer was later found to be primarily dependent on the N-H coordinate donor and O acceptor distances.[7] Initial solution phase studies sought to observe these calculated proton transfer processes on ultrafast

timescales through fluorescence, transient absorption, and photoisomerization, but found no evidence of the transfer.[15-19] Others tried to monitor the predicted proton transfer by measuring the dynamics of related forms of indigotin such as the reduced leuco-indigotin and the dianion indigotin carmine.[20-24] Those studies could not measure this relaxation channel but did find an ultrafast decay to the ground state.

Haggmark et al. measured the structure, excitation spectra, and excited-state lifetimes of indigotin ($I_o$) in the gas phase to investigate the proposed excited-state intramolecular proton and hydrogen transfer (PT and HT respectively) in a solvent-free environment.[25] In that work we found that unlike in common excited state intramolecular proton (ESIPT) systems, indigotin also exhibits hydrogen transfer as part of its photochemistry. Experimentally we observed two deactivation processes, a faster and a slower one. Calculations predicted two pathways as well, involving PT and HT, respectively, in the excited state and the opposite character (HT and PT) in the ground state trajectories. The excited state potential energy surfaces show trajectories with sequential double proton or hydrogen transfer.[27] There is a narrow spectral range (up to about 1000 $cm^{-1}$ above the origin) in which the partitioning among the two pathways depends strongly on vibrational modes. Above 1000 $cm^{-1}$ the excited state lifetime shortens considerably, providing a mechanism for indigotin's stability against radiative damage.[25-29]

The effects of halogenic substitution on proton transfer have been studied extensively due to its diverse applications in electronics, solar cells, and its presence in biological systems.[30] Typically, the addition of a strong electron-accepting group to a molecule draws electron density away from the proton increasing the rate of transfer. Studies on structures similar to the diketo indigotin tautomer found that fluorination also stabilizes the compound with a high

dependence on the position of the substitution and results in changes in the rate of excited-state lifetime.[31]

Here we present the absorption and excited-state dynamics of 6,6'-dibromoindigotin in the gas phase using resonance enhanced multi-photon ionization and pump-probe spectroscopy along with calculations of the excited-state potential energy landscape for comparison with its non-brominated form. Bromination of indigotin resulted in a blue-shift of the absorption spectrum near the origin transition. However, the excited state dynamics appears to be very similar to that of $I_o$. Like indigotin, molluscan purple exhibits two distinct decay processes on the order of 1 and 20 ns respectively. Computations of excited state profiles are also very similar to those for $I_o$ with only a ~0.007eV difference in the calculated second proton transfer barrier height. Based on these results, we speculate upon the complete relaxation mechanism of indigotin which we find to be a useful model for the more complex and historically relevant molluscan purple.

## 2.Methods

### 2.1. Experimental

We have described the REMPI technique extensively and thus will only briefly describe the specifics of our experiment here.[28] Molluscan purple was synthesized according to a methodology previously described.[36] Solid molluscan purple was deposited onto a graphite bar and placed into the experiment chamber under high vacuum ($2x10^{-6}$ torr). The sample is then laser desorbed with a focused 1064 nm pulse from a Continuum Minilite I (10 hz, 5 ns pulse width) laser which vaporizes the sample with minimal fragmentation. To continually refresh the material for desorption, the sample substrate is translated with a stepping motor orthogonal to the laser. The vaporized material is entrained in argon pulsed into the chamber

(10hz, 8 Bar backing pressure) cooling the material to ~15 K and directing the material through a skimmer into the mass spectrometer for further analysis.

To measure the excitation spectra and excited-state lifetimes of molluscan purple, REMPI and pump probe spectroscopy were employed. The laser pulses used for both spectroscopic techniques are generated from the third harmonic of an EKSPLA PL2251 Nd:YAG (30ps pulse width, 1064nm fundamental) pumping a PG-401 tunable optical parametric generator capable of producing wavelengths from UV to NIR with 6.5 $cm^{-1}$ resolution and approximately 600 μJ pulses. For R2PI, the wavelength of a tunable visible light pulse is scanned until resonant absorption occurs, promoting the molecule to the excited state. A second pulse produced from $5^{th}$ harmonic generation of the fundamental from the same pump laser source temporally overlapped with the sweeping laser then provides enough energy to ionize the molecule only if successfully excited. The ions are detected using a time-of-flight mass spectrometer providing simultaneous mass and absorption monitoring of 6,6'-dibromoindigotin. To perform pump-probe spectroscopy, the excitation laser is parked on a vibronic transition. A mechanical delay stage (Thorlabs, 300mm delay) in the $5^{th}$ harmonic laser pulse pathway provides up to a 2 ns delay with approximately 6 ps resolution. The relative ion count is measured as a function of delay. A separate ionization pulse generated from the $5^{th}$ harmonic of a Quantel DCR-11 Nd:YAG laser (5ns pulse width, 10 Hz, 8mJ/pulse) electronically delayed by a Stanford Instruments DG-645 delay generator measures the pump probe spectra with nanosecond delay. For both ns and ps pump probe experiments, resultant decay spectra are convolved and fitted to a monoexponential decay in a Mathematica script.[29]

**2.2. Computational**

The methodology used for Molluscan Purple is analogous to the one used for the indigo and deuterated indigo molecules.[27] The equilibrium geometry of the diketo form (Fig. 1) – the most stable planar minimum of Molluscan Purple molecule – in its closed-shell ground electronic state ($S_0$), was determined with the MP2 method [MP2] with $C_s$ symmetry constraint. The MP2 energy of the diketo form in the $S_0$-state is the reference value for all other ground-state and excited-state structures. The excited-state (S1) equilibrium geometries were determined with the second-order algebraic diagrammatic construction ADC(2) method.[22-25] In case Molluscan Purple molecule, the correlation-consistent valence double-zeta basis set with polarization functions on all atoms (ccpVDZ) [DZ-26] was used in these calculations as well as in the calculations of potential energy profiles and surfaces as it was done for indigo molecule.[27] Since bromine atom is the third row element, only for bromine the triple-zeta (cc-pVTZ) basis set was used[DZ-26].

To study the process of the transfer of the two active protons in the excited state of the diketo form, the relaxed potential energy profiles were calculated; first, along the first NH coordinate, $R_1$ (N1-H), and subsequently along the second NH coordinate, $R_2$ (N2-H). For each fixed value of a given NH coordinate the remaining internal nuclear coordinates were optimized.

To simulate the UV absorption spectrum of both molecules the simplified version of the coupled clusters method was used, CC2[CC2] with conjunction with the cc-pVTZ basis set. All calculations were performed using the TURBOMOLE program package [TURBO].

## 3.Results

### 3.1. Experimental Results

Figures 2 A and B show the R2PI spectra of molluscan purple with 30 picosecond and 6 nanosecond ionization laser pulses respectively. Both spectra use the same excitation laser, but a different ionization laser depending on the timescale required. The origin transition was found to be at 18416 $cm^{-1}$, a 267 $cm^{-1}$ blue shift relative to indigotin. Absorption spectra in a solution of DMF were reported with a similar although smaller shift.[20] This shift agrees with the calculated excitation energy found in Table 1. Both spectra were plotted as a function of excess energy with respect to the origin transition. We distinguish two regions of excitation, one, denoted as A, spanning from the origin to approximately 500 $cm^{-1}$ excess energy and the other, denoted as B, at higher excess energy. Region A shows peaks with both picosecond and nanosecond ionization and region B only shows peaks with picosecond ionization. The longer pulse width laser is less efficient at ionizing excited states with sub-nanosecond lifetimes.

We performed pump-probe spectroscopy with picosecond and nanosecond delays (using picosecond and nanosecond ionization pulses, respectively) to measure the excited-state lifetimes of molluscan purple. In our previous study of non-substituted indigotin ($I_0$), we found two decays for excitation energies in region A on the order of 1 and 20 ns.[23,24] Only the diketo tautomer was observed in the indigotin experiment, we assume this remains true for 6,6'-dibromoindigotin. Figure 4A shows the picosecond delay pump probe spectrum at the origin transition, which can be fit monoexponentially to an approximate 2.5 ns lifetime. This lifetime was about 1.5 ns slower than the origin transition of $I_0$ but within the same order of magnitude of the lifetimes measured in region A of normal indigotin. Figure 5 shows a pump-probe spectrum of the origin transition with nanosecond delay, fit to a 20 ns excited-state lifetime. As discussed below, these lifetimes are of the same order as those for $I_0$ and the differences between are within the precision of the fitting algorithm (100 ps for the ps pump probe, 3 ns

for the ns pump probe). Measurement of a higher energy transition, found in Figure S1, produced analogous lifetimes on this time scale.

### 3.2. Computational Results

Bromination at the 6 and 6' sites of indigotin shift the electron density of indigotin towards the halogens potentially influencing the shape of the previously calculated sequential double-proton transfer landscape. To confirm this, we modelled the excited-state PES (filled in squares and triangles) as well as in the ground state (empty squares and triangles) at the ADC(2)/cc-pVDZ and MP2/cc-pVDZ level respectively. Figure 3 displays the calculated lowest energy 1-D trace of one trajectory of the excited-state and ground-state potential energy surfaces (PES) of molluscan purple as a function of these two coordinates.

The overall landscape of the PES is strikingly like indigotin. 6,6'-dibromoindigotin retains the same $C_S$ symmetry as indigotin making the order of the protons transferring indistinguishable. Additionally, since only the trans-diketo tautomer was present in the cold jet of the experiment, we assume 6,6'-dibromoindigotin is present only in this form in the ground state as well as upon excitation within the Franck-Condon region. It was found in all indigotin analogues that the enol-enol conformer formed from isomerization via double proton transfer is located at a local minimum on the excited-state PES. However, the barrier for concerted double-proton transfer to this conformation is significantly higher than the competing sequential process and is deemed not probable to occur. Calculations were first performed by freezing the first transfer coordinate, denoted $N_1H$, at various positions and optimizing the remaining coordinates to calculate their energies. These measurements are found in the left half of Figure 3. The resulting computations suggest a small barrier (0.1 eV high) to transfer as the $N_1H$ coordinate stretched to about 1.2 Å. Beyond the barrier, two

trajectories that were nearly isoenergetic in the Franck-Condon region, X (red triangles) and Y (blue squares), begin to deviate in energy and form two distinct keto-enol photoproducts of the first transfer. The relative energies of the X and Y products are 1.893 and 1.869 eV, both lower in energy than the corresponding $I_0$ products. These two states differ in the amount of electric charge carried during the transfer, and we denote them as the first proton and hydrogen transfers respectively. Additionally, the center C-C bond in 6,6'-dibromoindigotin is significantly longer in the X trajectory (1.453 Å) than the Y (1.383 Å), as seen in Table 2. The lengths of both trajectories are the same as $I_0$. As the coordinate is stretched further beyond the barrier, the two states remain close in energy.

The right half of Figure 3 similarly freezes the second transfer coordinate, $N_2H$, at various distances and plots the energies of the optimized structures for both the X and Y paths. Stretching this coordinate to about 1.3 angstroms in both conformers results in the formation of a second barrier to transfer. However, unlike the barrier in the $N_1H$ coordinate, the barriers in the X and Y trajectories differ greatly, with heights of 0.117 eV and 0.382 eV respectively. Beyond these barriers both trajectories form conical intersections with the ground-state trace, leading to a ground-state intramolecular back transfer which reforms the trans-diketo conformation.

Bromine substitution on both donor sides of the sequential ESIPT and ESIHT mechanisms results in a small shift of the calculated potential energy surface compared to indigotin slightly altering the dynamics of the transfer process. The first transfer barrier had no change in height compared to indigotin. However, both the X and Y barriers to transfer showed slight decreases in height relative to the indigotin barrier, 0.007 and 0.019 eV respectively. Additionally, the gap between the peaks of the two barriers increased by 0.012 eV from 0.253 eV in indigotin

to 0.265 eV in molluscan purple, suggesting an increased preference to proceed along the X pathway. The fluorescence lifetimes of the keto-keto tautomer and the HT and PT products were also calculated to be 10, 5.4, and 2.3 ns respectively. The keto-keto and X states fluoresced 0.8 ns faster than $I_0$ and the Y state by 0.1 ns.

## 4.Discussion

### 4.1 REMPI

The signal to noise in the REMPI spectra is quite poor as a consequence of the small amount of the precious material we had available, which limited the amount of signal averaging we could perform. Therefore a detailed vibronic analysis is not possible. Nevertheless, two observations stand out. First, the origin is blue-shifted relative to that of $I_o$ by 267 $cm^{-1}$, matching the 0.02 eV increase in excitation energy calculated to reach the $S_1$ for Molluscan Purple found in Table 1. Secondly, the ns ionization spectrum exhibits a sharp cut-off at 500 compared to 1000 $cm^{-1}$ in the case of $I_o$. This cut-off indicates the energy beyond which the excited state lifetime becomes too short to allow ionization by the 6 ns pulses of the ionization laser.

### 4.2 Excited-State Dynamics

To completely model the excited-state dynamics, dynamics simulations are required which is beyond the scope of this experimental study. However, we will speculate on the possible processes the indigotin family utilizes to remain photostable and discuss how the dibromo analogue of indigotin provides new insight towards identifying the mechanism.

In our earlier studies of unsubstituted indigotin pump-probe measurements at each vibronic transition in the absorption spectrum showed that upon excitation in the Frank Condon region, indigotin relaxes on two distinct time scales on the order of 1 and 20 ns.[25]

Accompanying computational calculations of the excited-state potential energy surface (PES) measured as a function of the $N_1$-H coordinate responsible for excited-state intramolecular proton and hydrogen transfer indicated that upon overcoming a 0.1 eV barrier to transfer, two distinct trajectories form that are nearly isoenergetic, X and Y. Along the second $N_2$-H coordinate present in the indigotin molecule the two trajectories deviate in energy, both forming a second barrier to transfer. The barrier on the Y trajectory is approximately 0.3 eV higher than for X, and we tentatively assigned the faster lifetime measurement to X and slower to Y. We selectively substituted the hydrogens that take part in excited-state intramolecular proton and hydrogen transfer and found that only the faster relaxation process was affected by the kinetic isotope effect (KIE).[27] We concluded that the faster mechanism involves tunneling through at least one of the barriers on the PES. These results may indicate that the longer lifetime involves a process not affected by deuteration such as fluorescence or relaxation along an entirely different reaction coordinate.

The measured pump probe spectra of dibromo indigotin on the nanosecond and picosecond timescales showed no change in lifetime compared to indigotin. Furthermore, the calculated PES showed minimal change to the trajectories pre- and post-hydrogen and proton transfer, suggesting that the indigotin analogue uses the same mechanisms to relax as $I_0$. While the two measured mechanisms cannot be definitively assigned, we discuss below how the bromination effects each of the fast and slow proposed mechanisms.

### 4.2.1 The Fast Process

The effect of substitution with strong electron-withdrawing groups on excited-state proton and hydrogen transfer has been studied previously in theoretical studies.[30] From these calculations, a few key characteristics arose that impact the transfer processes. One such

finding was that halogenic substitution on the donor side stabilized the pre-proton transfer tautomer in the ground and excited state while acceptor side substitution stabilized the post-transfer product.[31] However, while the proton transfer product is slightly lower in energy when substituted on the acceptor side, the barrier to transfer increased and the converse effect occurred for donor side substitution. Another study, selectively substituting a fluorine atom onto a polyaromatic hydrocarbon, found that placement of the fluorine para to the hydrogen transfer donor favored the forward transfer strongly, while the back transfer rates in the ground state greatly diminished and the overall rate decreased.[32] Meta substitution increased the rates of both, illuminating the importance of the distance of the electrophilic group to the transfer site.

For 6,6'-dibromoindigotin, both bromine substitutions occur on the donor side of the excited-state transfer sites likely stabilizing the keto tautomer in the excited and ground state.[31] Additionally, we found a decrease in the second barrier height on the excited-state potential energy surface compared to $I_0$ which could increase the tunneling rate and lower the lifetime. However, we observed no significant change in the excited-state lifetime of the faster process. Measurements of the kinetic isotope effect point towards a tunneling mechanism, but it is not conclusive which of the two tunneling processes were involved. It is of note that the experimental measurements and calculated PES do not account for any possible changes in the rate of the ground state back transfer which others have found to shift with halogen substitution. But like in the excited state, the change in the potential energy landscape in the ground state and therefore the back transfer rate due to bromination should not change significantly. While a faster rate of ESIPT and ESIHT are both predicted from the lower barrier on the calculated surface since tunneling is involved and from previous studies of

donor-side halogenic substitution, we postulate that this change in rate was not observed in the pump probe spectrum because: (1) the calculated barrier height change was too small to have an effect on the tunneling rate, large enough to be observed with the limited resolution afforded by our fitting algorithm, and (2) the bromine is sufficiently far enough away from the donor-acceptor sites to not influence the transfer processes.

The difference between $I_0$ and dibromoindigotin's calculated fluorescence lifetimes from the X and Y photoproducts are smaller than the resolution of the pump probe experiments. These lifetimes are also close in value to the measured lifetime of the fast process. Through these observations, we conclude that it is likely that the fast process measured for dibromoindigotin utilizes the same tunneling mechanism as $I_0$. Upon tunneling through the barrier along the $N_1$-H coordinate forming the X and Y photoproduct, both indigotin and molluscan purple can fluoresce from these states. It is also possible that because the second barrier to transfer is low along the X trajectory, the molecule reaches the conical intersection to the ground state. Tunneling through the second barrier along the Y trajectory is unlikely on this timescale because the barrier is too high. After reaching the ground state, a ground state intramolecular hydrogen or proton transfer occurs as calculated for indigotin, reforming the keto-keto tautomer. However, it is not possible to assign which relaxation pathway the indigotins utilize without further dynamics of the excited-state PES.

### 4.2.2 The Slower Process

Similarly, the slower process showed no measurable difference in excited-state lifetime compared to the analogous indigotin decay. This decay could be due to a number of processes. (1) Trapping behind the large barrier in the Y trajectory, followed by adiabatic transfer to the X trajectory. In this case, the small change to the height of the barrier due to bromine

substitution would not affect the orders of magnitude slower interconversion to the X trajectory. (2) Fluorescence from the diketo or keto-enol tautomers or (3) a movement to another surface potential through intersystem crossing or internal conversion.

The impact of substitution of heavier atoms and functional groups on lifetime is thoroughly explored in the literature. Theoretical studies have shown that heavy atom substitution increases the rate and quantum yield of intersystem crossing due to increased spin-orbit coupling. This trend has been corroborated experimentally, including for thio- and seleno-substituted indigotin.[33-35] Further solution phase studies of molluscan purple and other substituted indigotins in both the diketo and leuco forms showed that in addition to an increase in intersystem crossing quantum yields, only the fluorescence yields decreased amongst the available competing mechanisms.

Like the fast process, it is unclear which of the possible mechanisms indigotin uses to reach the ground state on this time scale, but we suspect molluscan purple to use the same process. We will speculate upon the possible relaxation mechanisms further. An entrapment on the Y trajectory until interconversion to the X pathway would not exhibit a kinetic isotope effect on this timescale and not be affected by bromination. However, the calculated fluorescence lifetime from the Y state provides a much faster pathway to the ground state and would be in direct competition with this process. Fluorescence from the keto-keto or X trajectory and intersystem crossing occur on the same order of magnitude as the 20 ns lifetime measured. However, similar lifetime studies found that bromination affects the rate of these channels. Future measurements and calculations may also find evidence for an undiscovered trajectory to the ground state that matches the lifetime trends uncovered in these experiments.

**5.Conclusion**

We present REMPI spectra, pump-probe spectra, and calculated 1-D traces for sequential double proton and hydrogen transfer along the excited and ground-state potential energy surfaces of 6,6'-dibromoindigotin, the primary chromophore in the ancient dye known as molluscan purple. Other than a blue-shift in the absorption spectra, molluscan purple shares similar photo-relaxation mechanisms with indigotin: a faster sequential double proton transfer along the X trajectory followed by a back transfer and a slower interconversion from the Y trajectory to the X profile and followed by the same process. While halogenic substitution in other molecular systems has led to changes in the calculated potential energy surfaces and consequently the rate to transfer, bromination had little effect on the excited-state lifetimes of both decay processes compared to the indigotin molecule. The striking similarities between the measured lifetimes and calculated PES for both indigotin and molluscan purple illustrate the hardiness of the two dyes to harmful photodamage as well as the importance of modelling analogous molecules to predict the effects of more complex systems.

**Figures**

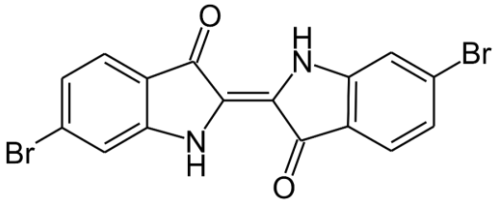


Figure 1: The chemical structure of 6,6'-dibromoindigotin (molluscan purple) in the trans-diketo tautomeric form.

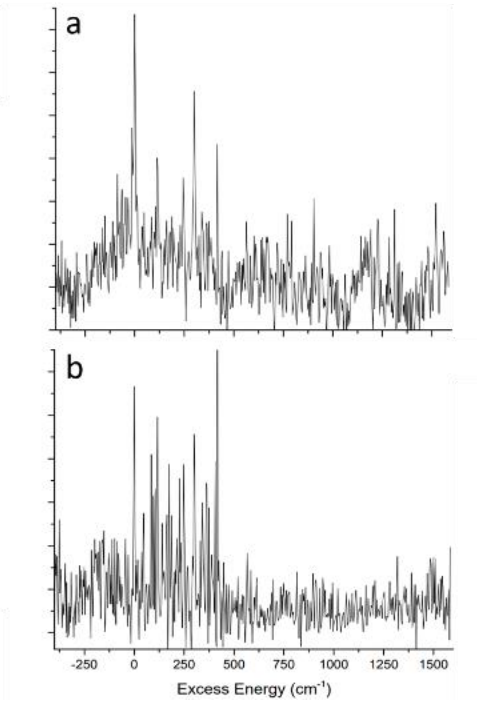


Figure 2: R2PI spectra of molluscan purple with picosecond (a) and nanosecond (b) ionization. The spectra were plotted in excess energy with respect to the origin.

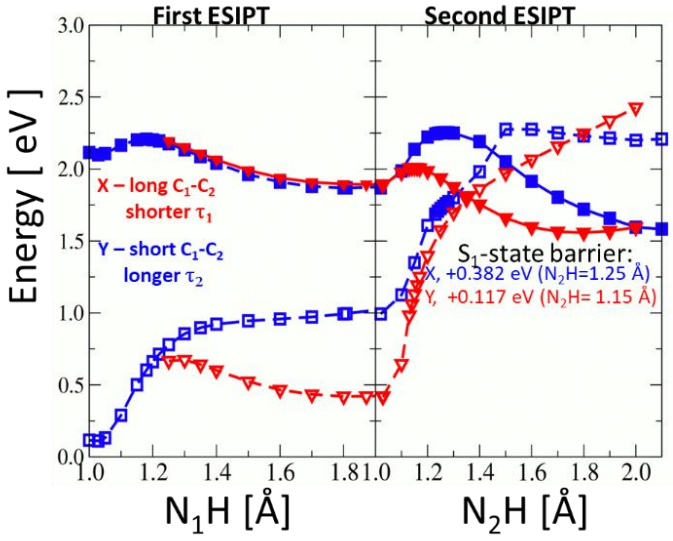


Figure 3: A two-dimensional trace of the lowest energy pathway of the excited state (filled shapes) to the ground state surface (empty shapes) along the $N_1H$ coordinate (left half) and the $N_2H$ coordinate (right half). Upon overcoming the first barrier to transfer along the

$N_1H$ trajectory, two pathways, X and Y, form. Overcoming the second barrier to transfer leads to a conical intersection back to the ground state and an eventual ground state intramolecular proton transfer back to the lowest energy trans-diketo tautomer.

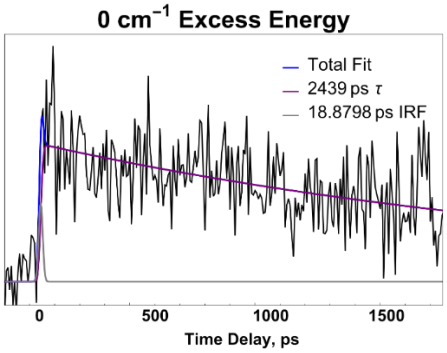


Figure 4: Pump probe of molluscan purple taken with a picosecond delay at the origin transition.

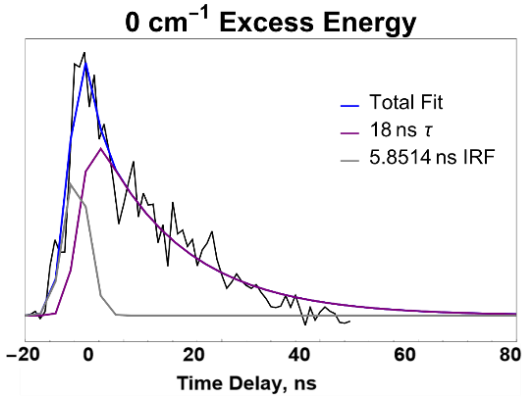


Figure 5: Pump probe of the origin transition with nanosecond delay.

| | **Molluscan Purple** | | | **Indigo** | |
|---|---|---|---|---|---|
| | $\Delta E^{VE}$ | f | | $\Delta E^{VE}$ | f |
| $S_0$ | 0.0 | | | 0.0 | |
| $S_1(\pi\pi^*)$ | 2.30 | 0.3964 | | 2.28 | 0.3535 |

| | | | | | |
|---|---|---|---|---|---|
| $S_2(\pi\pi^*)$ | 3.14 | 0.0000 | | 3.13 | 0.0000 |
| $S_3(\pi\pi^*)$ | 3.70 | 0.0000 | | 3.79 | 0.0000 |
| $S_4(\pi\pi^*)$ | 4.10 | 0.6135 | | 4.41 | 0.4066 |
| $S_5(\pi\pi^*)$ | 4.40 | 0.5218 | | 4.45 | 0.2011 |
| $S_5(\pi\pi^*)$ | 4.42 | 0.0000 | | 4.60 | 0.0000 |

Table 1: Table- UV absorption spectra of Indigo *vs.* Molluscan Purple in their diketto form calculated with the CC2/cc-pVTZ method at the geometry oprimed at the MP2/cc-pVDZ theory level

| | **cc-pVDZ** | | | | **cc-pVTZ** | | |
|---|---|---|---|---|---|---|---|
| **Indigotin, ground state** | | | | | | | |
| | **diketo** | **X, enol-keto** | **Y, enol-keto** | | **diketo** | **X, enol-keto** | **Y, enol-keto** |
| **$S_0$** [eV] | 0.00 | - | 0.126 | **$S_0$** | 0.00 | - | - |
| **$\mu_g$** [D] | 0.00 | - | 2.38 | **$\mu_g$** | 0.00 | - | - |
| **$C_1$-$C_2$** [Å] | 1.378 | - | 1.421 | **$C_1$-$C_2$** | 1.365 | - | - |
| **Indigotin, excited state** | | | | | | | |
| **$S_1$[a]** [eV] | 2.087 | 1.899 | 1.875 | **$S_1$[a]** | 2.031 | 1.851 | 1.824 |
| **$E_{fl}$** [eV] | 1.977 | 1.462 | 0.841 | **$E_{fl}$** | 1.922 | 1.388 | 0.785 |
| **$\mu_e$** [D] | 0.0 | 6.76 | 3.39 | **$\mu_e$** | 0.00 | 6.89 | 3.64 |

| | | | | | | | |
|---|---|---|---|---|---|---|---|
| **f** | 0.289 | 0.198 | 0.097 | **f** | 0.273 | 0.1783 | 0.0838 |
| **$C_1$-$C_2$** [Å] | 1.392 | 1.454 | 1.383 | **$C_1$-$C_2$** | 1.385 | 1.443 | 1.371 |
| **$\tau_r$** [ns] | | | | | **10.8** | **6.2** | **2.4** |
| **Molluscan Purple, $S_0$** | | **cc-pVDZ** | | | | **cc-pVTZ** | |
| | **diketo** | **X, enol-keto** | **Y, enol-keto** | | **diketo** | **X, enol-keto** | **Y, enol-keto** |
| **$S_0$** [eV] | 0.00 | - | 0.124 | **$S_0$** | 0.00 | - | 0.142 |
| **$\mu_g$** [D] | 0.0 | - | 1.51 | **$\mu_g$** | 0.00 | - | 1.38 |
| **$C_1$-$C_2$** [Å] | 1.377 | - | 1.420 | **$C_1$-$C_2$** | 1.364 | - | 1.406 |
| **Molluscan Purple, excited state** | | | | | | | |
| **$S_1^a$** [eV] | 2.098 | 1.893 | 1.869 | **$S_1^a$** | 2050 | 1.850 | 1.819 |
| **$E_{fl}$** [eV] | 1.988 | 1.473 | 0.875 | **$E_{fl}$** | 1.941 | 1.404 | 0.810 |
| **$\mu_e$** [D] | 0.0 | 6.89 | 3.19 | **$\mu_e$** | 0.0 D | 7.03 | 3.48 |
| **f** | 0.3215 | 0.2334 | 0.1154 | **f** | 0.3057 | 0.213 | 0.0972 |
| **$C_1$-$C_2$** [Å] | 1.397 | 1.453 | 1.383 | **$C_1$-$C_2$** | 1.385 | 1.441 | 1.370 |
| **$\tau_r$** [ns] | | | | | **10** | **5.4** | **2.3** |

Table 2: A comparison of the calculated ground and excited energies ($S_0$, $S_1$), fluorescence energy ($E_{fl}$), dipole moment ($\mu_g$, $\mu_e$), oscillator strength (f), and $C_1$-$C_2$ bond length of the diketo and enol-keto tautomers between indigotin and molluscan purple calculated using MP2/cc-pVDZ for the $S_0$ and ADC(2)/cc-pVDZ for the $S_1$. The calculated fluorescence lifetimes ($\tau_f$, in blue) are shortened in all calculated conformations of molluscan purple.

Supplemental Information

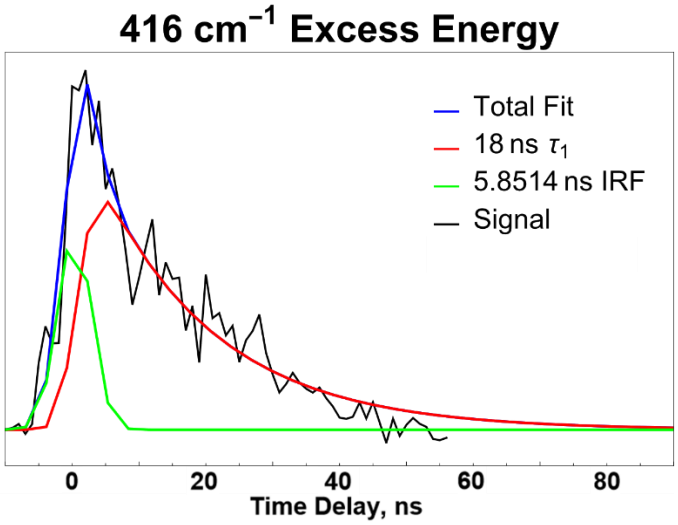


Figure S1: A measure of the excited-state lifetime using pump probe spectroscopy with nanosecond delay measured at a transition 416 $cm^{-1}$ excess in energy relative to the origin transition.

**References**

(1) Karapanagiotis, I.; A Review on the Archaeological Chemistry of Shellfish Purple. *Sustainability* **2019**, 11, 3595. DOI: 10.3390/su11133595.

(2) Sotiropoulou, S.; Karapanagiotis, I.; Andrikopoulos, K.S.; Marketou, T.; Birtacha, K.; Marthari, M. Review and New Evidence on the Molluscan Purple Pigment Used in the Early Late Bronze Age Aegean Wall Paintings. *Heritage* **2021**, *4*, 171–187. DOI: 10.3390/heritage4010010.

(3) Melo, M.J. History of Natural Dyes in the Ancient Mediterranean Civilization. In, Handbook of Natural Colorants, 2nd Ed. Betchtold, T; Manian, A.P., Pham, T. (Eds.), 2023 John Wiley & Sons Ltd. DOI: 10.1002/9781119811749.ch1.

(4) Karapanagiotis, I.; Mantzouris, D.; Cooksey, C.; Mubarak, M.S.; Tsiamyrtzis, P. An Improved HPLC Method Coupled to PCA for the Identification of Tyrian Purple in Archaeological and Historical Samples. *Microchemical Journal* **2013**, 110 70–80. DOI: 10.1016/j.microc.2013.02.008.

(5) Karapanagiotis, I.; Sotiropoulou, S.; Vasileiadou, S.; Karagiannidou, E.; Mantzouris, D.; Tsiamyrtzis, P. Shellfish Purple and Gold Threads from a Late Antique Tomb Excavated in Thessaloniki. *Arachne* **2018**, *5*, 64–77.

(6) Friedlaender, P. Zur Kenntnis des Farbstoffs des antiken Purpurs aus *Murex brandaris*. *Monatshefte für Chemie* **1907**, *28*, 991–996. DOI: 10.1007/BF01510338.

(7). Friedländer, P. Über den Farbsto des antiken Purpurs aus M*urex brandaris*. *Ber. Dtsch. Chem. Ges.* **1909**, *42*, 765–770. DOI: 10.1002/cber.190904201122.

(8) Clark, R. J. H.; Cooksey, C. J.; Daniels, M. A. M.; Withnall, R. Indigo, Woad, and Tyrian Purple - Important Vat Dyes from Antiquity to the Present. *Endeavour* **1993**, *17* (4), 191-199. DOI: Doi 10.1016/0160-9327(93)90062-8.

(9) Splitstoser, J. C.; Dillehay, T. D.; Wouters, J.; Claro, A. Early pre-Hispanic use of indigo blue in Peru. *Sci Adv* **2016**, *2* (9), e1501623. DOI: 10.1126/sciadv.1501623 From NLM Medline.

(10) Christie, R. M. Why is indigo blue? *Biotech Histochem* **2007**, *82* (2), 51-56. DOI: 10.1080/00958970701267276.

(11) Otterstedt, J. A. Photostability and Molecular-Structure. *J Chem Phys* **1973**, *58* (12), 5716-5725. DOI: Doi 10.1063/1.1679196.

(12) Yamazaki, S.; Sobolewski, A. L.; Domcke, W. Molecular mechanisms of the photostability of indigo. *Physical Chemistry Chemical Physics* **2011**, *13* (4), 1618-1628. DOI: 10.1039/c0cp01901a.

(13) Iwakura, I.; Yabushita, A.; Kobayashi, T. Why is Indigo Photostable over Extremely Long Periods? *Chem Lett* **2009**, *38* (11), 1020-1021. DOI: 10.1246/cl.2009.1020.

(14) Douhal, A.; Lahmani, F.; Zewail, A. H. Proton-transfer reaction dynamics. *Chem Phys* **1996**, *207* (2-3), 477-498. DOI: Doi 10.1016/0301-0104(96)00067-5.

(15) Wyman, G. M.; Zarnegar, B. M. Excited-State Chemistry of Indigoid Dyes .2. Interaction of Thioindigo and Selenoindigo Dyes with Hydroxylic Compounds and Its Implications on Photostability of Indigo. *J Phys Chem-Us* **1973**, *77* (10), 1204-1207. DOI: DOI 10.1021/j100629a004.

(16) Miehe, G.; Susse, P.; Kupcik, V.; Egert, E.; Nieger, M.; Kunz, G.; Gerke, R.; Knieriem, B.; Niemeyer, M.; Luttke, W. Theoretical and Spectroscopic Investigations of Indigo Dyes .23. Light-Absorption as Well as Crystal and Molecular-Structure of N,N'-Dimethylindigo - an Example of the Use of Synchrotron Radiation. *Angew Chem Int Edit* **1991**, *30* (8), 964-967. DOI: DOI 10.1002/anie.199109641.

(17) Pina, J.; Sarmento, D.; Accoto, M.; Gentili, P. L.; Vaccaro, L.; Galvao, A.; de Melo, J. S. S. Excited-State Proton Transfer in Indigo. *J Phys Chem B* **2017**, *121* (10), 2308-2318. DOI: 10.1021/acs.jpcb.6b11020.

(18) Bernardino, N. D.; Brown-Xu, S.; Gustafson, T. L.; de Faria, D. L. A. Time-Resolved Spectroscopy of Indigo and of a Maya Blue Simulant. *J Phys Chem C* **2016**, *120* (38), 21905-21914. DOI: 10.1021/acs.jpcc.6b04681.

(19) Grimme, G.; Grimme, S.; Jones, P. G.; Boldt, P. Am1 and X-Ray Studies of the Structures and Isomerization-Reactions of Indigo Dyes. *Chem Ber-Recl* **1993**, *126* (4), 1015-1021. DOI: DOI 10.1002/cber.19931260423.

(20) Moreno, M.; Ortiz-Sanchez, J. M.; Gelabert, R.; Lluch, J. M. A theoretical study of the photochemistry of indigo in its neutral and dianionic (leucoindigo) forms. *Phys Chem Chem Phys* **2013**, *15* (46), 20236-20246. DOI: 10.1039/c3cp52763h From NLM Medline.

(21) Rondao, R.; de Melo, J. S.; Melo, M. J.; Parola, A. J. Excited-State Isomerization of Leuco Indigo. *J Phys Chem A* **2012**, *116* (11), 2826-2832. DOI: 10.1021/jp211996f.

(22) de Melo, J. S.; Moura, A. P.; Melo, M. J. Photophysical and spectroscopic studies of Indigo derivatives in their keto and leuco forms. *J Phys Chem A* **2004**, *108* (34), 6975-6981. DOI: 10.1021/jp049076y.

(23) Chatterley, A. S.; Horke, D. A.; Verlet, J. R. R. On the intrinsic photophysics of indigo: a time-resolved photoelectron spectroscopy study of the indigo carmine dianion. *Physical Chemistry Chemical Physics* **2012**, *14* (46), 16155-16161. DOI: 10.1039/c2cp43275g.

(24) Roy, P. P.; Shee, J.; Arsenault, E. A.; Yoneda, Y.; Feuling, K.; Head-Gordon, M.; Fleming, G. R. Solvent Mediated Excited State Proton Transfer in Indigo Carmine. *J Phys Chem Lett* **2020**, *11* (10), 4156-4162. DOI: 10.1021/acs.jpclett.0c00946.

(25) Haggmark, M. R.; Gate, G.; Boldissar, S.; Berenbeim, J.; Sobolewski, A. L.; de Vries, M. S. Evidence for competing proton-transfer and hydrogen-transfer reactions in the S-1 state of indigo. *Chem Phys* **2018**, *515*, 535-542. DOI: 10.1016/j.chemphys.2018.09.027.

(26) Leyh, B. Ion Dissociation Kinetics in Mass Spectrometry. *Encyclopedia of Spectroscopy and Spectrometry, 3rd Edition, Vol 2: G-M* **2017**, 300-308. DOI: 10.1016/B978-0-12-409547-2.05195-7.

(27) Cohen, T., Svadlenak, N., Smith, C. *et al.* Excited-state dynamics of deuterated indigo. *Eur. Phys. J. D* **77**, 168 (2023). https://doi.org/10.1140/epjd/s10053-023-00744-z

(28) Meijer, G.; Devries, M. S.; Hunziker, H. E.; Wendt, H. R. Laser Desorption Jet-Cooling of Organic-Molecules - Cooling Characteristics and Detection Sensitivity. *Appl Phys B-Photo* **1990**, *51* (6), 395-403. DOI: Doi 10.1007/Bf00329101.

(29) Siouri, F. M.; Boldissar, S.; Berenbeim, J. A.; de Vries, M. S. Excited State Dynamics of 6-Thioguanine. *J Phys Chem A* **2017**, *121* (28), 5257-5266. DOI: 10.1021/acs.jpca.7b03036.

(30) Stasyuk, A. J.; Cywinski, P. J.; Gryko, D. T. Excited-state intramolecular proton transfer in 2 '-(2 '-hydroxyphenyl)imidazo[1,2-a]pyridines. J Photoch Photobio C 2016, 28, 116-137. (Review of PT and substitution)

(31) Fores, M.; Scheiner, S. Effects of chemical substitution upon excited state proton transfer. Fluoroderivatives of salicylaldimine. *Chem Phys* **1999**, *246* (1-3), 65-74. DOI: Doi 10.1016/S0301-0104(99)00179-2.

(32) Yang, W. J.; Chen, X. B. Dual fluorescence of excited state intra-molecular proton transfer of HBFO: mechanistic understanding, substituent and solvent effects. Physical Chemistry Chemical Physics 2014, 16 (9), 4242-4250. DOI: 10.1039/c3cp54462a.

(33) Becker, R. S. *Theory and interpretation of fluorescence and phosphorescence*; Wiley Interscience, 1969.

(34) Vanhaver, P.; Vanderauweraer, M.; Viaene, L.; Deschryver, F. C.; Verhoeven, J. W.; Vanramesdonk, H. J. Chem Phys Lett 1992, 198 (3-4), 361-366. DOI: Doi 10.1016/0009-2614(92)85065-I. (Enhanced ISC with heavy atom effect)

(35) Rae, M.; Perez-Balderas, F.; Baleizao, C.; Fedorov, A.; Cavaleiro, J. A.; Tome, A. C.; Berberan-Santos, M. N. J Phys Chem B 2006, 110 (25), 12809-12814. DOI: 10.1021/jp061010a (Bromination of C60)

(36) Karapanagiotis, I.; Mantzouris, D.; Cooksey, C.; Mubarak, M. S.; Tsiamyrtzis, P. An improved HPLC method coupled to PCA for the identification of Tyrian purple in archaeological and historical samples. *Microchem J* **2013**, *110*, 70-80. DOI: 10.1016/j.microc.2013.02.008.

(37) [MP2]= C. M∅ller and M. S. Plesset, Phys. Rev., 1934, 46, 618–622.

(38) [ADC2-1]= C. Hättig, Adv. Quantum Chem. **50**(50), 37 (2005)

(39) [ADC2-2]= J. Schirmer, Phys. Rev. A **26**(5), 2395 (1982)

(40) [ADC2-3]= A.B. Trofimov, J. Schirmer, J. Phys. B At. Mol. Opt. **28**(12), 2299 (1995)

(41) [ADC2-4]= D. Tuna, D. Lefrancois, L. Wolanski, S. Gozem, I. Schapiro, T. Andruniow, A. Dreuw, M. Olivucci, J.Chem. Theory Comput. **11**(12), 5758 (2015)

(42) [CC2]= O. Christiansen, H. Koch and P. Jorgensen, Chem. Phys. Lett., 1995, 243, 409–418; C. Hättig and F. Weigend, J. Chem. Phys., 2000, 113, 5154–5161.

(43) [TURBO]= TURBOMOLE V7.5.1 2016, a development of University of Karlsruhe and Forschungszentrum Karlsruhe GmbH, 1989-2007, TURBOMOLE GmbH, since 2007; available from https://www.turbomole.com.

## *III. Excited State Intramolecular Proton Transfer in Hydroxyanthraquinones: Predicting Fading of Organic Red Colorants in Art*

**Authors**

J.A. Berenbeim,[1] S. Boldissar,[1] S. Owens,[1] M.R. Haggmark,[1] G. Gate,[1] F.M. Siouri,[1] T. Cohen,[1] M. F. Rode,[2] C. Schmidt Patterson,[3] and M.S. de Vries[1]*

**Affiliations**

[1] Department of Chemistry and Biochemistry, University of California Santa Barbara, California, USA.

[2] Institute of Physics, Polish Academy of Sciences**,** Al. Lotnikow 32/46 02-668, Warszawa Poland.

[3] Getty Conservation Institute, 1200 Getty Center Drive, Suite 700, Los Angeles, California, USA.

**Abstract**

Compositionally similar organic red colorants in the anthraquinone family, whose photodegradation can cause irreversible color and stability changes, have long been used in works of art. Different organic reds, and their multiple chromophores, suffer degradation disparately. Understanding the details of these molecules' degradation, therefore, provides a window into their behavior in works of art, and may assist the development of improved conservation methods. According to one proposed model of photodegradation dynamics, intramolecular proton transfer provides a kinetically favored decay pathway in some photo-

excited chromophores, preventing degradation-promoting electron transfer (ET). To further test this model, we measured excited state lifetimes of substituted gas phase anthraquinones, utilizing high-level theory to explain the experimental results. The data show a general structural trend: anthraquinones with 1,4-OH substitution are long-lived and prone to damaging ET, while excited state intramolecular proton transfers promote efficient quenching for hydroxyanthraquinones that lack this motif.

## Introduction

Exposure to light degrades many molecules when absorption of ultraviolet and visible wavelength photons places them in an energetically excited state prone to chemical and physical change. Molecules susceptible to photodegradation are ubiquitous in both natural and synthetic systems and undesired effects of such degradation can include a wide range of phenomena, such as the appearance of abnormal skin cells marking melanoma, and the drop of efficiency in polymer solar cells via photo-bleaching. One notable form of organic photodegradation with relevance to the broad field of cultural heritage research is the fading of certain chromophores in works of art, which leads to visual change in a medium where meaning and value is often predicated on color.

Natural organic red colorants of either plant or scale-insect origin are important traditional sources of red hues.[1] These colorants have high tinting strength and are therefore present on artifacts in low concentration; as little as subnanogram concentrations of these colorants may be required to achieve a desired color saturation.[2] Many traditional organic red colorants (including madder, alizarin, cochineal, lac dye, brazilwood, and dragonsblood) are compositionally similar: these anthraquinones (AQ) and hydroxyanthraquinones (HAQ) have long been used as lake pigments and contain primarily hydroxyl, carboxylic acid, and carbonyl

moieties on a conjugated aromatic backbone. While commercial interest in AQs and HAQs has recently expanded to include pharmaceutical applications[3,4], the use of natural AQ derivatives (see Fig. 1) as lake dyes (insoluble dye-mordant complexes, typically precipitated with Al or Ca cations) has long attracted the attention of fine artists and craftsmen, and these pigments continue to be used today. The irreversible fading of organic red colorants in art is well-documented, and greatly affects the perception of masterpieces ranging from antiquity to the present day. Recent publications, for example, have highlighted alteration of organic red colorants in objects as disparate as medieval manuscript illuminations to paintings by Vincent van Gogh.[5-7]

One of the simplest HAQ molecules to be used as a lake pigment is 1,2-dihydroxyanthraquinone (1,2-HAQ), also known as alizarin. Alizarin is produced naturally by multiple species related to *Rubia tinctorum* (common madder) where it is a primary chromophore along with 1,2,4-trihydroxyanthraquinone (1,2,4-HAQ), also known as purpurin.(*1*) It is well documented in the cultural heritage and condensed phase scientific communities that alizarin is more photostable than purpurin.[8-11] Condensed phase photodynamics studies of these AQs suggests that the difference in photostability may stem from an excited state pathway, specifically an excited state intramolecular proton transfer (ESIPT), in alizarin which dissipates photonic energy to regain a stable ground state structure on a timescale much faster than the reaction rates of degradation.[11,12]

ESIPT constitutes one of the fastest reactions known[13,14], and planar organic molecules containing acidic and basic functional groups connected by an intramolecular hydrogen bond often have photophysics driven by such proton transfer. In such molecules, excited state tautomerization occurs through the excitation of the ground state enol-form to an

electronically excited intermediate where a rapid (sub-picosecond timescale), often energetically barrierless, enol to keto proton transfer takes place. Radiationless decay follows this transfer, bringing the excited keto form back to the ground state, and the stable ground state enol reforms through a barrierless back proton transfer.[15] Molecules which undergo ESIPT are typically identified by dual band fluorescence with a large degree of Stokes shift from the ESIPT lower well equilibrium geometry.

Formative work examining this mechanism in AQs/HAQs was done in the 1980s[16]; laser induced fluorescent spectroscopy studies (*17*), including by Flom and Barbara[15], determined that the presence of a dual 1,4- electron donating group (e.g. -OH) precludes dual fluorescence, likely indicating a high barrier towards ESIPT. This qualitative result was later supported by the nodal-plane model by Nagaota.[18] More recent transient spectroscopic work has measured the rate of ESIPT[19-21] as a femtosecond process and correlated this with pigment fading[11,22]. However these are all condensed phase experiments where the effects of secondary molecules cannot be completely excluded, which is particularly important since intermolecular effects are widely known to affect relaxation[20,23]. To measure the unimolecular dynamics of the AQ and HAQ molecules requires gas phase experiments. It should be noted that in the context of art materials, much of the available literature deals only with alizarin and purpurin as exemplars of the HAQ system.[24] Therefore, there remains a need to examine a broader range of these important molecules in the gas phase to fully explicate the observed differences in the relative photostabilities of the basic chromophores themselves. Such a fundamental study can then inform a fuller understanding of the more complex systems found in works of art, which will include binding media, the support, and other pigments in addition to the organic red colorant in question.

In this paper, we address this need, and report an experimental and computational case study on the effects of proton transfer on the excited state lifetimes of seven related HAQs. We measured intrinsic lifetimes of neutral HAQ molecules in a jet-cooled molecular beam by time resolved, pump-probe, two-color (2C) resonant two-photon ionization (R2PI) spectroscopy to elucidate the relaxation dynamics occurring at the lower limit of the excited state potential energy surface (PES). For each molecule studied, these data provide the first 2C R2PI action spectra. We also obtained the excited state lifetimes from both the lowest energy vibronic transition and at higher internal energy (~500-1000 $cm^{-1}$) and, for selected compounds, partial mid-IR characterization of the ground state hydrogen bond vibrations with IR hole burning of the R2PI probe signal. We explore the implications of the resulting data for the photodegradation of these compounds. Our results show a trend of shorter excited state lifetimes for the structures for which there is evidence for ESIPT, as derived from dual fluorescence by Flom and Barbara and others. Both phenomena correlate with structural motifs with specific hydrogen bonding patterns and provide experimental evidence to support predictions for the expected stability of HAQs in works of art.

## Results

### Analytes studied and R2PI spectroscopy

Fig. 1 shows the series of substituted HAQs analyzed. The analytes represent structures with and without the 1,4-OH substitution motif postulated to be determinative of ESIPT properties.[11,15] Several of these molecules are also found in artists' red lake pigments. The molecular structures shown in Fig.1 are planar in all cases. In each molecule the lowest energy (LE) structure (indicated by the Roman numeral I) is that of the 9,10-anthraquinone, with carbonyl groups rather than hydroxyl moieties on the central ring of the backbone. The

interpretation of R2PI and pump-probe spectra requires an understanding of the possible structures present in the molecular beam, which are most likely the lowest energy isomers. Fig. 1 shows all isomers with energies calculated to be within 25 kJ/mol of the lowest energy (LE) structure; isomeric forms with higher energies appear in the supplemental information. The center of Fig. 1 shows the two primary *common madder* chromophores alizarin (1,2-HAQ) and purpurin (1,2,4-HAQ). Both have multiple low energy isomers, as do 1,2,5,8-HAQ and 1,4-HAQ. Three of the molecules examined – 1-HAQ, 1,5-HAQ, and 1,8-HAQ – have only a single lowest energy structure (the rotamers for each of these molecules are 52.3, 53.2, and 47.4 kJ/mol higher in energy than the forms shown, respectively). In the figure and throughout we use the nomenclature of HAQ for all compounds, ignoring the more formal designations of DHAQ and THAQ for the di- and trihydroxy forms, as the numbered prefixes already indicate the number of hydroxyl substituents.

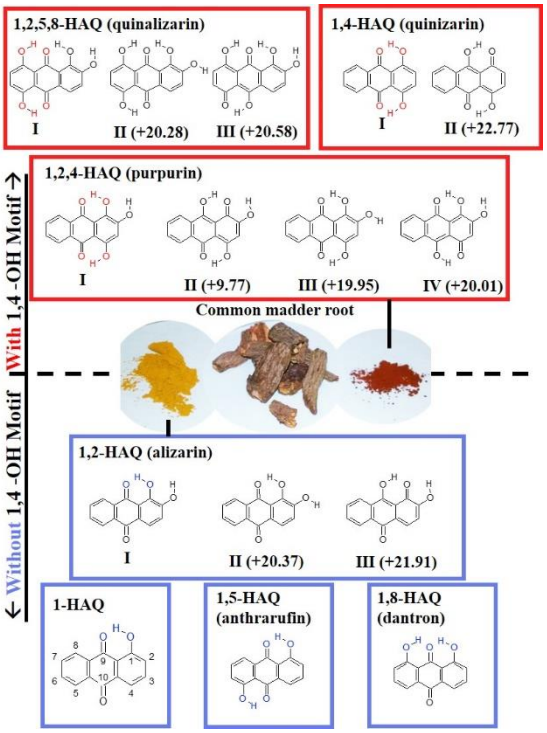

**Fig. 1.** The molecules of this study. Molecules having a 1,4 -OH motif are above the dotted line and those without 1,4 -OH motif are below it. Isomers within ~25 kJ/mol of the lowest energy ZPE corrected structure (labeled I) are also shown with their relative energy values (kJ/mol) with respect to the lowest energy form. Central to this figure is the common madder root and its primary chromophores alizarin and purpurin.

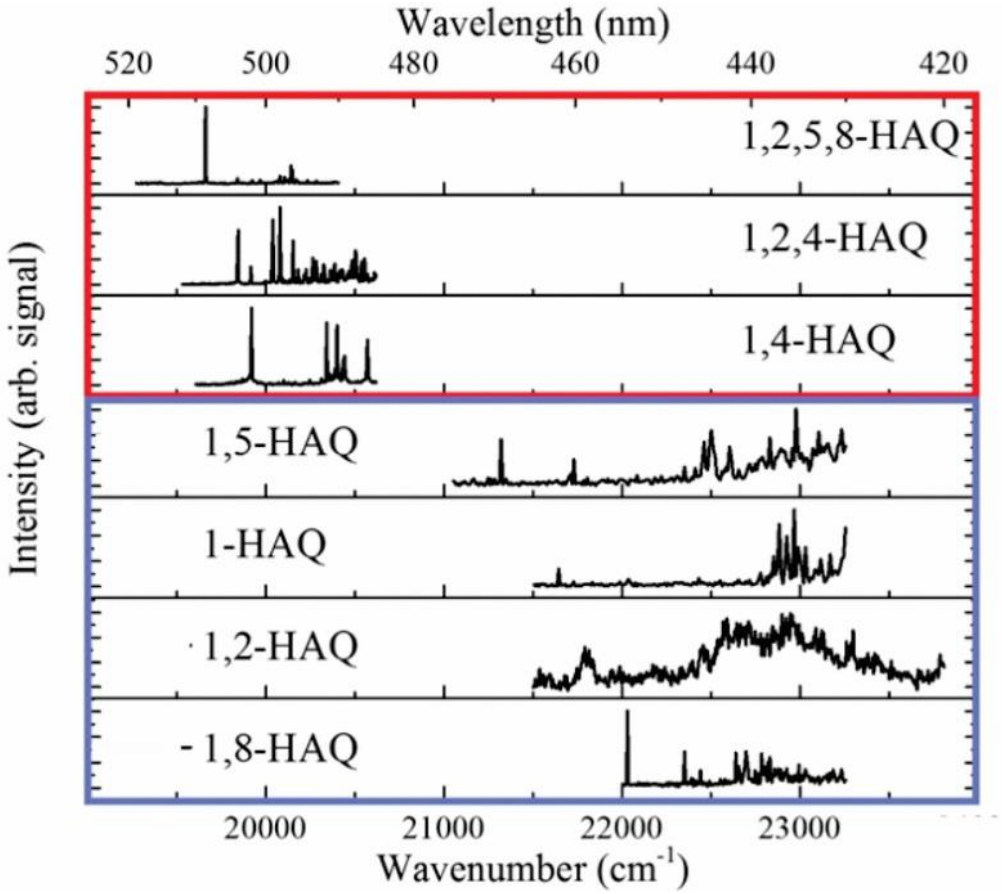


**Fig. 2.** Picosecond 2C-R2PI spectra of each HAQ in this study (OPG + 213 nm). Intensities have been normalized.

Fig. 2 presents the R2PI spectra of the HAQs from Fig. 1. The origins, corresponding to $S_{0\text{-}0}$ transitions, of molecules with a 1,4-motif are about 2000 $cm^{-1}$ lower in energy than those without the 1,4-motif. The origins of 1,2,5,8-HAQ (19,661 $cm^{-1}$), 1,2,4-HAQ (19,845 $cm^{-1}$), and 1,4-HAQ (19,920 $cm^{-1}$) all lie within 300 $cm^{-1}$ of each other, and each is characterized by sharp, laser linewidth limited, bands over a ~1000 $cm^{-1}$ range. In contrast to this, the HAQs

without the 1,4-motif are broader, and with origins – 1-HAQ (21,645 $cm^{-1}$), 1,2-HAQ (21,748 $cm^{-1}$), 1,5-HAQ (21,321 $cm^{-1}$), and 1,8-HAQ (22,031 $cm^{-1}$) – located over a larger energy spread, though still within ~700 $cm^{-1}$ of each other. The difference between these two groups of spectra, suggests that the excited state properties strongly depend on the presence or absence of the 1,4-OH structural motif.

**Pump-probe spectroscopy**

We performed picosecond pump-probe measurements for each HAQ from Fig. 1 on both the origin transition and on one additional higher energy transition, determined from the R2PI spectra. The measurement using the higher energy transition probed whether additional relaxation pathways become available at higher energies, which would likely be evidenced by a change in excited state lifetime. Fig. 3 shows the effect of structure on excited state lifetime. The molecules with the 1,4-OH motif, shown at the top in Fig. 3a in a red box, have nanosecond lifetimes at their lowest energy transitions. In contrast, those molecules without the 1,4-OH motif, shown at the bottom of Fig. 3a in a blue box, have sub-nanosecond lifetimes.

Coincidently, the primary madder chromophores (1,2,4-HAQ and 1,2-HAQ) have the longest and the shortest excited state lifetimes, respectively, of all molecules measured. Fig. 3b shows the pump-probe traces of these two end-members (picosecond pump-probe data for the other molecules are shown in Fig. S1, Supplemental Information). Each of these traces can be adequately fit using a single exponential, providing the excited state lifetime of each molecule. When probed at the origin, 1,2,4-HAQ (purpurin) has an excited state lifetime of 5.4 ns, while 1,2-HAQ (alizarin) has an excited state lifetime of only 120 ps. Others of the HAQ series have lifetimes intermediate between these two: 1-HAQ has a measured lifetime

of 290 ps while 1,4-HAQ has a measured lifetime of 1.7 ns, for example. In general, excitation at higher energies shortens the lifetime, as shown in Fig. 3a (black bars). 1,4-HAQ provides an exception to this trend, with a slight increase in excited state lifetime when measured at a transition +655 $cm^{-1}$ from the origin (from 1.7 ns to 1.9 ns). This slight increase is likely an artifact due to the short observation period relative to the excitation lifetime. For completeness, we also carried out nanosecond pump-probe measurements on the two endmembers (1,2,4-HAQ and 1,2-HAQ, data shown in Fig. S2). These measurements show no component at longer time scale than those found in the ps measurements.

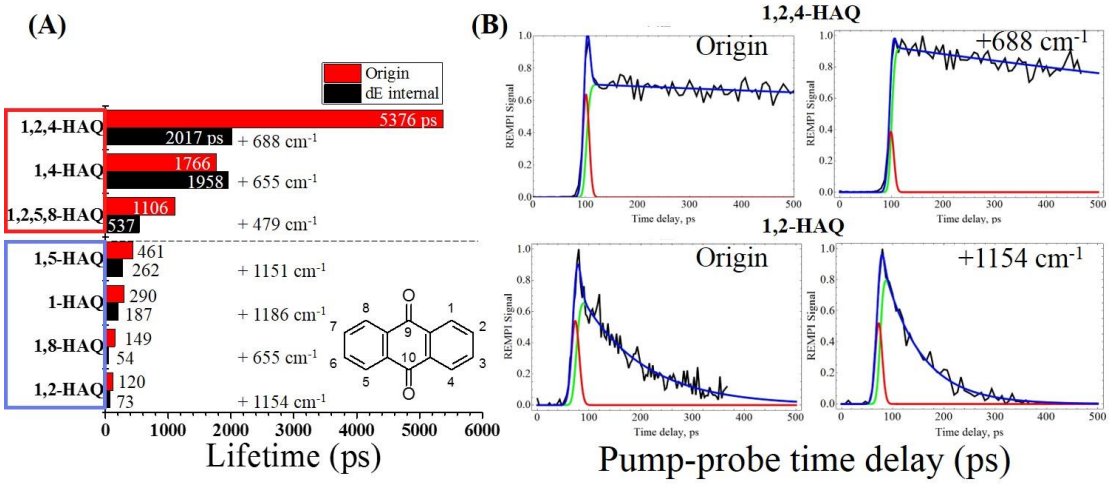


**Fig. 3. Results of picosecond pump-probe spectroscopy.** (A) Pump-probe lifetime as measured at the origin transition (red bars) and at excess energy (black bars), arranged in order of decreasing measured lifetimes. The excess energy transition used is noted next to the black bars. (B) Pump-probe traces of the molecules with the longest and shortest measured excited state lifetime, 1,2,4-HAQ and 1,2-HAQ respectively, plotted over 500 ps. The pump-probe data are fit to a curve (blue trace) which is the sum of a single exponential decay (green trace)

convolved with a Gaussian component (red trace) representative of our instrument response function (IRF).

**Intramolecular Hydrogen Bonding Characterization and Structural Confirmation**

In order to understand the hydrogen bonding environment of the isomer of species in the molecular beam with and without the 1,4-OH motif, we performed IR hole burning. IR-UV results in mode II indicate that for 1,2,4-HAQ and 1,4-HAQ the R2PI results are from a single conformation (see Supplemental Information Fig. S3).

We also performed hole burning in Mode 1 on 1,2,4-HAQ, 1,4-HAQ, and 1,8-HAQ while probing the origin of each, as shown in Fig. 4. In all three spectra the peak at ~3,100 $cm^{-1}$ represents stretching modes associated with the -OH hydrogen bound to a carbonyl group. In the case of 1,8-HAQ this peak is broadened by the competitive sharing of the carbonyl with intramolecular hydrogen bonds 180° about the oxygen atom (9-position). In the case of 1,2,4-HAQ the peak at 3570 $cm^{-1}$ results from the in-plane hydroxyl (2-position) which is hydrogen bound to the neighboring hydroxyl (1-position). The 470 $cm^{-1}$ separation is a direct measurement of different hydrogen bond environments: between carbonyl and hydroxy intramolecular bonded -OH stretches.

Fig. S4 in supplemental information also shows calculated LE spectra convoluted with a lorentzian linewidth of 3 $cm^{-1}$. These calculations reproduce the experimental patterns but not the exact frequencies, reflecting the fact that these are unscaled harmonic calculations. Future work with anharmonic calculations at a higher level may provide further details on structures.

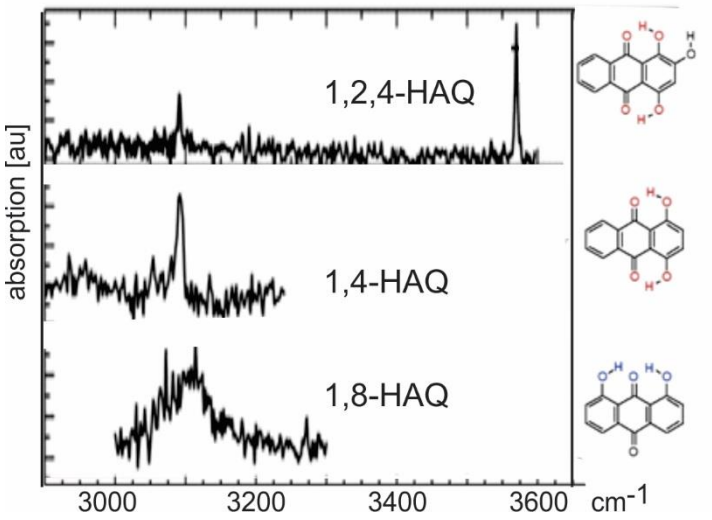


**Fig. 4. IR hole burning spectra. Spectra were taken in mode I of 1,2,4-HAQ, 1,4-HAQ, and 1,8-HAQ probed at their origin R2PI transition.**

## Theoretical calculations: 1-HAQ and 1,4-HAQ

To model computationally the difference in excited state dynamics in the two structural motifs, with and without the 1,4 substitution, we performed detailed calculations on the most basic representatives of the two structural families, namely 1-HAQ and 1,4-HAQ.

### *1-HAQ: ground and excited state*

Fig. 5 shows the calculated energetic landscapes of 1-HAQ. The ground-state global minimum of the keto form (I in Fig 5, hereafter referred to as K(I)) with the proton attached to the $O_1$ oxygen atom, is planar and stabilized by a single intramolecular hydrogen bond between two oxygen atoms as proton acceptor: $O_1$-H…$O_9$. The proton transferred form (enol form, II in Fig. 5, hereafter referred to as E(II)) with the proton attached to the $O_9$ oxygen atom is not stable in the $S_0$ state, and its geometry optimization transfers the proton back to the $O_1$ oxygen atom to reform the global minimum, form K(I). Possible rotation of the $O_1$H

group could generate the second lowest $S_0$-state minimum, the keto rotamer (III in Fig. 5) structure. However, the $O_1H$ rotation breaks the intramolecular hydrogen bond in the 1-HAQ structure, which destabilizes the rotated form compared to the global minimum K(I) by 0.52 eV (50 kJ/mol). Furthermore, the rotamer (III) minimum is separated from the global minimum by a $S_0$-state energy barrier of 0.16 eV (15kJ/mol). The fourth form, IV with the proton attached to the $O_9$ atom, has much higher energy and can be excluded from this study. This energetic profile indicates that the 1-HAQ molecule should exist in the K(I) form in the ground state.

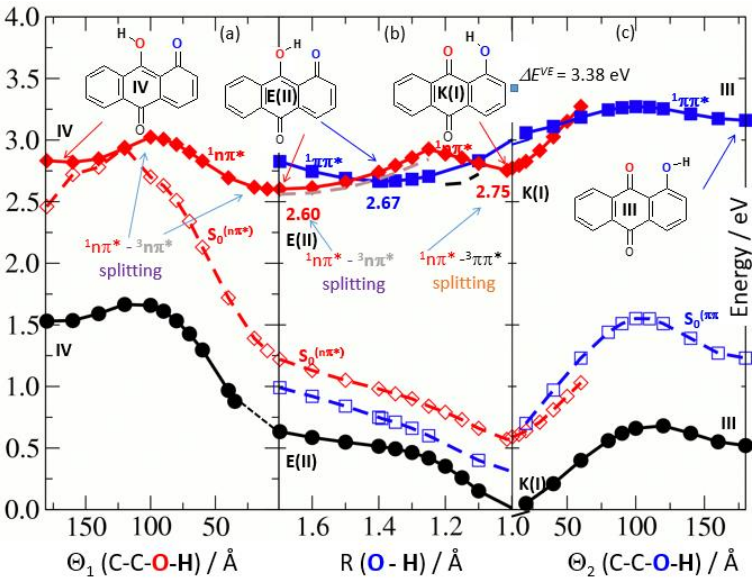


**Fig. 5. Potential-energy energy profiles of 1-HAQ.** Profiles shown are of the $S_0$ state (black circles), the $S_1(\pi\pi^*)$ state (blue squares) and the $S_1(n\pi^*)$ state (red diamonds) of the 1-HAQ molecule as a function of the torsional reaction path (a, c) and the hydrogen-transfer reaction path (b). Full lines (full symbols): energy profiles of reaction paths determined in the same electronic state. Dashed lines (empty symbols) represent ground-state energy calculated for the geometry optimized in the given excited state npi*(red) or pipi* (blue).

When 1-HAQ is irradiated, the ground-state K(I) form is photo-excited to the lowest ππ* excited state, $S_2(\pi\pi^*)$ with vertical energy $\Delta E^{VE}$ =3.38 eV at the $S_0$-state minimum geometry. At this optimized ground-state geometry of K(I), $S_1$ is a dark nπ* state below the $S_2(\pi\pi^*)$. The lowest ππ* excited state does not have a stable minimum in the K(I) form. Therefore, as long as the system remains in the excited ππ* state, the proton will transfer between the two oxygen atoms (from $O_1$ toward $O_9$) along a barrierless path to form the proton-transferred ππ* excited-state form, E(II), as indicated by the minimum of the blue curve (full squares) in the central panel of Fig. 5.

As depicted in Fig. 5, the nπ* and ππ* excited states intersect in the vicinity of the $S_1(\pi\pi^*)$ state minimum, E(II). Consequently, the nπ* state can be populated directly from the ππ* excited state. The nπ* state has two minima, at the K(I) and E(II) forms, and the adiabatic energies of both minima are lower than that of the $S_1(\pi\pi^*)$ E(II) minimum. Once in the non-fluorescent nπ* state the system seeks another decay channel. The $S_1$-$S_0$ energy gap lowers for the nπ* state to 1.38 eV for the E(II) excited-state form. As shown in Fig. 5, if the system is in nπ*- E(II) minimum, rotation of the $O_9H$ group may lead to further significant decrease of the $S_1$-$S_0$ energy gap (see red traces) until $S_1$ and $S_0$ meet at a C-C-$O_2$-H dihedral angle of about 100 $^{o}$. This pathway provides an additional channel for excited-state deactivation. However, the large barrier in the nπ* excited state may make this process less efficient.

The low-lying nπ* state may open another excited-state deactivation channel through intersystem crossing (ISC) between the singlet and triplet states if they are in close proximity. To check this possibility in 1-HAQ, we calculated the triplet state energies at the $^1$nπ* singlet excited state geometries along the excited–state minimum potential–energy (MPE) profile of

the $S_1(n\pi*)$ state, shown as a grey dashed line in central panel Fig. 5. Based on this curve, ISC seems to be a possible additional excited-state energy dissipation channel, since the triplet state energy profile is just less than 0.1 eV below the respective singlet $n\pi*$ state MPE profile, though there is as yet no experimental evidence for this process.

***1,4-HAQ: ground and excited state***

The addition of the OH group to position 4 of the 1-HAQ molecule (that is, the introduction of the 1,4-OH motif) results in significant changes, both structurally by forming a second intramolecular hydrogen bond, and photo-physically by changing the ordering of the excited states.

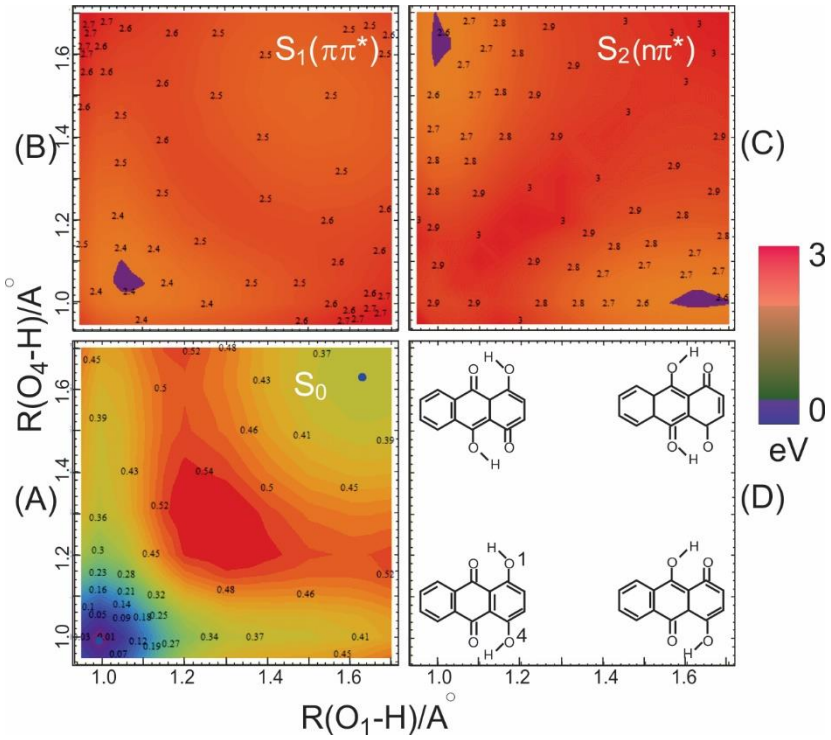


**Fig. 6. Potential energy surfaces (PES) of 1,4-HAQ.** (A) Minimum PES of the $S_0$ state, (B) the $S_1(\square\square\square)$ singlet excited state, (C) the $S_1(n\square\square)$ singlet excited state of the **1,4-HAQ**

molecule as a function of the hydrogen-transfer reaction path as a function of two coordinates: R($O_1$….H) and R($O_4$…H). (D) Schematic indication of the structures at the four combinations of minimum and maximum R values.

In contrast to 1-HAQ, 1,4-HAQ possesses two intramolecular hydrogen bonds: $O_1$-H…$O_9$ and $O_4$-H…$O_{10}$ which bridge the molecule on opposite sides and ensure planarity of the system. In addition to the global minimum energy KK(I) form with the protons attached to $O_1$ and $O_4$, there is an additional local minimum, 0.36 eV higher in energy, designated as EE(II) with the protons attached to $O_9$ and $O_{10}$. As shown in Fig. 6, the EE(II) minimum is separated from the KK(I) form by relatively small $S_0$-state energy-barrier of ~ +0.15 eV. The presence of this additional tautomeric minimum and the energy barrier (in contrast to the 1-HAQ system which lacks an energy barrier) might be explained by the fact that any proton transfer usually requires shortening of the interatomic distance between two proton accepting centers (here, two oxygen atoms). While one interatomic distance, e.g. $O_1$…$O_9$, contracts, the other, i.e. $O_4$…$O_{10}$, must simultaneously lengthen. This effect is not energetically favorable, creating the barrier. There are two other stable forms of the 1,4-HAQ molecule associated with respective rotation of the OH groups in analogy to the 1-HAQ molecule, but these are not apparent experimentally in the IR hole-burning results.

The vertical excitation energies, $\Delta E^{VE}$, to the lowest excited $\pi\pi^*$ state of the KK(I) and EE(II) forms of the 1,4-HAQ molecule are: 2.80 eV and 2.58 eV, respectively (for a complete tabulation of results, see Tables S1 and S2, Supplemental Information). Both values for the doubly substituted system are lower than the respective value of 3.38 eV for the singly OH-substituted molecule which is consistent with the experimental pattern of the origin shifts. This effect is consistent with $\pi$-electron donating character of the OH group(*25*) which should

result in stabilization of the ππ* excited state *vs* the nπ∗ state for a given structure. Indeed, the lowest nπ∗ states in the absorption ladder of both tautomeric forms of 1,4-HAQ are at least 0.5 eV above the lowest ππ* states.

The properties of the optimized excited state forms of the molecule are gathered in Table S1. Both KK(I) and EE(II), respectively, each have the same ground state and ππ∗ excited state geometries. Both excited-state forms are almost isoenergetic. Moreover, a barrier of only 0.15 eV separates the $S_1$ states of these two forms. At the same time, the nπ∗ state PES lies almost entirely above the fluorescent ππ∗ state. Such a situation greatly reduces the probability for nonradiative decay for the 1,4-HAQ in comparison to the 1-HAQ system.

**Discussion**

The experimental and computational results from this series of molecules demonstrate that the presence or absence of a hydroxyl substitution at the 4 position has profound effects on the spectroscopy and dynamics of substituted anthraquinones.

When interpreting spectral and pump-probe results it is important to keep in mind that multiple tautomeric forms are possible (as shown in Fig. 1). Generally, in jet-cooling conditions only the lowest energy forms exist and the mode II IR-UV data for 1,2,4-HAQ and 1,4-HAQ suggest those data to be exclusively from a single tautomer (though it is possible that signal arises from complimentary rotamers in Fig. 1). We assume the other compounds also to be exclusively or at least predominantly in the lowest energy tautomeric form but the possible existence of other tautomers in the beam cannot be definitively excluded.

With this limitation in mind, the experimental and computational evidence can be summarized as follows: (i) The origin transition for HAQs with the 1,4-motif is about 2000

cm-1 to the red of those without the 1,4-motif, as shown in Fig. 2.(ii) The excited state lifetime is approximately an order of magnitude shorter for those without the 1,4-motif, going from a few ns to a few hundred ps at the origin transition, as shown in Fig. 3. Relative to the 1-OH motif there is a 15× average longer lifetime for the molecular species with the 1,4-OH motif. (iii) In systems without the 1,4 motif (and therefore with short excited state lifetimes), proton transfer between the two oxygen atoms to form the proton-transferred $\pi\pi^*$ excited-state form is likely, while systems with the 1,4 motif more energetically favorable forms are likely to be present, limiting the probability for nonradiative decay pathways.

The photobleaching effects of *common madder* chromophores, 1,2,4-HAQ and 1,2-HAQ, was recently investigated by Tan et al. by counting emissive events in time (photo-blinking) of these dyes under inert ($N_2$) irradiant conditions on glass. They measured that alizarin is able to absorb and emit four times longer (and over many more events) than purpurin, which they argue to be due to a long lived excited state of purpurin which degrades through electron injection to the glass slide.(*11*) This decay pathway is consistent with the literature.(*19, 21, 26*) One cannot compare absolute lifetime values between gas phase and condensed phase states but the trend in the condensed phase correlates with the inherent lifetime trends presented here that 1,2-HAQ is ~ 45 times shorter lived at its vibrationless transition than 1,2,4-HAQ. The experimental data presented here seem to suggest that this pathway may be common to other substituted HAQs, with variations in the excited state lifetimes determined by the exact substitution arrangement.

Our theoretical investigation focused on the excited state potentials of 1-HAQ and 1,4-HAQ, since the experimental work showed that these motifs represent two distinct families of molecules. For 1-HAQ, the computations explain the experimentally observed short lifetimes

by an energetically downhill process from the initially populated ππ* state. Along the proton transfer coordinate, the nπ* state is crossed twice, leading to the minimum of K(II). Following this pathway, the energy gap to the ground state is 1.38 eV, allowing for nonradiative decay, although there may be additional involvement of an out of plane torsion, leading to a conical intersection. These dynamics are consistent with the relatively short lifetimes observed for the HAQs without a 1,4-motif. After reaching the ground state, it is a downhill path to transfer the proton back and complete the photocycle, recovering the K(I) tautomer.

The addition of the OH group to the 4 position of the HAQ skeleton results in several critical changes to ground and excited state profiles. First, in the 1,4-HAQ molecule there is a second $S_0$ state minimum, the EE (II) characterized by the two protons being transferred to the oxygens on carbons 9 and 10. Additionally, the shape of the ππ*-excited state in 1,4-HAQ is much shallower than in 1-HAQ and photoexcitation of the KK(I) form does not result in a barrierless proton transfer to the EE(II) form as in 1-HAQ. The most prominent effect is that the ππ* excited-state PES lies below the nπ* excited-state PES, an effect of electron-donating property of the OH-group, which tends to stabilize the ππ* excited state versus the nπ*state. This explains the red shift of 1,4 motif versus those molecules that lack it.[25,27] This effect also inhibits nonradiative decay from the excited $S_1$(ππ*) to $S_0$. The last effect of 4-OH substitution is related to the unique stabilization of the KK(ππ∗), lacking the proton transferred minimum of the ππ∗ excited state in 1-HAQ. The analogous initial ππ∗ state in 1-HAQ undergoes proton transfer in a barrierless manner. With a single ns timescale lifetime seen for the molecules with a 1,4-motif, it is expected that none of them undergo ESIPT, and instead relax from the initially populated ππ* state.

We investigated the possibility of longer-lived states such as triplets with a ns ionization source for 1,2-HAQ and 1,2,4-HAQ, but have not observed such states experimentally. However, Mohamed et al. reported formation of a long lived triplet state with high quantum yield in a study of 1,8-DHAQ in a series of nonpolar, polar aprotic, and polar protic solvents.[20] Further work in this area is therefore justified to clarify whether long lived triplets may form in some systems.

As seen by Flom and Barbara and explained by Nagaota et al., the 1-HAQ motif exhibits dual fluorescence due to ESIPT. As the main excited-state pathway, this explains the photostability of molecules lacking the 1,4-HAQ motif observed in works of art (by, e.g. alizarin). In contrast, molecules **with** the 1,4-HAQ motif lack dual fluorescence and the corresponding ESIPT properties. At the same time, molecules with the 1,4-HAQ motif are noted for their photodegradation in works of art (e.g. purpurin). We have corroborated these phenomena both experimentally and theoretically in the gas-phase, indicating that this is a fundamental characteristic of the anthraquinone molecules used to create lake dyes, and not due to other effects such as the interaction of the binding media or other pigments that may be present in a complex system. Molecules with the 1-HAQ motif have ~15x shorter excited state lifetime than molecules with the 1,4-HAQ motif, explaining the former's photostability. The energetically downhill process of ESIPT accounts for the shorter lifetime of the 1-HAQ motif. Meanwhile, the geometries resulting from ESIPT of the 1,4-motif are all higher in energy than the initially excited, non-proton transfer state, making PT highly unfavorable. Without this process available, the 1,4-motif has a much longer excited-state lifetime and worse photostability.

Taken with the body of work done on UV radiation on anthracene by Mallakin on the production of toxic species (i.e. reactive, typically $^1O_2$) through the stepwise formation and further irradiation of AQs and HAQs[28,29] and the work by Nagaoka et. al on the quenching of singlet oxygen ($^1O_2$) by ESIPT HAQs, a complex picture begins to form of the degradation of the madder colorants in cultural heritage materials. It may be possible that due to its longer lifetime, purpurin and other molecules with the 1,4-OH motif can transfer the energy of its electronic transition to a reactive species, involving either a mordant metal or formation of a reactive oxygen species which the PT excited structure found in e.g. alizarin can efficiently quench.

## Materials and Methods

### Experimental Design

Standards of seven HAQs were purchased from Sigma-Aldrich and used without further purification. Standards were directly applied to individual graphite sample bars as a thin solid layer and examined in isolation to ensure spectral purity for 2C-R2PI and pump-probe measurements.

The instrument has been previously described in detail and only a brief description of the experimental setup follows.[30,31] Samples are laser desorbed in vacuo directly in front of a pulsed molecular beam controlled by a piezo cantilever valve.[32] The desorption laser is a tightly focused Nd:YAG laser (1064 nm, ~ 1 mJ/pulse) and the piezo cantilever valve operates at a 45 μsec pulse duration with 8 bars backing argon gas. The desorbed sample is adiabatically cooled by collisions with the argon jet-expansion to between 10-20 K and the molecular beam is skimmed before being intersected by laser beams and photo-ionized by two-color resonant

two photon ionization (2C-R2PI). The subsequent ions are detected by a reflectron time of flight mass spectrometer (2 x $10^{-6}$ Torr analyzer pressure, mass resolution m/Δm=500).

The 2C-R2PI spectroscopic and picosecond (ps) pump-probe delay measurements are performed with an Ekspla PL2251 Nd:YAG laser system producing ~30 ps laser pulses. The 355 nm output pumps an Ekspla PG401 tunable optical parametric generator (OPG) (VIS output of 450-600 uJ/pulse, ~6 $cm^{-1}$ spectral linewidth). The sample is excited by the OPG and ionized by 213 nm, fifth harmonic of the Ekspla PL2251 laser, which is mechanically delayed up to 600 ps before colineation with the OPG beam. A variable electronic (SRS DG645) delay between OPG UV laser and an excimer laser (193 nm, 1.5-2 mJ/pulse) is used for pump-probe measurements in the nanosecond (ns) time delay range.

For IR-UV double resonant spectroscopy (i.e. IR hole-burning) a Laser Vision optical parametric oscillator/amplifier (OPO/OPA) (mid-IR output over the range 3,000-3,600 $cm^{-1}$ of ~3-5 mJ/pulse, 3 $cm^{-1}$ spectral linewidth) precedes the REMPI by 200 ns. This study utilized double resonant spectroscopy with two different pulse sequences: in mode I, the IR pump is scanned at a fixed UV probe wavelength, while in mode II, the UV is scanned with a fixed IR burn wavelength. In mode I, the UV laser wavelength is selected to correspond to a single vibronic transition, and the resulting 2C-R2PI signal depletes when the IR laser becomes resonant with the ground state population. The resulting ion-dip spectrum therefore represents the ground state IR spectrum of a single tautomer, selected by the UV probe wavelength. This IR spectrum can be compared with calculated IR frequencies to determine the specific tautomer of the selected vibronic transition. In mode II, the IR laser wavelength is selected to correspond to a tautomer-specific vibrational resonance, and spectra are collected both with

IR laser on and off. The difference spectrum identifies peaks in the UV spectrum that arise from the same tautomer.

**Calculations for IR-UV double resonant spectroscopy**

Calculations were performed with the Gaussian 09 program package.(*33*) Starting structures for hydroxy derivatized anthracene-9,10-dione (HAQ) structures, tautomer and rotamer isomers, were optimized using the B3LYP hybrid functional with CC-pVTZ basis set. Relative zero- point corrected energy (ZPE) values are used to predict the number of isomers in our molecular beam based on the rule of thumb that for a given species isomers up to 20 kJ/mol of the lowest energy structure are typically kinetically trapped laser desorption jet-expansion. Past work on the nucleobase adenine showed that only the lowest energy isomer was present, where the next lowest energy isomer was calculated to be at ~33 kJ/mol higher energy than the one observed.[34] Ground state minima were confirmed by the absence of imaginary frequencies and these geometries were later used to determine electronic transition state strengths for S1-4 by way of TD-DFT with the B3LYP hybrid functional with CC-pVTZ basis set. The simulated IR spectra arise from frequencies with harmonic intensities using a Lorentzian shape and FWHM of 3 $cm^{-1}$ and are presented without a spectral shift.

**Calculations for construction of energy profiles**

The ground-state minima forms of the 1-HAQ and 1,4-DHAQ were optimized by means of the MP2 method using the cc-pVDZ(*36*) correlation-consistent atomic basis set. The excited-state geometries were optimized with the use of the same basis set while using the CC2(*37, 38*) method as implemented in TURBOMOLE software package.[35,39] In the calculation of the vertical excitation energies, $\Delta E^{VE}$, mimicking the absorption spectra,

performed on top of the MP2/cc-pVDZ-optimized $S_0$-state geometries, the CC2 method was used to evaluate the response properties.[37,38]

To elucidate the photophysical mechanism on the molecular level the important driving coordinates were appropriately chosen for each system so that the ground– and the excited–state minimum potential–energy (MPE) profiles or surfaces could be constructed to estimate the ground– and excited–state energy barriers determining the photophysics of the both molecules. The 1-HAQ molecule is bound by a single hydrogen bond. In such case one coordinate – the $R_1(O_1H)$ distance – is needed to be chosen as a driving coordinate to illustrate the photophysical mechanism of the photo–tautomerization process. The MPE profile for 1-HAQ is constructed in a way that for fixed given value of the $R_1(O_1H)$ distance, all the remaining nuclear degrees of freedom are optimized; once in the ground state and twice in the two excited states: $S_1(\pi\pi^*)$ and $S_1(n\pi^*)$.

The 1,4-DHAQ system has an additional intramolecular hydrogen bond binding the molecule and more tautomeric forms are possible to be formed upon photoexcitation. A convenient method for illustrating the tautomerization process in such molecule is to construct the MPE surface spanning the two driving reaction coordinates describing the two intramolecular hydrogen bonds by the $R_2(O_2H)$ and $R_3(O_4H)$ distances. In that case both the $R_2$ and $R_3$ coordinates are being frozen for given values, while the rest of the parameters are being optimized in the constructed MPE surface, separately for the ground ($S_0$) and the two excited states: $S_1(\pi\pi^*)$ and $S_1(n\pi^*)$ with the $C_s$ symmetry constrain.

***Supplementary Materials***

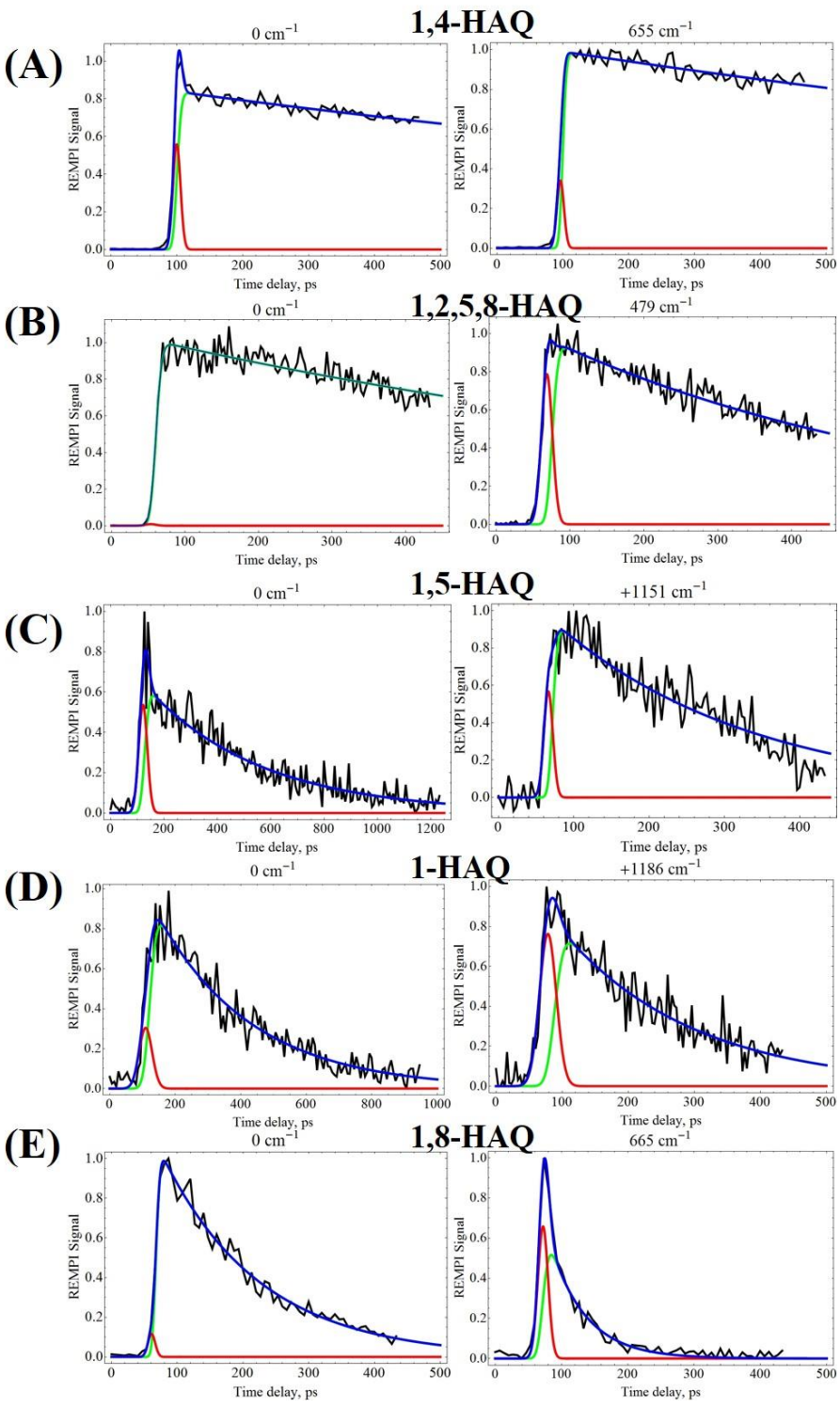
(A)
1,4-HAQ
0 cm−1
655 cm−1
(B)
1,2,5,8-HAQ
0 cm−1
479 cm−1
(C)
1,5-HAQ
0 cm−1
+1151 cm−1
(D)
1-HAQ
0 cm−1
+1186 cm−1
(E)
1,8-HAQ
0 cm−1
665 cm−1
REMPI Signal
Time delay, ps

**Figure. S1.** Picosecond pump-probe spectra. (A) 1,4-HAQ, (B) 1,2,5,8-HAQ, (C) 1,5-HAQ, (D) 1-HAQ, and (E) 1,8-HAQ at vibrationless (left column) and excess probe lengths (right column). The pump-probe data are fit to a curve (blue) which is the sum of a single exponential decay convolved with a Gaussian component (red) representative of our instrument response function (IRF) the IRF itself (green).

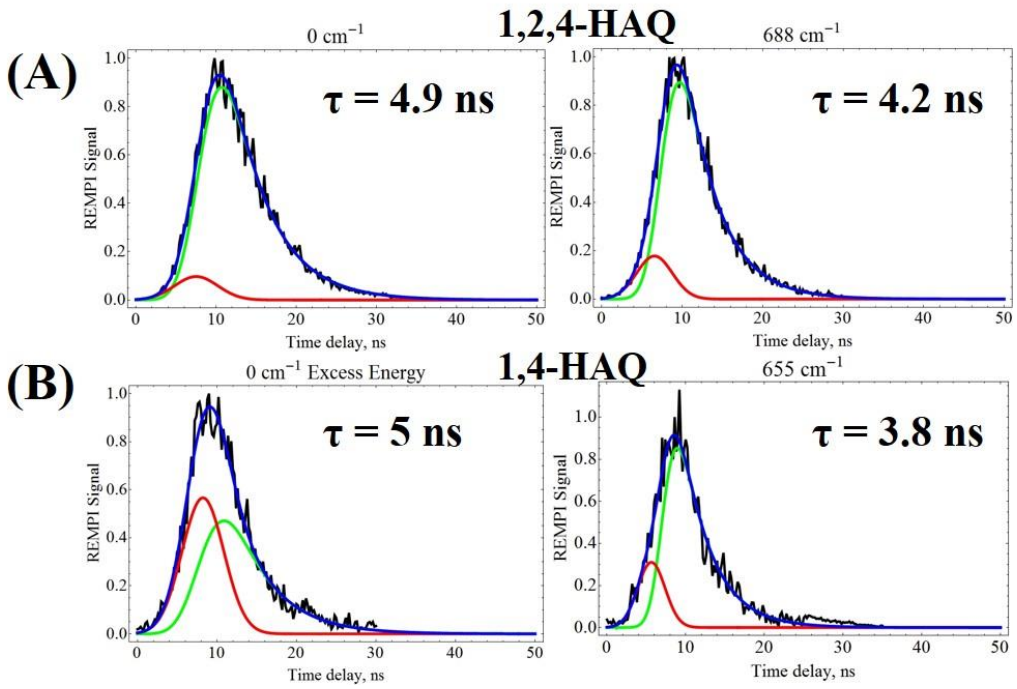


**Figure. S2.** Nanosecond pump-probe spectra. (A) 1,2,4-HAQ at vibrationless and excess probe lengths and for (B) 1,4-HAQ at vibrationless and excess probe lengths. The lifetime values here agree with those presented in Fig. 3for pump-probe measurement within the time jitter (± 3 ns) of the 193 nm ns ionization source. The pump-probe data are fit to a curve (blue) which is the sum of a single exponential decay convolved with a Gaussian component (red) representative of our instrument response function (IRF) the IRF itself (green).

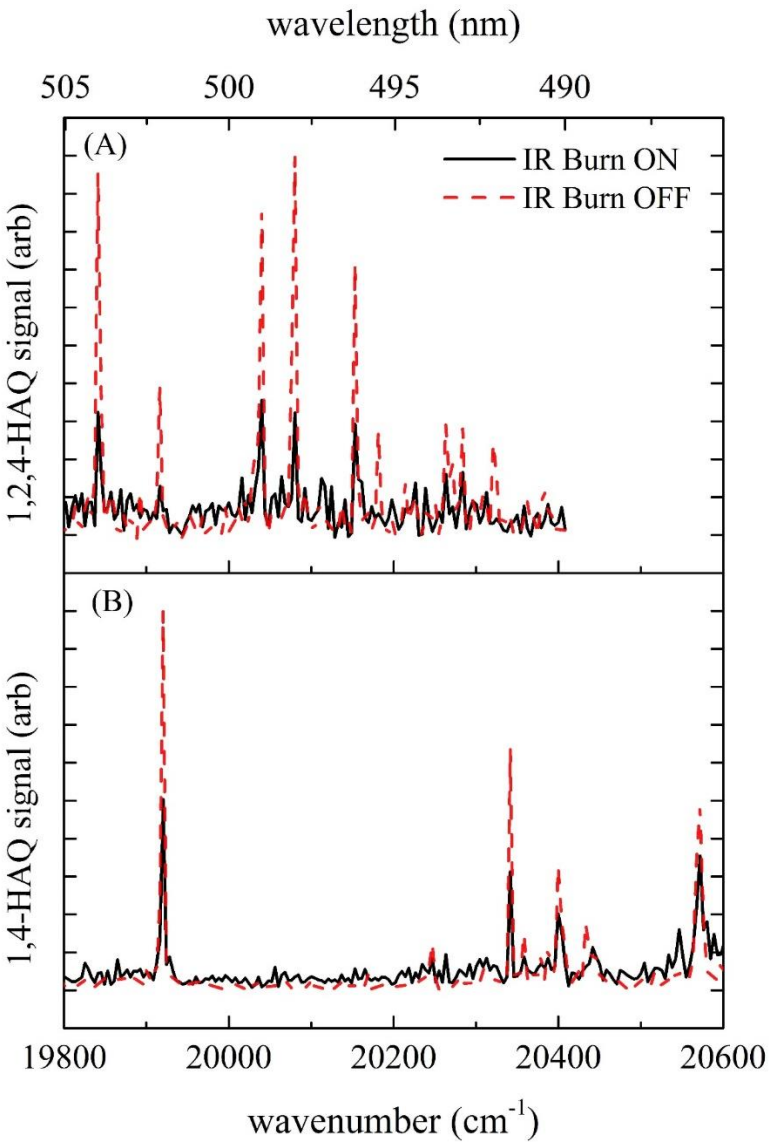


**Figure. S3.** IR hole burning spectra in mode II with the burn laser set to 3090 $cm^{-1}$. (A) All 1,2,4-HAQ vibronic transitions share resonance at IR burn wavelength, as do all (B) 1,4-HAQ vibronic transitions, suggesting a single tautomer in each R2PI spectrum.

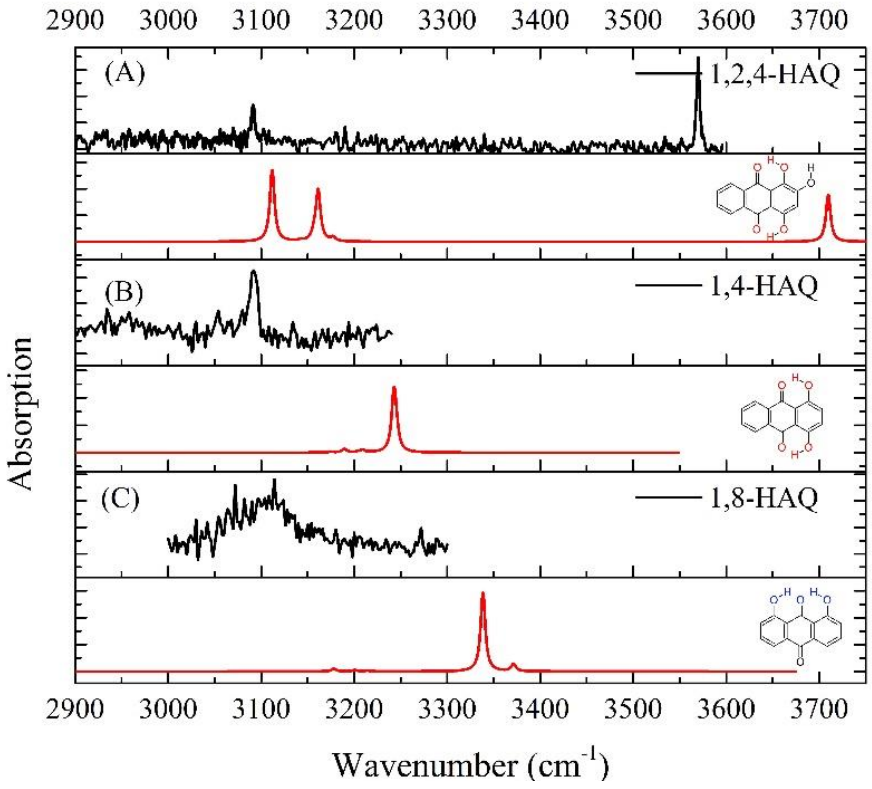


**Figure. S4.** IR hole burning spectra (in black) taken in mode I of (A) 1,2,4-HAQ, (B) 1,4-HAQ, and (C) 1,8-HAQ probed at their lowest energy R2PI transition. The ground state predicted frequencies for the given LE structure are plotted below each hole burn spectrum (in red). Harmonic analysis is shown unshifted.

**Table S1: Calculated properties of 1-HAQ and 1,4-HAQ.** Vertical excitation energies, $\Delta E^{VE}$ (in eV) for the stable minima of the **1-HAQ** and **1,4-HAQ** molecules calculated at the CC2/cc-pVDZ theory level at the geometries optimized with the MP2/cc-pVDZ method. The ground-state properties are marked Italic.

| **1-HAQ** | | | |
|---|---|---|---|
| **$S_n$ / Tautomer** | **$\Delta E^{VE}$ / eV** | ***f*** | **$\mu$ / D** |
| **form K (I)** | | | |
| $S_0$ | *0.0* | | *1.4* |
| $S_1(n\pi^*)$ | 3.21 | 0.000 | 2.8 |
| **$S_2(\pi\pi^*)$** | **3.38** | **0.145** | 4.4 |
| $S_3(n\pi^*)$ | 3.62 | 0.000 | 2.6 |
| $S_4(\pi\pi^*)$ | 4.28 | 0.029 | 4.9 |
| $S_5(\pi\pi^*)$ | 4.31 | 0.012 | 1.3 |
| $S_6(n\pi^*)$ | 4.97 | 0.000 | 4.0 |
| **form K_rot (III)** | | | |
| $S_0$ | *0.52* | | *1.8* |
| $S_1(n\pi^*)$ | 3.10 | 0.000 | 3.6 |
| $S_2(n\pi^*)$ | 3.43 | 0.000 | 2.2 |
| **$S_3(\pi\pi^*)$** | **3.79** | **0.110** | 7.2 |

| | | | |
|---|---|---|---|
| $S_4(\pi\pi^*)$ | 4.34 | 0.035 | 3.2 |
| $S_5(\pi\pi^*)$ | 4.55 | 0.014 | 0.7 |
| $S_6(n\pi^*)$ | 4.74 | 0.000 | 6.3 |
| **1,4-HAQ** | | | |
| **$S_n$ / Tautomer** | ***$\Delta E^{VE}$* / eV** | ***f*** | ***$\mu$* / D** |
| **form KK (I)** | | | |
| $S_0$ | *0.0* | | *2.2* |
| $S_1(\pi\pi^*)$ | 2.80 (a1) | 0.209 | 2.5 |
| $S_2(n\pi^*)$ | 3.32 (b2) | 0.000 | 1.9 |
| $S_3(n\pi^*)$ | 3.65 (a2) | 0.000 | 2.1 |
| $S_4(\pi\pi^*)$ | 4.14 (b1) | 0.000 | 0.4 |
| $S_5(\pi\pi^*)$ | 4.29 (a1) | 0.032 | 7.1 |
| $S_6(\pi\pi^*)$ | 4.43 (b1) | 0.006 | 4.0 |
| **form EE (II)** | | | |
| $S_0$ | *0.36* | | *1.1* |

| | | | |
|---|---|---|---|
| $S_1(\pi\pi^*)$ | 2.58 (a1) | 0.246 | 4.8 |
| $S_2(n\pi^*)$ | 3.19 (b2) | 0.000 | 0.6 |
| $S_3(n\pi^*)$ | 3.46 (a2) | 0.000 | 0.4 |
| $S_4(\pi\pi^*)$ | 3.86 (b1) | 0.007 | 0.9 |
| $S_5(\pi\pi^*)$ | 4.16 (b1) | 0.051 | 5.2 |
| $S_6(n\pi^*)$ | 4.34 (a1) | 0.002 | 4.2 |
| **form KK_rot (I)** | | | |
| $S_0$ | *0.55* | | *0.9* |
| $S_1(n\pi^*)$ | 3.03 | 0.188 | 5.7 |
| $S_2(\pi\pi^*)$ | 3.03 | 0.000 | 4.2 |
| $S_3(n\pi^*)$ | 3.60 | 0.000 | 2.6 |
| $S_4(\pi\pi^*)$ | 4.29 | 0.026 | 4.1 |
| $S_5(\pi\pi^*)$ | 4.38 | 0.020 | 0.9 |
| $S_6(n\pi^*)$ | 4.70 | 0.000 | 6.8 |

**Table S2: Emission properties of 1-HAQ**. Adiabatic energy, ($E^a$ in *eV*, bold), fluorescence energy, *($E_{fl}$*, given in parenthesis), excited-state dipole moment ($\mu_e$ in *D*) and

oscillator strength (*f*) of the given excited-state form optimized with the CC2/cc-pVDZ method.

| **1-HAQ** | | | | |
|---|---|---|---|---|
| **state/ tautomer** | ***E*$^{a}$*(S$_n$)*** (E$_{fl}$) | $\mu_e$ /*D* | *f* | |
| **form K(I)** | | | | |
| **S$_0$** | **0.00** | | | |
| **S$_1$ $^{\pi\pi*}$** | **-** | **-** | **-** | |
| **S$_1$$^{n\pi^*}$** | **2.75** (2.18) | $\mu_e$ = 4.2 D | **0.00** | |
| **form E(II)** | | | | |
| **S$_0$** | **-** | | | |
| **S$_1$ $^{\pi\pi*}$** | **2.67** (1.92) | $\mu_e$ = 1.2 D | **0.200** | |
| **S$_1$$^{n\pi^*}$** | **2.60** (1.38) | $\mu_e$ = 5.4 D | **0.000** | |

**Table S4: Emission properties of 14-HAQ**. Adiabatic energy, (*E*$^{a}$ in *eV*, bold), fluorescence energy, (*E*$_{fl}$, given in parenthesis), excited-state dipole moment ($\mu_e$ in *D*) and oscillator strength (*f*) of the given excited-state form optimized with the CC2/cc-pVDZ method.

| **1,4-HAQ** | | | | |
|---|---|---|---|---|
| **state/ tautomer** | ***Sn*** (Efl) | $\mu_e/D$ | *f* | |
| **form KK(I)** | | | | |
| **S0** | ***0.00*** | | | |
| **S1 (ππ*)** | **2.39** (2.13) | 0.1 D | 0.221 | |
| **S1(nπ*)** | **2.95** (2.42) | 3.1 D | **0.000** | |
| **form EE(II)** | | | | |
| **S0** | ***0.36*** | | | |
| **S1 (ππ*)** | **2.50** (2.01) | 2.6 D | **0.225** | |
| **S1(nπ*)** | **3.10** (2.57) | 2.0 D | **0.000** | |
| **form EK ~ KE** | | | | |
| **S0** | **-** | | | |
| **S1 (ππ*)** | - | - | - | |
| **S1(nπ*)** | **2.66** (1.70) | 3.6 D | **0.000** | |

## III. Excited-State Dynamics of Alternative Nucleobases

On a prebiotic Earth, it is predicted that harsh UV radiation from the sun acted as a selective pressure on the building blocks of life, the canonical nucleobases and their substituted analogues, influencing the eventual structure of RNA and then DNA. As such, the excited-state lifetimes of all the canonical nucleobases have been found to be ultrafast, corroborating the relevance of UV-radiation on nucleobases. Isocytosine has been studied as a strong candidate as an alternative pyrimidine version of guanine. Through excited-state measurements, it was found that the alternative base shares similar dynamics to guanine, and differences in their relaxation mechanisms were reported further.

### I. Excited State Dynamics of Isocytosine; A Hybrid Case of Canonical Nucleobase Photodynamics

Jacob A. Berenbeim, Samuel Boldissar, Faady M. Siouri, Gregory Gate, Michael R. Haggmark, Briana Aboulache, Trevor Cohen, and Mattanjah S. de Vries*

*Department of Chemistry and Biochemistry, University of California Santa Barabara, CA 93106-9510*

**Abstract**

We present resonant two-photon ionization (R2PI) spectra of isocytosine (isoC) and pump-probe results on two of its tautomers. We compare the excited state dynamics with the Watson Crick (WC) cytosine (C) and guanine (G) tautomeric forms. These results suggest that the excited state dynamics of WC G may primarily depend on the heterocyclic substructure of the pyrimidine moiety, which is chemically identical to isoC. For WC isoC we find a single excited state decay with a rate of ~ $10^{10}$ $s^{-1}$ while the enol form has multiple decay rates, the fastest of which is 7 times slower than for WC isoC. The excited state dynamics of isoC exhibits striking similarities with that of G, more so than with the photo-dynamics of C.

Without a fossil record of the prebiotic chemical world we are left to conjecture to understand the road map that led to RNA and DNA. One of the factors that may have played a role in the prebiotic chemistry on an early earth is the photochemistry that could have been important before modern enzymatic repair and before the formation of the ozone layer.[1-6] Nucleobases, when absorbing ultraviolet (UV) radiation, tend to eliminate the resulting electronic excitation by internal conversion (IC) in picoseconds (ps) or less.[4, 7-9] The availability of this rapid "safe" de-excitation pathway turns out to depend exquisitely on molecular structure. DNA and RNA bases are generally short lived in the excited state, and thus UV protected, while many closely related compounds are long lived and thus more prone to UV damage. This structure dependence suggests a mechanism for the chemical selection of the building blocks of life, implying that photochemical properties may be molecular fossils of the earliest stages of prebiotic chemistry.

It is therefore of great interest to study the photochemical properties of possible alternative bases in comparison to the canonical bases. Especially intriguing are structures that can form alternate base pairs with the same Watson Crick (WC) motif as the canonical ones, such as the triple hydrogen bonded Guanine/Cytosine (G/C) pair.[10-13] The alternative bases isocytosine (isoC) and isoguanine (isoG) were predicted in 1962 as a plausible third WC base pair.[14] As pointed out by Saladino et al., isoC can form WC base pairs with cytosine (C) and isoguanine or a reversed WC base pair with guanine.[15] Here we focus on isoC, which is not only an isomer of C but also an analogue of guanine (G), see Figure 1. Theoretical and experimental study has established the thermodynamic stability of the isoC/isoG base pair which nominally has greater free energy than G/C as well as of other possible base pair combinations with isoC.[16-17] This has piqued interest in the prebiotic prevalence of these

unnatural pairs in addition to their role in synthetic research and medical applications.[18-19] Here we aim to understand the photostability of isoC.

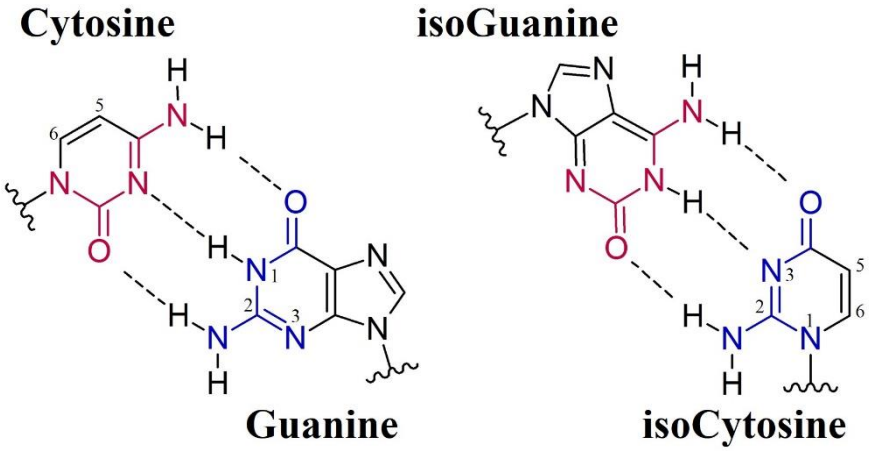


**Figure 2: Structures of G/C and isoG/isoC arranged to emphasize heterocyclic substructure similarities, emphasized in red and blue.**

We have arranged the bases within Figure 1 to emphasize the functional rearrangement from the standard base to its iso- analog about the pyrimidine heterocyclic centers. Doing so likens isoC to the core moiety of G. The difference between G and isoC is the five membered ring in G (not present in isoC) which would have consequences for formation of a macromolecular structure. In this work, we find that the excited state dynamics of isoC exhibits striking similarities with that of G and more so than with the photo-dynamics of C.

IsoC has previously been identified in the gas phase[20] and its photo dynamics have been studied theoretically[21-22] and in the condensed phase[23-25] but no excited state lifetime has been experimentally determined of isolated isoC in individual tautomeric forms. The two lowest energy forms are enol and keto which can isomerize via an excited state intramolecular proton

transfer. This isomerization after UV excitation has been observed in solution[23] by time dependent absorption spectroscopy and in a rare gas matrix by changes in the IR absorption.[24-25] Chart 1 outlines the lowest energy tautomers in the gas phase. KA2 corresponds to the WC structure in the pairing with isoG in Figure 1. KA1 can also form similar triple hydrogen bonded structures with other tautomeric forms of G, such as the enol form.

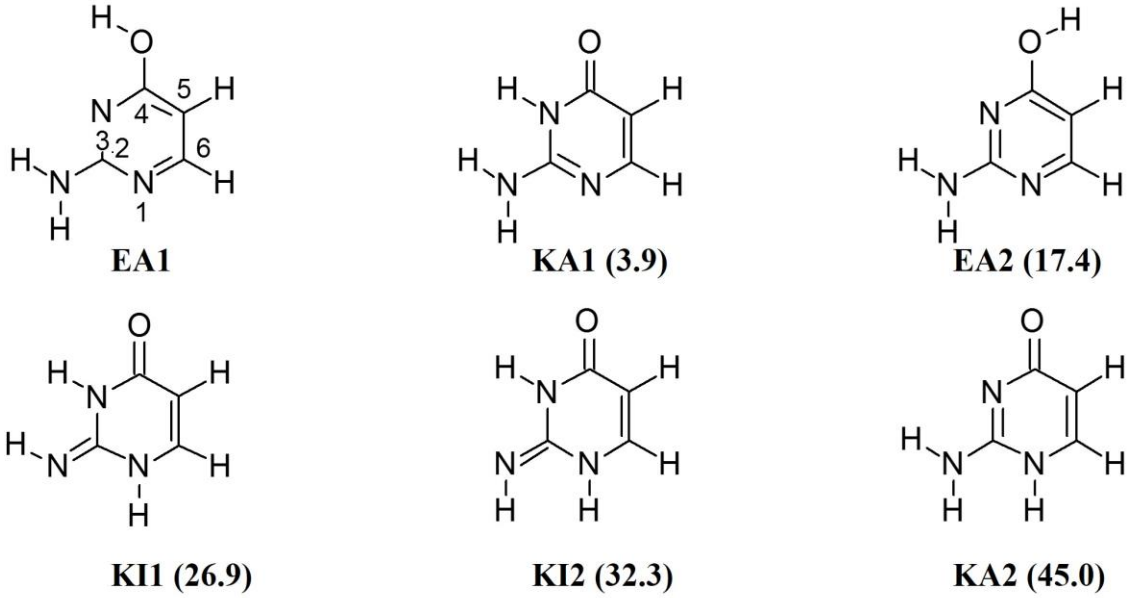


**Chart 1:** Lowest ground state energy structures (ΔE < 50 kJ/mol). Heterocyclic atoms are numbered for EA1 but the convention is the same for all others. Arranged in order of relative energy given in parenthesis (kJ/mol). Zero point corrected energies were calculated by DFT analysis with the B3LYP hybrid functional and with a cc-pVTZ basis set.

Recent work by Szabla et. al used state-of-the-art surface-hopping adiabatic molecular dynamic simulations to predict the excited states lifetime of isoC to be the following: $\tau_{EA1}$=533 fs and $\tau_{KA1}$=182 fs.[21] These lifetimes are from populating a continuum of mixed character electronic states S1-S6 at the 5.5 ± 0.2 eV spectral domain which proceed to relax

through S1 IC. Three dominant conical intersection (CI) geometries are established in their work for the modeled EA1 and KA1 starting structures, whereby pyramidalization of the planar Franck Condon (FC), i.e. excitation geometry, structure at the C2 position accounts for $\Phi_{EA1}$=0.60 and $\Phi_{KA1}$=0.93 non-radiative relaxation yields, while deformation about the $C_5$=$C_6$ bond accounts for a CI of negligible yield. Hu et al. also studied the KA1 form computationally, comparing different levels of theory. They assumed excitation at energies closer to the vibrationless level and identified three CIs, all leading to IC to the ground state, one involving the C=O stretching vibration and two involving out-of-plane structures of the $NH_2$ group. They found the preferred pathway to depend on the computational method, as did the IC rate, leading to excited state lifetimes ranging from 100 fs to 1 ps.[26] Surprisingly, both computational studies are contrary to the bulk of theoretical work done on pyrimidine relaxation dynamics, where the $CI_{C5=C6}$ is understood to be a major pathway towards nonradiative deactivation by twisting of the H-$C_5$=$C_6$-H torsional angle to near ethylene geometry.[27-29] Trachsel et al. most recently showed the importance of this particular bond deformation when they measured excited state lifetimes of 5,6-trimethylenecytosine, a sterically constrained C analogue, in the gas phase.[30] This modified version yielded lifetimes attributed to IC six times greater than that of C, likely due to the absence of a $CI_{C5=C6}$.

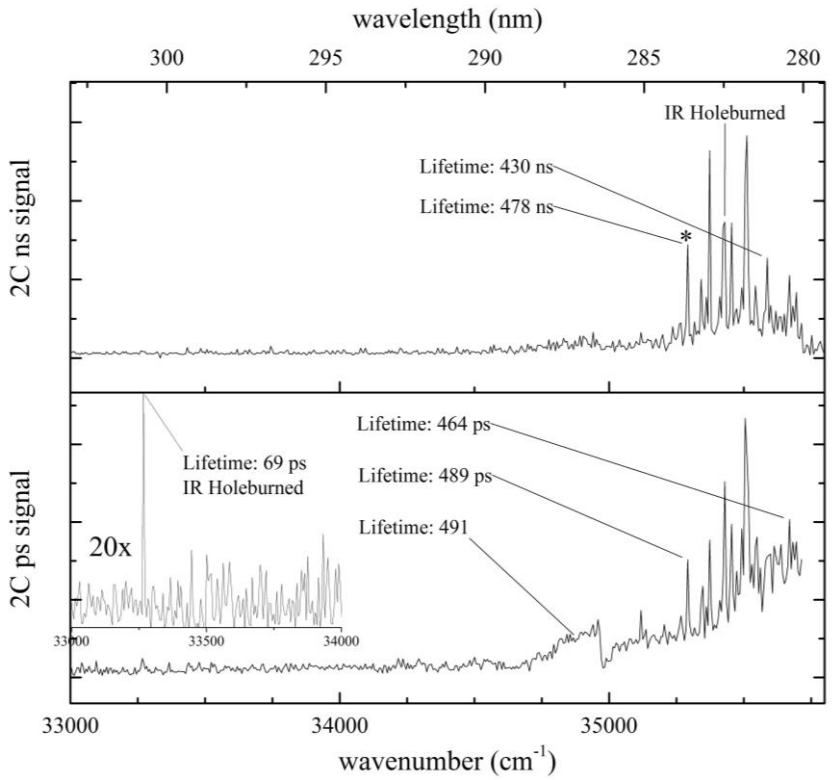


**Figure 3:** 2C R2PI spectra for isocytosine (a) ns excitation with 193 nm ionization and (b) ps excitation with 213 nm ionization (5th Nd:YAG harmonic). Lifetimes are pump-probe data. See text for details.

Figure 2 shows Two-Color (2C) resonant two-photon ionization (R2PI) spectra of isocytosine with nanosecond (ns) and ps pulse sources. The ns spectrum (Figure 2a) has a well-defined origin transition at 35,292 $cm^{-1}$ (starred *) followed by a series of discrete peaks atop an elevated baseline over a range of 500 $cm^{-1}$. This elevated baseline extends to the red but is relatively low in intensity and devoid of features. The ps trace (Figure 2b) exhibits the same defined vibronic transitions seen in the ns spectrum but presents another unique feature at 33,266 $cm^{-1}$. Here, the elevated baseline features to the red of the starred origin are by contrast to the ns spectrum more intense. While this signal could result from other tautomers, we suspect that this feature is due to hot bands from the low frequency breathing vibrational

modes which are more efficiently excited with the 6 $cm^{-1}$ spectral linewidth of ps laser and artificially intensified by elevated laser power in that region. The sharp feature at 35,000 $cm^{-1}$ is a laser power artifact and highlights the non-resonant nature of the absorption in this range. Furthermore, we could not obtain IR-UV double resonant signal from this part of the spectrum, which is also consistent with hot bands. We simultaneously recorded wavelength and mass spectra, shown as a two-dimensional plot in supplemental information (S.1) to verify that there is no contribution to the isoC mass channel from potential higher order clusters, including checking the M+1 mass channel.

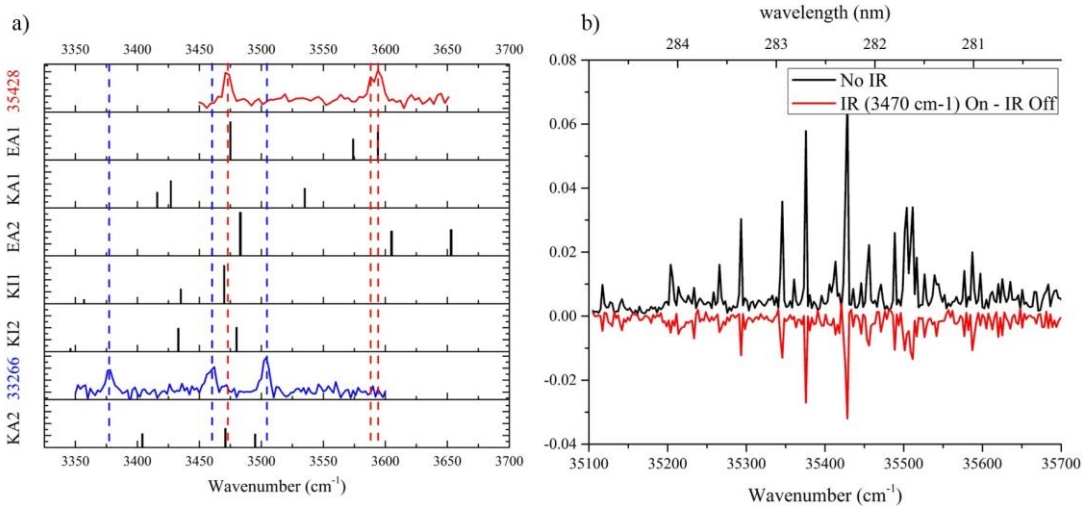


**Figure 4**: (a) IR UV hole burning results compared to anharmonic simulations for the 6 low energy structures. Experimental spectra are from UV ns probe 35,428 (red) and ps probe 33,266 (blue) $cm^{-1}$ respectively. (b) ns 2C R2PI spectrum (black) and the difference trace below (red) when burning at the EA1 experimental wavelength of 3,470 $cm^{-1}$. Anharmonic DFT analysis calculated with the B3LYP hybrid functional and the cc-pVTZ basis set.

IR-UV double resonance spectroscopy reveals the presence of the EA1 tautomer, with the origin at 35,269 $cm^{-1}$ and the KA2 tautomer, with the feature at 33,266 $cm^{-1}$, shown by Figure

3a. We matched IR-UV hole burning spectra (probed as annotated in Figure 3a) with anharmonic computations. The peaks observed in the ns 2C R2PI scan are all correlated with the EA1 tautomer by IR-UV double resonance spectroscopy in which the IR resonance at 3,470 $cm^{-1}$ was held constant 200 ns prior to scanning the UV source (Figure 3b). We have attached UV-UV hole burning results at 35,428 $cm^{-1}$ as supplemental figure (S.2) which further confirms that all the peaks shown in the ns spectrum belong to a single tautomer which we identify as EA1. After characterization the KA2 and EA1 electronic origin transition energies correlated to within 10% of those predicted for KA1 and EA1 by Szabla et al. and KA1 by Hu et al.[21, 26]

Referring to Chart 1, KA2 is predicted to be the highest energy structure indicating that if this tautomer is present all other forms may be present in our beam as well. Jet-cooling is not an equilibrium process so we cannot predict the tautomer distribution but in our experience in our set-up usually the lowest energy tautomers up to typically about 50 kJ/mol are present. Furthermore, the KA1 tautomer was observed in matrix isolation experiments.[24-25] Three possible reasons certain tautomers are not observed in our experiment are the following. (1) There can be tautomers that absorb in different ranges of the UV spectrum, which we have not covered. (2) Our experiment measures action spectroscopy rather than direct absorption. It is possible that a molecule is excited by the first photon but not ionized by the second. One way this situation can occur is when the excited state lifetime is significantly shorter than the ionizing laser pulse. A very similar situation exists for guanine: the lowest energy keto tautomers, equivalent to KA1 in isoC, have not been observed so far by R2PI, although from direct absorption in microwave experiments and in He droplets they are known to exists.[31-32] (3) A molecule may undergo fragmentation after excitation or ionization adding complexity

to the action spectrum as we typically monitor only the parent ion mass. We did not observe any obvious non-statistical fragmentation.

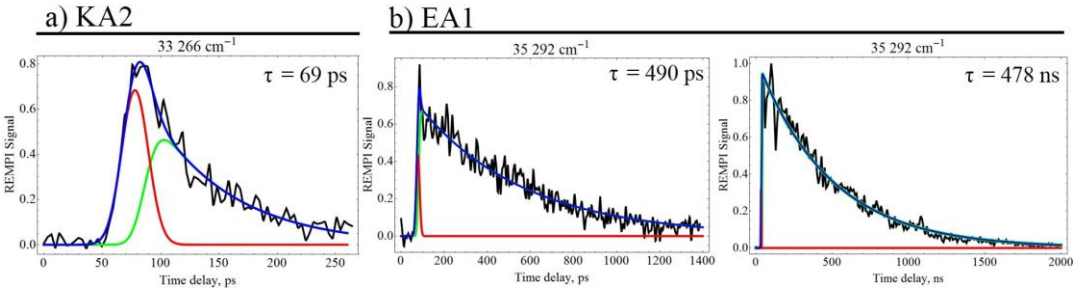


**Figure 5**: Pump-Probe results from the origin bands of (a) the KA2 and (b) the EA1 tautomer in the ps and ns regimes. The data in (a-b) is fit to a curve (blue) which is the sum of a single exponential decay convolved with a Gaussian component (green) representative of our instrument response function (IRF) and the IRF itself (red).

Figure 4 shows a selection of the pump-probe results from the origin transitions of EA1 and KA2; additional pump-probe fits are found in supplemental material (S.3). The derived lifetimes are shown within Figure 2a-b. The 463-491 ps lifetime of the EA1 tautomer represents the decay rate of the excited state. All pump-probe curves were fit to a mono-exponential decay.

We probed the broad elevated baseline signal present to the red of the EA1 origin in Figure 2a in hopes of attributing it to a specific species from Chart 1. The lifetime of 491 ps agrees with the ps component measured for EA1. We were unable to support this pump-probe correlation to EA1 with conclusive IR-UV hole burning results, like those from Figure 3a. The inability to obtain a clear IR-UV spectrum would be consistent with hot bands.

| | keto KA1 | keto KA2 | Enol |
|---|---|---|---|

| | | | |
|---|---|---|---|
| Isocytosine | N/O | 69 ps | 489 ps / 478 ns |
| Cytosine | N/O | 730 ps[33] / 290 ns[34] | *56 ps / *30.5 ns |
| Guanine | N/O | N/O | 13 ns[35] / 40 ns[35] |

**Table 1** Vibrationless excited state lifetimes. N/O = not observed. *These reported pump-probe results for enol-C were not obtained at the 0-0 transition but rather on the rising edge of its broad initial absorption region

Table 1 lists vibrationless excited state lifetimes, following 0-0 excitation unless otherwise noted, which we found here for isoC and compares those with the equivalent lifetimes for C and G. In terms of its photo-dynamics, isoC has elements of both G and C. The six membered ring in G is an amino-pyrimidione, identical to isoC with a five membered ring that immobilizes the C5=C6 bond that is free in isoC. Szabla et al. identified major conical intersections involving ring puckering, C=O stretching, $NH_2$ out-of-plane bending and C=C rotation.[21] The former three are similar to the CIs that dominate G dynamics[36] while the latter cannot occur in G but is characteristic for pyrimidines, including cytosine.[37]

We first compare isoC with G. Neither the 1H-9h-keto-amino (KA1 equiv) nor the 3H-keto-amino (KA2 equiv) have been identified yet by ps or ns R2PI. So in both isoC and G we do not observe the KA1 form (because of the difference in numbering between pyrimidines and purines this is N3H for isoC and N1H for G, see Figure 1). For G this is the WC form and is slightly less in energy than the imino forms, which are observed.[36, 38] As noted before, one likely reason for not observing a species with R2PI is an excited state lifetime significantly

shorter than the laser pulse length. In the G experiments pulse widths were of the order of 5 ns and in the current isoC experiments they are lower limited at 30 ps. Excited states with lifetimes of the order of a few hundred fs could thus defy detection by R2PI in these experiments. Notably the conical intersection that is most responsible for the ultrafast IC in the G keto case involves pyramidalization at the C2 position and does not involve the 5-membered ring[29, 36, 39-40] Therefore, it is possible for the isoC KA1 form to undergo very similar ultrafast IC. For the KA2 form of isoC we find a lifetime of 69 ps while the equivalent form for G was not observed with R2PI although it is lower in energy than the imino forms that are observed with R2PI.[31-32, 41] For both compounds the enol form is significantly longer lived, with two independent decay channels of almost 0.5 ns and 0.5 μs for isoC and 13 ns and 40 ns for G.[35] In both cases we consider that the long lived dark state could be a triplet state and for G the 13 ns decay can be attributed to fluorescence.[42] In the case of enol isoC the observation of two decays with a 3 orders of magnitude difference implies that those two channels do not decay from the same excited state. If they did, the higher rate process would have 3 orders of magnitude larger quantum yield and dwarf the signal from the lower rate process. Instead we assume an ultrafast population of a doorway state, possibly a triplet, which in turn decays at the slow rate.

In comparing isoC and C we notice larger differences in excited state dynamics. Again we do not see the KA1 equivalent form for C, which is about 30 kJ/mol higher in energy than the WC KA2 equivalent and enol forms. The KA2 form, which is the lowest energy keto form for C, behaves very different from isoC. Leutwyler and coworkers have reported this case in great detail, finding a vibrationless decay time of 730 ps.[33, 43-45] Nir et al. reported on a long lived state, presumably a triplet, with a 290 ns lifetime.[34, 46] These observations suggest different

dynamics than for isoC where we found a single 69 ps decay. For the enol form of C we find a 56 ps short component which populates a longer lived state with a 30.5 ns lifetime (shown in S4). Because the ns R2PI spectra of enol C, also reported by Nir et al., is broad and without a clear 0-0 transition[46] we performed these pump-probe measurements on the rising edge of the broad signal which appears along with the ps 2C R2PI in supplemental information (S.4). So for C the vibrationless excited state for the enol form is shorter lived than for the keto form, contrary to the situation for both G and isoC. Szabla et al. find a CI for the isoC enol that involves the C5=C6 twist, which also plays a role in C, however according their calculations only 14% of the trajectories follow this path in isoC.[21] It should be noted that their trajectories start at 5.5 ± 0.2 eV which is a full eV more excited state energy than what we impart in our experiments. This may suggest that the C5=C6 CI for EA1 has an energy barrier of up to 1 eV.

The conclusion that isoC resembles G in its photochemistry is just one of the considerations in evaluating its potential role in prebiotic scenarios. For example, we are currently investigating the photo-stability of isoguanine as one of its possible alternative base pair partners. Furthermore, the response to radiation is wavelength dependent and its consideration should not be limited to a single wavelength or small parts of the spectrum. The study of the dynamics near the threshold for absorption provides opportunities to probe the potential energy landscape close to the most relevant CIs and barriers. It is hoped that these data will serve as support for further detailed theoretical treatments.

**Experimental section**

Here we report results which identify the EA1 and KA2 tautomers of cold isocytosine prepared in a molecular beam. We have investigated the absorption spectrum with 2C R2PI,

identified the tautomers with IR-UV hole burning, and performed pump-probe experiments to probe excited state relaxation dynamics in the ns and ps time regimes. The instrument and explanation of these specific techniques are detailed elsewhere and very briefly outlined here.[35, 47] IsoC standard (Sigma, ≥99%) is entrained into a pulsed molecular beam by laser desorption and ionized by tunable 2C R2PI. The ps spectroscopic and pump-probe delay measurements are performed with a Nd:YAG driven Optical Parametric Oscillator (OPG) laser system which produces ~30 ps laser pulses. The molecule is excited by the tunable light from the OPG and ionized by 213 nm, which is mechanically delayed up to 1.5 ns before colineation with the OPG beam. A variable electronic delay between OPG UV laser and an excimer laser (193 nm, 6 ns pulse width) is used for spectroscopic and pump-probe measurements in the ns time delay range.

For IR-UV double resonant spectroscopy an optical parametric oscillator/amplifier (OPO/OPA) precedes the 2C R2PI by 200 ns. IR resonant frequencies are compared to anharmonic DFT analysis calculated with the B3LYP hybrid functional with the cc-pVTZ basis set.

***Supplemental Information***

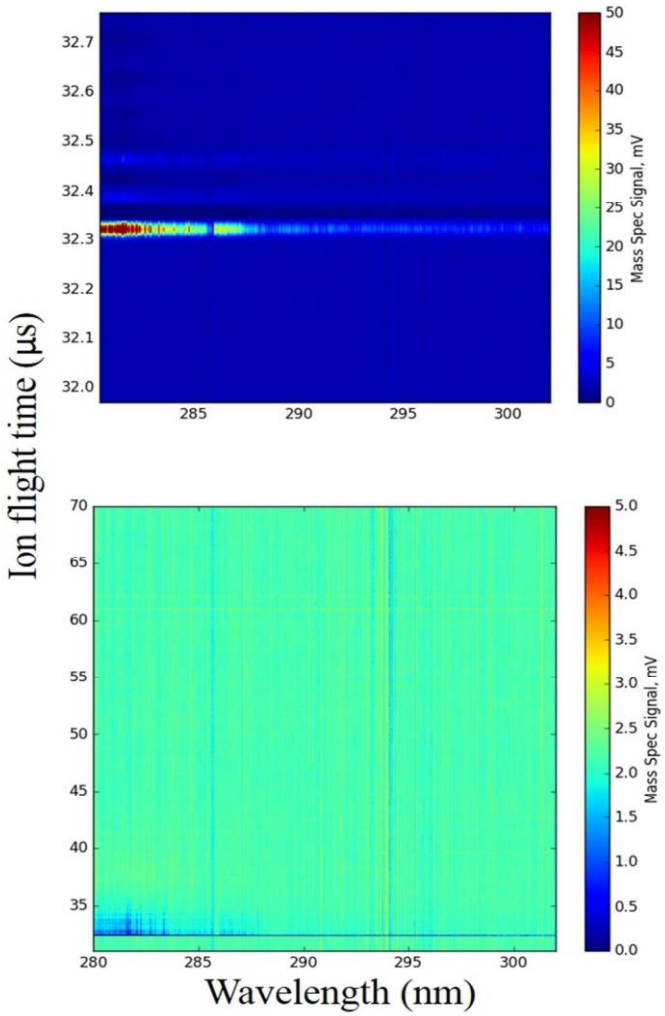


**Figure S1**: The two-dimensional time-of-flight data showing ion signal intensity (z axis 0-50 mv top, 05 mv bottom) with respect to flight time (y axis) and excitation wavelength (x axis). The only signal is the parent mass of isoC at 32.3 us across all wavelengths. Therefore, no signal is due to the fragmentation of higher order mass ions.

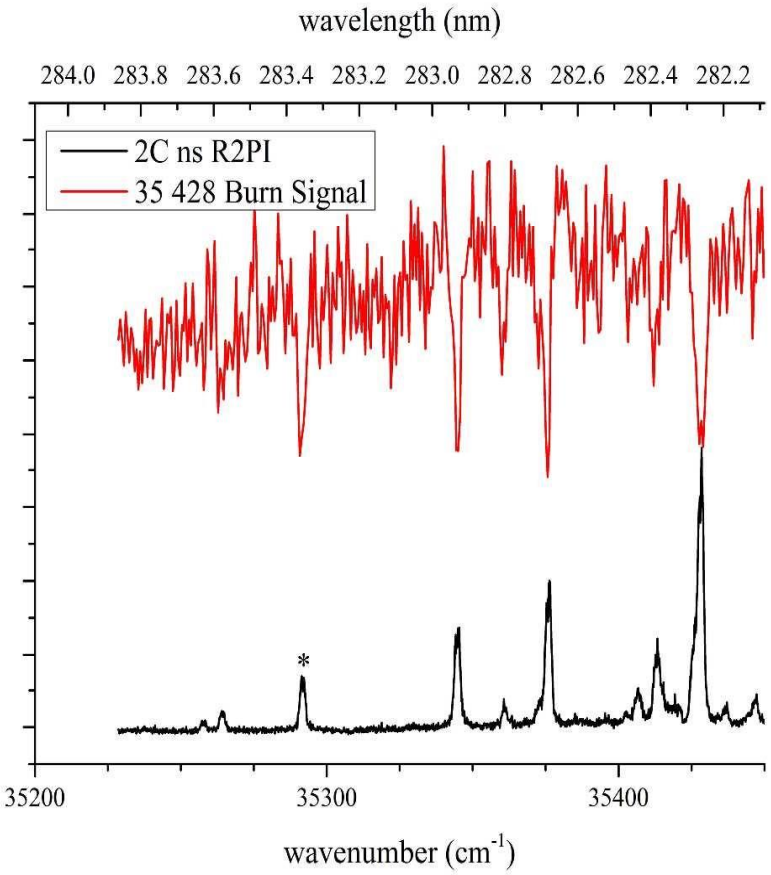


**Figure S2:** The UV-UV of the EA1 region (35,428 $cm^{-1}$ probe) supporting the IR-UV in Figure 3b that all signal in the ns scan within the shown range is from the EA1 tautomer only. The EA1 origin of 35,292 $cm^{-1}$ is starred (*).

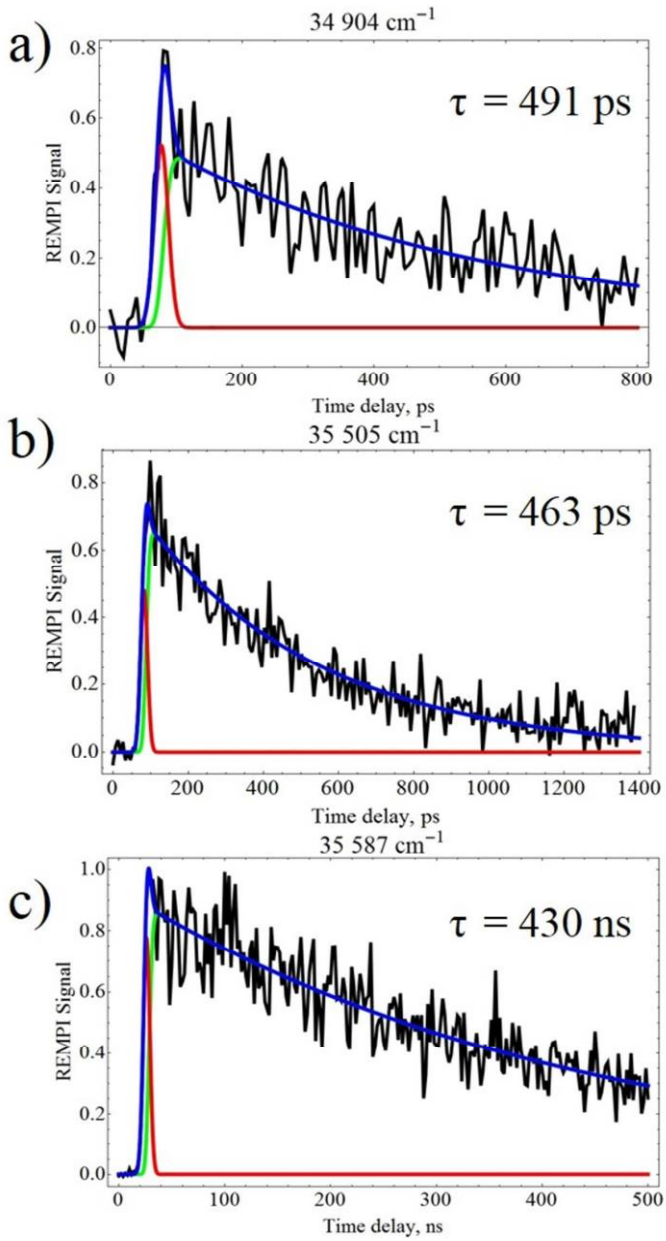


**Figure S3**: The pump-probe results (a) through (c) at excitations other than the 0-0 transition wavelengths. The data in (a-c) is fit to a curve (blue) which is the sum of a single exponential decay convolved with a Gaussian component (green) representative of our instrument response function (IRF) and the IRF itself (red).

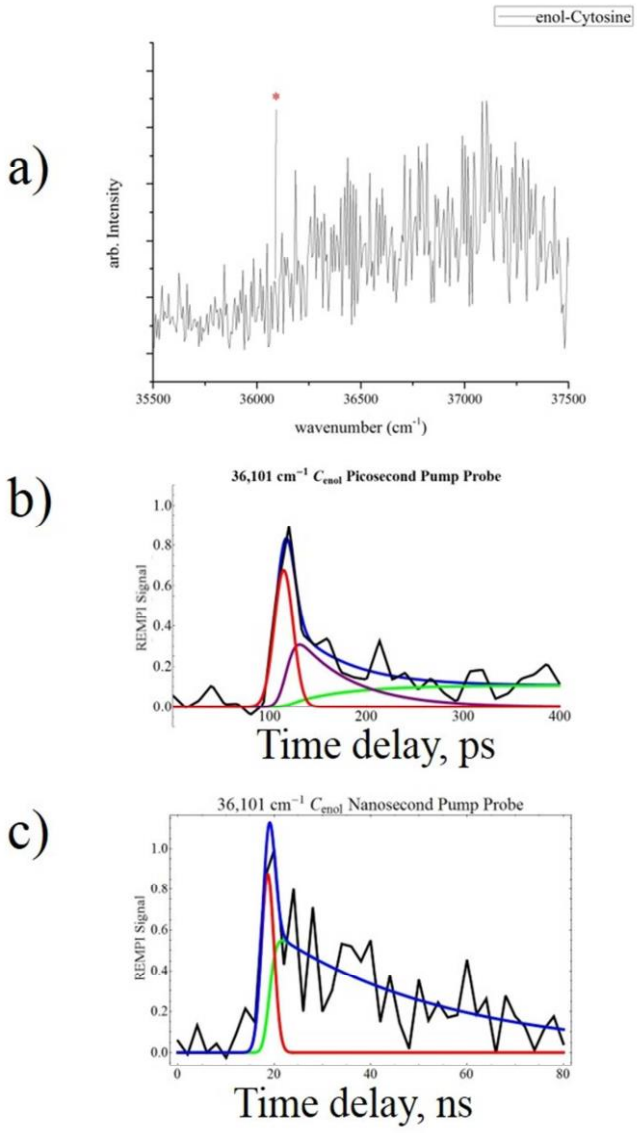


**Figure S4:** The (a) ps 2C R2PI and (b) ps pump-probe results of enol C. 213 nm was the second color for both, and (c) ns pump-probe results of enol C with 193 nm as a second color. In the ps pump probe two lifetimes were fit for, a short lifetime (purple) of 56 ps which populates a >5 ns secondary lifetime (green). The ns pump-probe fit to a single decay of 30.5 ns (green) In both the IRF is plotted in red. Our previous work on 6-TG showed the upper fitting limit of our ps setup to be ~5 ns, longer lifetimes need additional fitting in the ns regime.

# IV. Control of the Excited-State Intramolecular Proton Transfer in Nucleosides

The extensive study of the nucleobases revealed that the canonical bases relax often times orders of magnitude faster than their modified counterparts. The excited-state dynamics studies of the isolated bases, however, do not provide a complete picture of the overall dynamics of the much more complex structures of DNA and RNA. As such, the dynamics of the nucleosides have also been extensively analyzed both experimentally and theoretically. Previous finding predict that the sugar group attached to the nucleosides adenosine and guanosine create a new ultrafast relaxation pathway, an excited-state intramolecular proton transfer between the sugar and base. To confirm its relevance in the mechanism of these two nucleosides, the dynamics of adenosine and guanosine as well as modified analogues that remove the hydroxyl groups necessary for proton transfer were measured.

## *I. Selective Substitution of the Donor Groups Responsible for the Fast Excited-State Intramolecular Proton Transfer in the Nucleosides Guanosine and Adenosine*

Trevor Cohen, Ana D. Parejo Vidal, Charlie Smith, Julia Didziulis, Mattanjah de Vries
University of California, Santa Barbara. Department of Chemistry and Biochemistry

***Abstract***

On an early Earth, it is hypothesized that the likely absence of an atmospheric ozone layer allowed for significant amounts of UV radiation to reach the planet and exert an evolutionary pressure over the chemicals present on its surface. This hypothesis has been further corroborated by studies comparing the canonical nucleotides to similar structures substituted analogues that could perform the replication mechanisms necessary for life, which found that upon photoexcitation, the canonical bases relax significantly faster than their alternative base competitors. However, addition of the sugar group necessary to form a

double helix has been theoretically found to introduce new pathways for relaxation, of note an ultrafast excited-state intramolecular proton transfer between the sugar and base. However, the significance of this process in the overall dynamics of the nucleosides has yet to be fully analyzed experimentally. To further explore the significance of this process and the excited-state dynamics of DNA, we present the absorption spectra and excited-state lifetime of guanosine and adenosine in the gas phase using Resonance Enhanced Multi-Photon Ionization. Further study of a modified guanosine that removed all hydroxyl groups on the sugar molecule revealed a longer lifetime compared to conventional guanosine suggesting a blocking of this mechanism. A similarly substituted adenosine, however, exhibited no measurable change in excited-state lifetime, revealing that ESIPT is either not contributing to the mechanism or that a new relaxation pathway is formed by the substituents.

### *1.Introduction*

Since the observations made by Darwin in the mid-1800's, it is well accepted that the slow evolution of organisms on Earth are driven by pressures due to the environment and competing species sharing the same habitat. While his original observations were tailored to macroscopic changes in wildlife on the Galapagos Islands, these same principles can be applied to molecules on the nanoscale and their ability to resist destruction or mutation into other forms. It is theorized that on an Early Earth, based on studies simulating the synthesis of various nucleosides in the conditions of the time, there were a diverse number of molecules available that could have formed the eventual building blocks of life.[1-3] Evidence of the canonical nucleobases, as well as these nonconventional pyrimidine and purine bases have even been found on meteorite samples acting as the original source for these

compounds.[4,5] Other studies have found the precursor materials necessary to form these nucleobases and analogues on the surface of the Earth.[6-8] Whether these molecules were formed in the vacuum of space or in the harsh environments of a prebiotic Earth, it is predicted that the Sun's rays irradiating the Earth would act as a significant pressure on the eventual formation of the double-helix DNA structure we observe presently.

On a prebiotic Earth free of life capable of producing oxygen, it is predicted that the composition of the Earth's atmosphere was significantly different. In particular, a lack of oxygen produced from photosynthesis suggests that there was no ozone layer capable of absorbing the harmful UV radiation produced from the sun.[9,10] It has been found that a molecule's proficiency to quickly release the energy it absorbs upon photoexcitation is directly related to its photostability and consequently contributes largely to its ability to survive for longer periods of time.[11] Consequently, a multitude of experiments have been conducted measuring the interactions between UV radiation and the canonical nucleobases and analogues predicted to be present 4 billion years ago. Resultantly, it was found that the canonical DNA and RNA bases relax through nearly barrierless ultrafast pathways to conical intersections leading to high lightfastness.[12-17] Conversely, analogues of the canonical bases were found to relax on longer timescales and thus more susceptible to photodamage.[17-19]

In conjunction with excited-state lifetime trends, the canonical bases and relevant analogues were studied both experimentally and theoretically to determine the structural dependence on their relaxation pathways. For the canonical bases, key features such as the freedom to twist about the C5-C6 bond in the pyrimidines and some purines as well as the pyramidization about the C2 position in the purines lead to near barrierless pathways to a

conical intersection back to the ground state.[14,15,17,20] These trends are consistent in both solution and in the gas phase.[21-23] The purine and pyrimidine alternatives, however, remove, add, or substitute various functional groups onto the heterocyclic structures often inhibiting motion or shifting electron density blocking the once available pathways for a fast relaxation.[24-31] In some cases, the relaxation becomes fluorescence dominant yielding useful tags in biological research.[32]

The dynamics studies of the nucleobases have developed a well-defined landscape of the possible mechanisms available for DNA strands. Addition of a sugar group onto a nucleobase, a necessary component for the formation of the double helix structure, produces a nucleoside providing more complexity to the excited-state potential energy surface and forms new potential pathways for the molecule relax with. One of the first measurements of the excited-state dynamics of the nucleosides was performed by Pecourt et al. using transient absorption spectroscopy revealing an ultrafast internal conversion to the ground state.[33] Domcke et al. found through theoretical calculations of the nucleoside adenosine that the molecule is capable of relaxing on an ultra-fast timescale through an excited-state intramolecular proton transfer (ESIPT) and back transfer between the hydroxyl group at the 5' position and the nucleobase.[34] Further studies in the gas and solution phase measured ultra-fast non-radiative mechanisms, but no evidence of the ESIPT was found.[35-38] Mirroring the trends of the isolated nucleobase, addition of a thio and thieno group onto guanosine was found to slow the rate of relaxation to the microsecond timescale promoting fluorescence.[39,40]

Previously, we measured the absorption spectra of isolated guanosine as well as 2' and 3' deoxyguanosine in the gas phase using Resonance Enhanced Multi-Photon Ionization

(REMPI).[41] Further hole burning spectra found that guanosine was only observed in its syn conformation positioning the hydroxyl group at the 5’ position capable of ESIPT.[42] Removal of an -OH group on the sugar moiety at the 2’ position did not destabilize the structure in guanosine or adenosine.[43,44] However, substitution of an O-ethyl group at the 5’ position destabilized guanosine leading to the formation of the anti conformation suggesting the 5’ hydroxyl group stabilizes the syn structure.[45]

To probe the ESIPT process, we present the absorption spectra and the excited-state lifetime measurements of guanosine, adenosine, as well as the analogues 2’,3’-dideoxo-5’-O-ethylguanosine and 5’-chloro-2’,3’-isopropylidine adenosine using REMPI and pump probe spectroscopy (see Scheme 1 for structures). The lifetime measurements of adenosine and guanosine lifetimes were on the order of 50 ps and 1 ns respectively. Substitution of the 5’ hydroxyl group with chlorine on adenosine showed little change in the excited-state lifetime suggesting that the chlorine atom may be able to perform excited-state charge transfer or that the molecule has an alternative mechanism of relaxation that does not involve ESIPT. Removal of all hydroxyl groups on the sugar moiety of guanosine did

however slow the excited-state lifetime two-fold, providing evidence for ESIPT as part of the mechanism of relaxation.

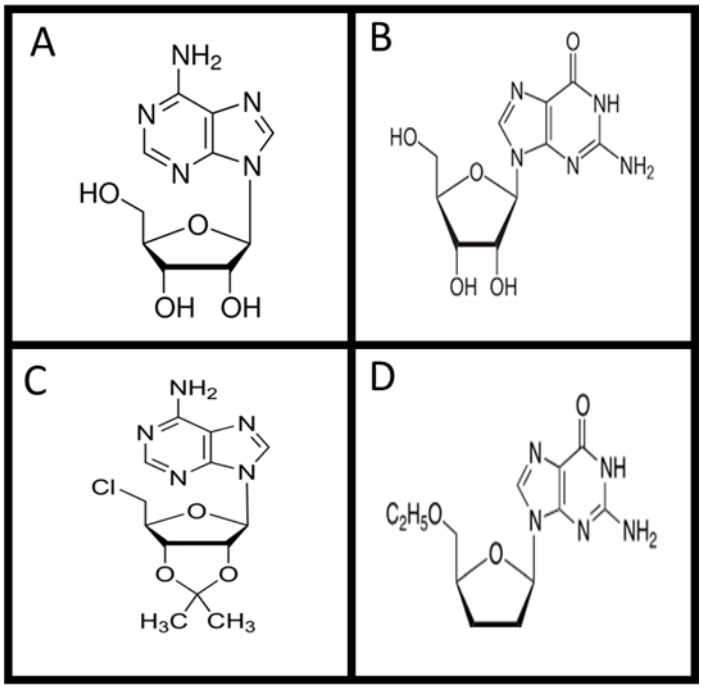


Scheme 1: Chemical structures of adenosine (A), guanosine (B), 2',3'-deoxo-5'-chloro-isopropylidine adenosine (C), and 2',3'-deoxo-5'-O' ethyl-guanosine (D).

***2.Methods***

***2.1 Synthesis of 2',3'-dideoxo-5'-O-ethylguanosine***

To an oven-dry, argon-purged, 50 mL round-bottom flask was added 2',3'-Dideoxyguanosine (Combi-Blocks, 250 mg, 1 mmol, 1 equiv), then 18 mL anhydrous *N*,*N*-dimethylformamide (DMF, Aldrich). The white, cloudy suspension was cooled in dry ice/acetonitrile bath for 5 min, then bromoethane (TCI, 1.5 mL, 21 mmol, 21 equiv) was added dropwise. The white, cloudy suspension was continually stirred in the cooling bath an additional 5 min, then NaHMDS (CHEM-IMPEX, 367 mg, 2 mmol, 2 equiv) was added as a solution in 3 mL anhydrous DMF dropwise over 5 min. The reaction mixture remained cloudy and white and was stirred with continued cooling for 10 h, then allowed to warm to

room temperature gradually overnight. At room temperature, the reaction was clear and slightly yellow. It was cooled again in the dry ice/acetonitrile bath, and quenched with 2 mL methanol, then stirred with continued cooling for 2 h, then allowed to warm to room temperature. An additional 2 mL water was added, and the reaction mixture was concentrated by rotary evaporation to a white residue. The crude reaction mixture was purified by column chromatography ($SiO_2$, $CH_2Cl_2$ to 95:5 $CH_2Cl_2$:methanol) to isolate 68 mg 2',3'-dideoxo-5'-O-ethylguanosine as a colorless oil (24%). $^1$H NMR (400 MHz, DMSO-$d_6$): δ 7.86 (s, 1H), 7.02 (s, 2H), 5.98 (dd, *J* = 6.9, 3.4 Hz, 1H), 4.18-4.03 (m, 1H), 3.97 (q, *J* = 7.0 Hz, 2H), 3.72 (dd, *J* = 11.3, 3.8 Hz, 1H), 3.62 (dd, *J* = 11.3, 4.8 Hz, 1H), 2.44-2.22 (m, 2H), 2.07-1.95 (m, 2H), 1.11 (t, *J* = 7.0, 3 H).

### *2.2 Experimental*

The REMPI technique has been described in detail previously, and thus will only be briefly described here.[46] The guanosine, adenosine, and 5'-chloro-2',3'-isopropylidine adenosine were purchased from Sigma Aldrich at 99% purity, while 2',3'-dideoxo-5'-O-ethylguanosine was synthesized as described above. For all REMPI techniques, the samples were placed onto a graphite bar and loaded into the experiment chamber ($2x10^{-6}$ torr working pressure). A 5 ns laser pulse produced by a Minilite I (1064 nm fundamental, 10 hz) laser is fired at the graphite substrate. Through laser desorption, the high impulse laser from the Nd:YAG laser system promotes the molecules to the gas phase while also minimizing fragmentation. Pressurized Argon (8 Barr backing pressure) is pulsed through a general valve nozzle (150 μs pulse width, 10 hz) resulting in the supersonic expansion of the carrier gas and collisional cooling the sample to approximately 15 K. The sample is directed

through a skimmer into the mass spectrometer where the spectroscopic techniques are performed.

REMPI is a broad term used to describe any multi-photon technique that resonantly excites followed by ionization of the sample gas. For each measurement taken on the picosecond timescale, the laser pulses are formed from an EKSPLA PL2551 Nd:YAG pump laser (1064 nm, 10 hz, 30 ps pulse width). To produce laser pulses from 250-700 nm with 0.05 nm bandwidth, the third harmonic of the pump laser is split using a 50:50 beam splitter and sent into two PG401 optical parametric generators (OPG). Each molecule was first characterized using 1-Color Resonance Enhanced 2 Photon Ionization (R2PI). To perform this the wavelength of the laser produced from one of the OPG units was scanned and sent into the experimental chamber spatially and temporally intersecting the sample gas. Upon successful resonant excitation, a second photon from the same laser pulse provides enough energy to ionize the sample. The newly formed ions are accelerated through a time-of-flight mass spectrometer and an absorption spectrum is constructed measuring ion count versus the wavelength of light used.

To measure the excited-state lifetime of each molecule, pump probe spectroscopy was performed at each origin transition found from the R2PI spectra. The laser pulse produced from one of the OPG units is fixed to the wavelength of the origin transition guaranteeing excitation and ionization. In order to measure the relative population of the molecules that can be ionized at as a function of the ionization pulse delay, it is necessary that the excitation and ionization pulses are temporally independent from one another. Because of this, a separate laser pulse is generated from the second OPG unit so that it can be separately delayed from the excitation laser. The ionization pulse is delayed using a Thorlabs

mechanical delay stage (300 mm, 2 ns maximum delay) providing a 6.67 ps resolution delay for the measurements. The wavelength of the ionization laser is chosen for each molecule by examining their R2PI spectra and selecting a wavelength slightly to the red of their origin transition assuring that this ionization pulse does not resonantly excite the molecule. However, the non-resonant ionization pulse is in direct competition with the excitation laser that is also capable of ionization as seen in the 1-Color R2PI. To minimize ionization from a single laser, the excitation laser is externally attenuated to the minimum threshold power necessary to measure any signal in the mass spectrometer. The new ionization laser is then cross propagated and spatially overlapped with the excitation pulse to avoid attenuation, enhancing the ionization process. The resultant spectra formed by delaying this ionization laser is fitted with a Mathematica script described previously.[29]

## *3. Results and Discussion*

### *3.1 Absorption spectra and insights into structure in the gas phase*

Figure 1 displays the R2PI spectra for guanosine, adenosine, and the substituted nucleosides. We have previously reported the absorption spectra of guanosine in the gas phase using a pulsed nanosecond dye laser, and the origin transition was measured at 34,302 $cm^{-1}$.[41] Using the picosecond laser system, we report the same origin transition, marked with an asterisk in Figure 1A, which will be further examined later in the pump probe studies. The spectrum is significantly broader than previously measured, especially at higher energies. This is likely caused by the lower wavelength resolution. Additionally, we have found that use of picosecond lasers to ionize excited molecules results in more efficient ionization of transitions with excited-state lifetimes lower than 1 ns. This broadening may also be the product of measuring more short-lived transitions previously not measured with

the longer laser pulse. The origin transition of adenosine is reported to be 37,453 $cm^{-1}$ (Figure 1B) with similarly broad features at higher energies. The addition of sugar moieties to the nucleobases provides more degrees of motion previously unavailable. For example, rotational freedom in the glycosidic bond could result in the spectral broadening measured.

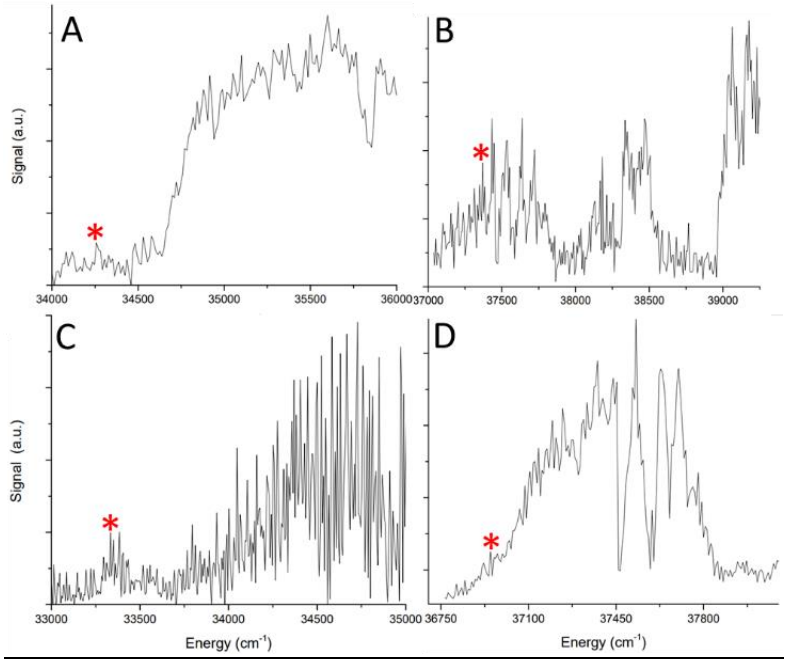


**Figure 1**: The R2PI spectra for guanosine (A), adenosine (B), 2',3'-deoxo-5'-O' ethyl-guanosine (C), and 2',3'-deoxo-5'-chloro-isopropylidine adenosine (D). The excited-state lifetimes were measured at the vibronic transitions labelled with an asterisk.

The substituted guanosine and adenosine compounds exhibited the same broadened features, with origins at 33,379 $cm^{-1}$ and 36,940 $cm^{-1}$ as seen in Figure 1C and 1D. While both modified nucleoside analogues exhibited a red shift in their origin transitions compared to their canonical counterparts, the substituted guanosine shifted significantly more. Conformational studies using IR-hole burning coupled with excited-state calculations of guanosine with a substituted ethyl ether group at the 5' revealed that the molecule was only observable in the anti conformation.[45] This significant change in conformation between

guanosine and its analogue revealed that without the hydrogen bonding between the 5' hydroxyl group and the nitrogen at the 3 position on the nucleobase, the less sterically hindered anti conformation is more favorable. Additionally, computational work on adenosine revealed that in the anti conformation, the 2' OH group can form a weaker hydrogen bond with the N3 atom compared to the 5' moiety, but nevertheless stabilizes the conformation.[34] The modified 2',3'-deoxo-5'-O' ethyl-guanosine and 2',3'-deoxo-5'-chloro-isopropylidine adenosine remove all hydroxyl groups from the sugar ensuring no hydrogen bonding between the sugar and base. Resultantly, the modified guanosine is predicted to be found in the anti conformation due to the steric effects.

Comparable studies removing the hydroxyl group from the 5' position of adenosine have not been performed, but adenosine is expected to behave in a similar manner. Removal of only the 2' and 3' hydroxyl groups in protonated adenosine did not result in a change in structure to the anti conformation.[44] Removal of the hydroxyl groups from the 2' and 3' positions in both analogues in the present study most likely do not largely contribute to the red shifting. The substituted adenosine and guanosine greatly differ in the compound substituted at the 5' position, chlorine for adenosine and an ether group for guanosine. This may indicate possible stabilization of adenosine in the syn conformation through use of the chlorine atom resulting in a smaller change in conformation and red shift. Further excited-state structural calculations are necessary for confirmation.

### *3.2 Proposed mechanism of relaxation nucleosides*

The excited-state dynamics of adenosine and guanosine have been previously studied theoretically as well as experimentally revealing new pathways that the sugarless nucleotides cannot utilize for relaxation. While we cannot definitively confirm the relaxation

mechanisms which these modified nucleosides utilize, we will speculate below. Through extensive structural and dynamics studies of the purine bases, it was determined that two key features of adenine and guanine provide pathways for the molecules to relax after photoexcitation: (1) a ring puckering of the C2, C6, and C8 positions and (2) a pyramidalization at the N9 position.[17] In addition to stabilizing guanosine and adenosine in the syn conformation, the 5' hydroxyl group the available relaxation mechanisms available such as through attachment of the sugar group at the N9 position, blocking the pathway previously available on the nucleotide. It is also now possible for the molecule to perform an excited-state intramolecular proton transfer (ESIPT) from the 5' OH to the nitrogen in the 3 position. A theoretical study calculating the relative energies of protonated adenine found that protonation at the N3 site was the lowest energy conformation for the 7H tautomer, the relevant structure of adenosine, but much higher for the 9H tautomer.[47] Fluorescence studies of protonated adenosine in solution further corroborated that protonation at the N3 position relaxed in approximately 500 fs, significantly faster than at the N1 position studied.[48] These studies reveal that sugar group addition both increases the relaxation rate of adenosine, and likely also guanosine, and promotes the most stable structure post transfer compared to protonation at alternative positions. After proton transfer, it is expected that guanosine and adenosine follow similar pathways back to the ground state as the protonated nucleotides. Dynamics calculations of protonated adenine found the C2 puckering mechanism was barrierless to reach a conical intersection to the ground state and predicted this process to be the fastest and dominant mechanism for the purine family of molecules.[47]

When considering the excited-state lifetime of the nucleosides, it is important to consider the rates of both the ESIPT and following internal conversion from the protonated base.

While relaxation through ESIPT is typically considered to be ultrafast, it is possible to slow the mechanism if for example the barrier to transfer is sufficiently high or broad promoting a slower tunneling through the barrier.[50] Prior theoretical studies of adenosine suggests that the barrier to proton transfer is nearly barrierless.[34,49] Internal conversion following ESIPT is likely the rate-limiting step in the overall process, and is further slowed by structural differences of the purines that are a part of adenosine and guanosine. While the dynamics of adenosine has been well studied, further dynamics calculations probing the excited-state potential energy surface (PES) of guanosine are necessary to understand the difference in trajectories available for this system.

### *3.3 Insight into the ESIPT mechanism through selective structural modification of the nucleosides*

Figure 2 shows the pump probe spectra taken at the origin of guanosine (A), adenosine (B), 2',3'-deoxo-5'-O' ethyl-guanosine (C), and 2',3'-deoxo-5'-chloro-isopropylidine adenosine (D). All were fitted with monoexponential decay curves to calculate the respective lifetimes. Guanosine exhibited a lifetime on the order of a nanosecond (Figure 2A). This lifetime is on the same order of magnitude as the non-Watson Crick tautomers of guanine previously measured, and a similar study of the dynamics of guanosine in the gas phase measured similar lifetimes.[15,37]

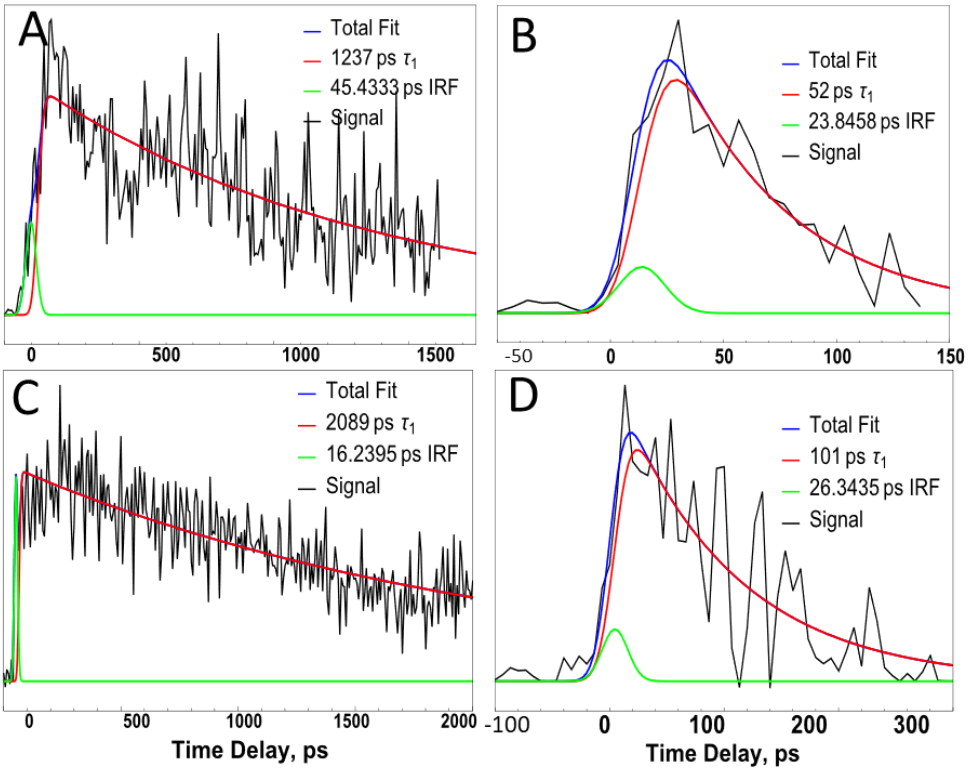


**Figure 2**: Pump probe spectra of guanosine (A), adenosine (B) 2',3'-deoxo-5'-O' ethyl-guanosine (C), and 2',3'-deoxo-5'-chloro-isopropylidine adenosine (D). Each pump probe was measured at their respective origin transition measured in the R2PI spectra.

2',3'-deoxo-5'-O' ethyl-guanosine is both found in the anti conformation and does not have a proton available to donate in the ESIPT process. The measured excited-state lifetime at the origin was on the order of 2 ns, a two-fold increase (Figure 2C). This provides further evidence that (1) guanosine utilizes ESIPT as one of the steps to relaxation and (2) blocking the ESIPT process from both 3' and 5' positions forces the molecule to utilize a different, much slower process to the ground state. It is likely that the modified guanosine relaxes similarly to the analogous unprotonated guanine, through slower contortions of the purine ring such as through puckering at the C2 position.[17]

Like adenine to guanine, adenosine relaxes on a much faster timescale than guanosine at approximately 52 ps (Figure 2B). A study of the nucleosides in the gas phase further corroborates that adenosine relaxes much more quickly than guanosine.[37] ESIPT is expected to be ultrafast and the dynamics are believed to be rate limited by the mechanisms that follow from the protonated bases. Thus, the significantly shorter lifetime compared to guanosine matches well with both the calculated excited-state potential energy surface of adenosine as well as the much faster relaxation rates between guanine and adenine.[14,34]

Removal of the OH moieties from guanosine lengthened the excited-state lifetime of the nucleoside but not for 2',3'-deoxo-5'-chloro-isopropylidine adenosine (Figure 2D). The measured lifetime of the substituted adenosine was 101 ps, within the bounds of error of the fitting algorithm used and thus the difference between the two is insignificant. It is necessary when considering the relaxation mechanism of adenosine and guanosine to consider the two ESIPT channels, starting from the 5' and 3' hydroxyl groups, available depending on whether the molecules are in their syn or anti conformation respectively. On both substituted nucleosides, the 2' and 3' hydroxyl groups were replaced with hydrogen in the guanosine analogue and isopropylidine in adenosine. This removes the ESIPT process present in the anti form in both compounds. At the 5' position, however, the hydroxyl group on adenosine was replaced with a chlorine atom, a highly electron withdrawing group compared to the ethyl ether substituted at the 5' position in guanosine. While ESIPT is still blocked at this position in adenosine, it is possible that a new mechanism to the ground state is utilized such through an excited-state charge transfer mechanism accounting for the similar lifetimes in the two adenosines. It is also possible that when ESIPT is blocked, adenosine relaxes like adenine, through similarly fast contortions of the purine ring. The pathway available through

the 9N atom on the purine is now blocked by the glycosidic bond and can no longer be utilized for relaxation, but contortion at the C2 and C6 positions are still possible. Further excited-state lifetime studies studying the effects of halogenic substitution at the 5' position is needed for a full understanding of the mechanism and structure.

### *4.Conclusion*

We present the absorption spectra and excited-state lifetimes of adenosine and guanosine in the syn conformation in the gas phase. Through measurement of the lifetime and absorption spectra of the selectively modified nucleosides, we find that removing the OH groups on 2',3'-deoxo-5'-O' ethyl-guanosine doubles the excited-state lifetime of the compound, while 2',3'-deoxo-5'-chloro-isopropylidine has no measurable difference. We conclude that guanosine and adenosine utilize ESIPT followed by internal conversion to quickly return to the ground state. Since the modified guanosine cannot undergo ESIPT, it likely relaxes utilizing a similar mechanism as guanine. The substituted adenosine similarly blocks any possible ESIPT but relaxes at the same rate as the unmodified nucleoside. Chlorine substitution at the 5' position of adenosine may thus possibly provide a different relaxation with similar rates to the ESIPT process.

### *References*


1. Orgel, L. E. Prebiotic chemistry and the origin of the RNA world. *Crit Rev Biochem Mol* **2004**, *39* (2), 99-123. DOI: 10.1080/10409230490460765.
2. Cafferty, B. J.; Gallego, I.; Chen, M. C.; Farley, K. I.; Eritja, R.; Hud, N. V. Efficient Self-Assembly in Water of Long Noncovalent Polymers by Nucleobase Analogues. *J Am Chem Soc* **2013**, *135* (7), 2447-2450. DOI: 10.1021/ja312155v.
3. Chen, M. C.; Cafferty, B. J.; Mamajanov, I.; Gallego, I.; Khanam, J.; Krishnamurthy, R.; Hud, N. V. Spontaneous prebiotic formation of a beta-ribofuranoside that self-assembles with a complementary heterocycle. *J Am Chem Soc* **2014**, *136* (15), 5640-5646. DOI: 10.1021/ja410124v From NLM Medline.
4. Callahan, M. P.; Smith, K. E.; Cleaves, H. J., 2nd; Ruzicka, J.; Stern, J. C.; Glavin, D. P.; House, C. H.; Dworkin, J. P. Carbonaceous meteorites contain a wide range of

extraterrestrial nucleobases. *Proc Natl Acad Sci U S A* **2011**, *108* (34), 13995-13998. DOI: 10.1073/pnas.1106493108 From NLM Medline.

5. Marin, L. G.; Bejaoui, S.; Haggmark, M.; Svadlenak, N.; de Vries, M.; Sciamma-O'Brien, E.; Salama, F. Low-temperature Formation of Carbonaceous Dust Grains from PAHs. *Astrophys J* **2020**, *889* (2). DOI: ARTN 10110.3847/1538-4357/ab62b7.

6. Saladino, R.; Neri, V.; Crestini, C.; Costanzo, G.; Graciotti, M.; Di Mauro, E. Synthesis and Degradation of Nucleic Acid Components by Formamide and Iron Sulfur Minerals. *Journal of the American Chemical Society* **2008**, *130* (46), 15512-15518. DOI: 10.1021/ja804782e.

7. Saladino, R.; Crestini, C.; Pino, S.; Costanzo, G.; Di Mauro, E. Formamide and the origin of life. *Phys Life Rev* **2012**, *9* (1), 84-104. DOI: 10.1016/j.plrev.2011.12.002 From NLM Medline.

8. Saladino, R.; Botta, G.; Delfino, M.; Di Mauro, E. Meteorites as Catalysts for Prebiotic Chemistry. *Chem-Eur J* **2013**, *19* (50), 16916-16922. DOI: 10.1002/chem.201303690.

9. Ranjan, S.; Sasselov, D. D. Influence of the UV Environment on the Synthesis of Prebiotic Molecules. *Astrobiology* **2016**, *16* (1), 68-88. DOI: 10.1089/ast.2015.1359 From NLM Medline.

10. Ranjan, S.; Sasselov, D. D. Constraints on the Early Terrestrial Surface UV Environment Relevant to Prebiotic Chemistry. *Astrobiology* **2017**, *17* (3), 169-204. DOI: 10.1089/ast.2016.1519 From NLM Medline.

11. Otterstedt, J. A. Photostability and Molecular-Structure. *J Chem Phys* **1973**, *58* (12), 5716-5725. DOI: Doi 10.1063/1.1679196.

12. A. L. Sobolewski and W. Domcke, Europhy. News, 2006, 37, 20-23.

13. Middleton, C. T.; de La Harpe, K.; Su, C.; Law, Y. K.; Crespo-Hernandez, C. E.; Kohler, B. DNA excited-state dynamics: from single bases to the double helix. *Annu Rev Phys Chem* **2009**, *60*, 217-239. DOI: 10.1146/annurev.physchem.59.032607.093719 From NLM Medline.

14. Satzger, H.; Townsend, D.; Zgierski, M. Z.; Patchkovskii, S.; Ullrich, S.; Stolow, A. Primary processes underlying the photostability of isolated DNA bases: Adenine. *P Natl Acad Sci USA* **2006**, *103* (27), 10196-10201. DOI: 10.1073/pnas.0602663103.

15. Abo-Riziq, A.; Grace, L.; Nir, E.; Kabelac, M.; Hobza, P.; de Vries, M. S. Photochemical selectivity in guanine-cytosine base-pair structures. *P Natl Acad Sci USA* **2005**, *102* (1), 20-23. DOI: 10.1073/pnas.0408574102.

16. Sobolewski, A. L.; Domcke, W.; Hattig, C. Tautomeric selectivity of the excited-state lifetime of guanine/cytosine base pairs: The role of electron-driven proton-transfer processes. *P Natl Acad Sci USA* **2005**, *102* (50), 17903-17906. DOI: 10.1073/pnas.0504087102.

17. Zgierski, M. Z.; Fujiwara, T.; Lim, E. C. Conical intersections and ultrafast intramolecular excited-state dynamics in nucleic acid bases and electron donor-acceptor molecules. *Chem Phys Lett* **2008**, *463* (4-6), 289-299. DOI: 10.1016/j.cplett.2008.06.024.

18. Boldissar, S.; de Vries, M. S. How nature covers its bases. *Physical Chemistry Chemical Physics* **2018**, *20* (15), 9701-9716. DOI: 10.1039/c8cp01236a.

19. Rapf, R. J.; Vaida, V. Sunlight as an energetic driver in the synthesis of molecules necessary for life. *Physical Chemistry Chemical Physics* **2016**, *18* (30), 20067-20084. DOI: 10.1039/c6cp00980h.

20. Beckstead, A. A.; Zhang, Y. Y.; de Vries, M. S.; Kohler, B. Life in the light: nucleic acid photoproperties as a legacy of chemical evolution. *Physical Chemistry Chemical Physics* **2016**, *18* (35), 24228-24238. DOI: 10.1039/c6cp04230a.

21. Ligare, M.; Siouri, F.; Bludsky, O.; Nachtigallova, D.; de Vries, M. S. Characterizing the dark state in thymine and uracil by double resonant spectroscopy and quantum computation. *Physical Chemistry Chemical Physics* **2015**, *17* (37), 24336-24341. DOI: 10.1039/c5cp03516c.

22. Crespo-Hernandez, C. E.; Cohen, B.; Hare, P. M.; Kohler, B. Ultrafast excited-state dynamics in nucleic acids. *Chem Rev* **2004**, *104* (4), 1977-2019. DOI: DOI 10.1021/cr0206770.

23. Crespo-Hernandez, C. E.; Cohen, B.; Kohler, B. Base stacking controls excited-state dynamics in A-T DNA. *Nature* **2005**, *436* (7054), 1141-1144. DOI: 10.1038/nature03933.

24. Hare, P. M.; Crespo-Hernandez, C. E.; Kohler, B. Internal conversion to the electronic ground state occurs via two distinct pathways for pyrimidine bases in aqueous solution. *P Natl Acad Sci USA* **2007**, *104* (2), 435-440. DOI: 10.1073/pnas.0608055104.

25. Frey, J. A.; Ottiger, P.; Leutwyler, S. Watson-Crick and Sugar-Edge Base Pairing of Cytosine in the Gas Phase: UV and Infrared Spectra of Cytosine center dot 2-Pyridone. *J Phys Chem B* **2014**, *118* (3), 682-691. DOI: 10.1021/jp409660b.

26. Trachsel, M. A.; Lobsiger, S.; Schar, T.; Blancafort, L.; Leutwyler, S. Planarizing cytosine: The S(1) state structure, vibrations, and nonradiative dynamics of jet-cooled 5,6-trimethylenecytosine. *J Chem Phys* **2017**, *146* (24), 244308. DOI: 10.1063/1.4989465 From NLM PubMed-not-MEDLINE.

27. Trachsel, M. A.; Wiedmer, T.; Blaser, S.; Frey, H. M.; Li, Q. S.; Ruiz-Barragan, S.; Blancafort, L.; Leutwyler, S. The excited-state structure, vibrations, lifetimes, and nonradiative dynamics of jet-cooled 1-methylcytosine. *Journal of Chemical Physics* **2016**, *145* (13). DOI: Artn 13430710.1063/1.4964091.

28. obsiger, S.; Trachsel, M. A.; Den, T.; Leutwyler, S. Excited-State Structure, Vibrations, and Nonradiative Relaxation of Jet-Cooled 5-Fluorocytosine. *J Phys Chem B* **2014**, *118* (11), 2973-2984. DOI: 10.1021/jp500410s.

29. Nachtigallova, D.; Lischka, H.; Szymczak, J. J.; Barbatti, M.; Hobza, P.; Gengeliczki, Z.; Pino, G.; Callahan, M. P.; de Vries, M. S. The effect of C5 substitution on the photochemistry of uracil. *Phys Chem Chem Phys* **2010**, *12* (19), 4924-4933. DOI: 10.1039/b925803p.

30. Siouri, F. M.; Boldissar, S.; Berenbeim, J. A.; de Vries, M. S. Excited State Dynamics of 6-Thioguanine. *J Phys Chem A* **2017**, *121* (28), 5257-5266. DOI: 10.1021/acs.jpca.7b03036.

31. Berenbeim, J. A.; Boldissar, S.; Siouri, F. M.; Gate, G.; Haggmark, M. R.; Aboulache, B.; Cohen, T.; de Vries, M. S. Excited-State Dynamics of Isocytosine: A Hybrid Case of Canonical Nucleobase Photodynamics. *J Phys Chem Lett* **2017**, *8* (20), 5184-5189. DOI: 10.1021/acs.jpclett.7b02032.

32. Gate, G.; Szabla, R.; Haggmark, M. R.; Sponer, J.; Sobolewski, A. L.; de Vries, M. S. Photodynamics of alternative DNA base isoguanine. *Physical Chemistry Chemical Physics* **2019**, *21* (25), 13474-13485. DOI: 10.1039/c9cp01622h.

33. Tor, Y.; Del Valle, S.; Jaramillo, D.; Srivatsan, S. G.; Rios, A.; Weizman, H. Designing new isomorphic fluorescent nucleobase analogues: the thieno[3,2-d]pyrimidine core. *Tetrahedron* **2007**, *63* (17), 3608-3614. DOI: 10.1016/j.tet.2007.01.075.

34. Pecourt, J. M. L.; Peon, J.; Kohler, B. DNA excited-state dynamics: Ultrafast internal conversion and vibrational cooling in a series of nucleosides. *J Am Chem Soc* **2001**, *123* (42), 10370-10378. DOI: 10.1021/ja0161453.

35. Tuna, D.; Sobolewski, A. L.; Domcke, W. Mechanisms of Ultrafast Excited-State Deactivation in Adenosine. *J Phys Chem A* **2014**, *118* (1), 122-127. DOI: 10.1021/jp410121h.

36. Buchner, F.; Heggen, B.; Ritze, H. H.; Thiel, W.; Lubcke, A. Excited-state dynamics of guanosine in aqueous solution revealed by time-resolved photoelectron spectroscopy: experiment and theory. *Physical Chemistry Chemical Physics* **2015**, *17* (47), 31978-31987. DOI: 10.1039/c5cp04394h.

37. Buchner, F.; Ritze, H. H.; Lahl, J.; Lubcke, A. Time-resolved photoelectron spectroscopy of adenine and adenosine in aqueous solution. *Physical Chemistry Chemical Physics* **2013**, *15* (27), 11402-11408. DOI: 10.1039/c3cp51057c.

38. De Camillis, S.; Miles, J.; Alexander, G.; Ghafur, O.; Williams, I. D.; Townsend, D.; Greenwood, J. B. Ultrafast non-radiative decay of gas-phase nucleosides. *Phys Chem Chem Phys* **2015**, *17* (36), 23643-23650. DOI: 10.1039/c5cp03806e.

39. Chan, R. C. T.; Chan, C. T. L.; Ma, C. S.; Gu, K. Y.; Xie, H. X.; Wong, A. K. W.; Xiong, Q. W.; Wang, M. L.; Kwok, W. M. Long living excited state of protonated adenosine unveiled by ultrafast fluorescence spectroscopy and density functional theoretical study. *Physical Chemistry Chemical Physics* **2021**, *23* (11), 6472-6480. DOI: 10.1039/d0cp06439d.

40. Martinez-Fernandez, L.; Gavvala, K.; Sharma, R.; Didier, P.; Richert, L.; Marti, J. S.; Mori, M.; Mely, Y.; Improta, R. Excited-State Dynamics of Thienoguanosine, an Isomorphic Highly Fluorescent Analogue of Guanosine (vol 25, pg 7375, 2019). *Chem-Eur J* **2019**, *25* (59), 13648-13648. DOI: 10.1002/chem.201904278.

41. Reichardt, C.; Guo, C.; Crespo-Hernandez, C. E. Excited-State Dynamics in 6-Thioguanosine from the Femtosecond to Microsecond Time Scale. *J Phys Chem B* **2011**, *115* (12), 3263-3270. DOI: 10.1021/jp112018u.

42. Nir, E.; Imhof, P.; Kleinermanns, K.; de Vries, M. S. REMPI spectroscopy of laser desorbed guanosines. *J Am Chem Soc* **2000**, *122* (33), 8091-8092. DOI: 10.1021/ja000502c.

43. Nir, E.; Hunig, I.; Kleinermanns, K.; de Vries, M. S. Conformers of guanosines and their vibrations in the electronic ground and excited states, as revealed by double-resonance spectroscopy and ab initio calculations. *Chemphyschem* **2004**, *5* (1), 131-137. DOI: 10.1002/cphc.200300862.

44. Abo-Riziq, A.; Crews, B. O.; Compagnon, I.; Oomens, J.; Meijer, G.; Von Helden, G.; Kabelac, M.; Hobza, P.; de Vries, M. S. The Mid-IR spectra of 9-ethyl guanine, guanosine, and 2-Deoxyguanosine. *J Phys Chem A* **2007**, *111* (31), 7529-7536. DOI: 10.1021/jp072183i.

45. Wu, R. R.; Yang, B.; Berden, G.; Oomens, J.; Rodgers, M. T. Gas-Phase Conformations and Energetics of Protonated 2 '-Deoxyadenosine and Adenosine: IRMPD Action Spectroscopy and Theoretical Studies. *J Phys Chem B* **2015**, *119* (7), 2795-2805. DOI: 10.1021/jp509267k.

46. Asami, H.; Urashima, S.; Tsukamoto, M.; Motoda, A.; Hayakawa, Y.; Saigusa, H. Controlling Glycosyl Bond Conformation of Guanine Nucleosides: Stabilization of the anti Conformer in 5 '-O-Ethylguanosine. *J Phys Chem Lett* **2012**, *3* (5), 571-575. DOI: 10.1021/jz300081e.

47. Meijer, G.; Devries, M. S.; Hunziker, H. E.; Wendt, H. R. Laser Desorption Jet-Cooling of Organic-Molecules - Cooling Characteristics and Detection Sensitivity. *Appl Phys B-Photo* **1990**, *51* (6), 395-403. DOI: Doi 10.1007/Bf00329101.

48. Shahrokh, L.; Omidyan, R.; Azimi, G. Excited state deactivation mechanisms of protonated adenine: a theoretical study. *Phys Chem Chem Phys* **2022**, *24* (24), 14898-14908. DOI: 10.1039/d2cp00106c.

49. Chan, R. C. T.; Chan, C. T. L.; Ma, C. S.; Gu, K. Y.; Xie, H. X.; Wong, A. K. W.; Xiong, Q. W.; Wang, M. L.; Kwok, W. M. Long living excited state of protonated adenosine unveiled by ultrafast fluorescence spectroscopy and density functional theoretical study. *Phys Chem Chem Phys* **2021**, *23* (11), 6472-6480. DOI: 10.1039/d0cp06439d.

50. Nielsen, S. B.; Solling, T. I. Are conical intersections responsible for the ultrafast processes of adenine, protonated adenine, and the corresponding nucleosides? *Chemphyschem* **2005**, *6* (7), 1276-1281. DOI: 10.1002/cphc.200400644.

51. Leyh, B. Ion Dissociation Kinetics in Mass Spectrometry. *Encyclopedia of Spectroscopy and Spectrometry, 3rd Edition, Vol 2: G-M* **2017**, 300-308. DOI: 10.1016/B978-0-12-409547-2.05195-7.

## V. Development of Tip Enhanced Laser Desorption

Detailed chemical analysis of material surfaces, ie., identification, quantification, and imaging of chemical functionality, at high spatial resolution is a challenge faced in many fields. In the current landscape of characterization techniques, it is difficult to achieve both high spatial resolution while also obtaining highly detailed structural analysis of surface features. Effective separation of the two processes would, however, allow for independent spatial and chemical analysis optimization. Tip Enhanced Laser Desorption was developed as a sub-micron sampling method in which material beneath an AFM probed is desorbed from a highly localized area, vaporizing the sample, and recollected onto a new sample substrate. Each area desorbed is sufficiently separated to avoid cross-contamination and can be characterized with techniques such as REMPI that are both highly sensitive and provide detailed structural analysis of the compounds that compose the surface. Below, the development of TELD and studies of the underlying mechanism of the technique is reported.

### *I. Tip Enhanced Laser Desorption: Technique Development for Spatially Resolved Nano-Scale Surface Sampling for ex-situ Chemical Analysis*

*Trevor Cohen, Ana Parejo Vidal, Nico Estebanez, Michael Gordon, Mattanjah de Vries*

**Abstract**

Detailed chemical analysis of material surfaces, ie., identification, quantification, and imaging of chemical functionality, at high spatial resolution is a challenge faced in many fields. There are many techniques available that can either image with high resolution or characterize with high chemical selectivity. However, it is difficult to achieve both high spatial resolution and chemical selectivity simultaneously. By collecting material with high spatial selectivity separate from the characterization of the sample, it is possible to achieve both high spatial and chemical resolution while maintaining flexibility in the choice of analytical technique for the desired characterization. Here, we present the development of a

novel sub-micron sampling technique, Tip Enhanced Laser Desorption (TELD), that when coupled with sensitive analytical detection, can provide detailed spatial and chemical information of a complex surface.

## 1. Introduction

In the past century, techniques designed to characterize complex material surfaces have advanced quickly to meet the demands of fields such as semiconductors and photovoltaics. While techniques such as Matrix Assisted Laser Desorption Ionization (MALDI) and Atomic Force Microscopy (AFM) are capable of either highly sensitive mass resolved molecular characterization and nanoscale imaging respectively, a technique that can provide achieve both high spatial resolution and chemical specificity currently is not possible.

Several material characterization techniques do exist that provide both chemical and spatial information, e.g., SEM/EDX, SIMS, imaging XPS, and SERS/TERS, but they all have drawbacks. For instance, some provide elemental information only (SEM/EDX, SIMS), making complex sample identification impossible. Other techniques are spatially limited to, i.e., a few microns for XPS/SIMS, depending on the x-ray and focused ion beam spot size or the optical diffraction limit (SERS). One promising technique developed by Zenobi et al. sought to sample a surface with high spatial selectivity with a Near-Field Scanning Optical Microscope and characterize with an ion trap mass spectrometer.[1] However, since the instruments were on-line, spatial resolution was sacrificed to desorb enough material for the mass spectrometer's to detect. Ghorai et al. developed a sub-micron sample preparation technique that fired a pulsed laser at a tapping AFM probe.[5] Through utilization of the lightning rod effect, the energy was able to transfer from the laser through the apex of the tip to the surface, desorbing the sample. However, the heating efficiency was

too low resulting in primarily melting of the surface material decreasing the spatial sensitivity of the process. A highly sensitive technique that measures the thermal expansion of a surface after successful absorption of infrared light measure by a tapping mode AFM probe, AFM-IR, has been shown to measure elucidate conformational structure from a surface.[6-8] However, the non-localized laser pulse fired at the surface lowers spatial resolution and requires expensive preparation of the sample surface.

In this paper, we developed a novel sample preparation method, Tip Enhanced Laser Desorption (TELD), in an AFM platform for high spatial resolution sampling of materials surfaces combined with ex situ REMPI and MALDI-based chemical characterization of the collected material (Figure 1). The TELD technique relies on a pulsed nanosecond or picosecond laser and an AFM probe, absorbing the pulse. The probe acts as a lightning rod directing the energy to the surface resulting in desorption with high localization and fast heating rate. Desorbed material is collected through a sampling capillary and redeposited onto a surface for off-line characterization and analysis. High spatial resolution is inversely related to the amount of material desorbed per event. To attain the highest spatial resolution, we choose resonant enhanced multi-photon ionization (REMPI) for its high detection sensitivity and mass and wavelength selectivity. Additionally, to showcase the flexibility of the off-line sample preparation, simultaneous detection of a heterogenous mixture of coronene and indigo were detected with Matrix-free Laser Desorption Ionization Mass Spectrometry (LDI-MS) was performed.

## 2. Experimental

### 2.1 Chemical Samples and Preparation

Solid samples of coronene and indigo were purchased from Sigma Aldrich at 99.9% purity. To prepare the samples for TELD, vapor deposition was utilized to evenly deposit thin layers onto glass microscope slides. A home-built vapor deposition apparatus was built capable of holding vacuum as low as 5 x $10^{-6}$ Torr. Approximately 20 mg of each sample was placed in a ceramic holder and slowly heated at 8 x$10^{-6}$ Torr until all material was evaporated from the sample holder. The glass slides were then glued to a magnetic disc and analyzed under an AFM.

**2.2 TELD**

A schematic of the TELD technique can be found in Figure 1. The TELD device is composed of three parts: the AFM that images the surface, the laser that desorbs material from sub-micron regions, and the substrate holder that collects the vaporized material in order to redeposit the material for further analysis. For imaging, a Veeco Multimode SPM was refurbished and installed in contact AFM mode in order to image the sample surfaces. All TELD experiments used two tips for validation of the methodology of the technique, a probe covered in approximately 50 nm of gold on all faces to promote optical plasmonic enhancement and energy transfer, and a silicon nitride probe as a control, both designed to be run in contact mode and purchased from Ted Pella. To perform the TELD process, a pulsed Nd:YAG nanosecond laser (Minilite I, 1064 nm fundamental, 10 Hz) frequency doubled to produce 532 nm light is directed at the AFM probe at approximately 5$^{o}$ above parallel to the surface. The pulse was focused using a 10 cm focal length planar convex lens to increase power density on the AFM probe. To maintain consistent alignment, a camera is placed above the AFM capable of imaging the laser pulse in real time. Sample collection is achieved by vacuum collection through a brass capillary (ID $\frac{1}{16}$") pumped by a rotary vane

pump connected to a vacuum sealed box. The sample substrate the material is redeposited onto is attached to a 3D-stage to allow for precise redeposition of material.

### 2.3 Chemical Analysis with REMPI and MALDI

After sub-micron removal and collection, the sample is analyzed using both Matrix Assisted Laser Desorption Ionization (MALDI) and Resonance Enhanced Multi-Photon Ionization (REMPI). For detection with MALDI, A Bruker Microflex Mass Spectrometer was used in linear time of flight mode. The sample was redeposited directly onto a stainless steel 96-well plate. Since the sample molecules were both sufficiently small and volatile, no matrix was needed for ample detection. For the quantification studies with coronene, each well that contained collected material fired at until complete depletion of the sample area. The integrated mass peak was compared to a calibration curve created with standardized solutions of coronene.

The REMPI technique has been extensively described in detail previously.[3] However, the unique detection parameters needed for TELD sample detection will be described below. All instruments in the REMPI apparatus were run at a 10 Hz cycle rate timed relative firing of the excitation laser pulse. TELD samples of indigo were redeposited on a graphite substrate designed for optimal detection with the instrument. The sample bar is loaded into the experimental chamber ($2x10^{-6}$ Torr working pressure) and placed on a motorized stage. To vaporize the sample material to be detected with REMPI, a 1064 nm pulse from a Minilite I nanosecond pulsed-laser is fired orthogonal to the substrate, quickly heating the substrate and desorbing the deposited sample. This laser wavelength is chosen for its high transmission of the samples analyzed and high absorption by the graphite substrate. A telescope connected to a video camera was aligned to monitor the position of the desorption

laser pulse to confirm where material was removed from the surface of the graphite substrate. The sample is then cooled to about 15 K through collisions with a molecular beam of argon pulsed into the chamber. Two laser pulses both spatially and temporally optimized to interact with the cooled sample are sent into the reaction chamber. To ensure the highest sensitivity, resonant detection of indigo was performed by fixing the wavelengths of both laser pulses to their optimal excitation and ionization wavelengths, at 551.6 and 213 nm respectively. The number of ions formed were measured in a time-of-flight mass spectrometer and measured relative to the area desorbed on the sample bar.

## 3. Preliminary Results and Discussion

### 3.1 Nanoscale sampling of surface material

To determine whether localized desorption is possible with the TELD apparatus, a methodology was developed to create and image the craters left behind post desorption. The desorption laser is first aligned onto the probe through a focusing lens at approximately 10 μJ per pulse to ensure the highest photon flux possible and to limit probe damage that occurs at higher pulse powers. The collection sniffer is then aligned approximately 10 μm from the AFM probe so as not to block the laser pulse from entering the AFM head. To measure the crater formed post desorption, an image of the surface is captured before TELD is performed. An example of a surface of indigo captured before TELD can be found in Figure 2A. The tip is then fixed to the target location on the surface and is illuminated by the pulsed laser, desorbing the material and simultaneously collecting the plumes through the sniffer. After TELD is completed, the AFM is scanned over the same area and upon successful desorption, a crater is imaged as seen in Figure 2B. To measure the size of the crater formed, the before and after images are exported into Matlab, shifted to correct errors in drift

between the two scans, and each pixel is height subtracted as seen in Figure 2C. To analyzed how different parameters affect the TELD process, the dimensions and volume of the height subtracted crater are calculated with an in house Matlab script. While coronene cannot absorb 532 nm light and indigo does, samples of both compounds were successfully desorbed using a gold probe and green light. Additionally, the average crater size at a fixed number of shots did not change between the two materials. This could suggest that absorption by the sample does not significantly contribute to the vaporization of material from the surface. Other properties such as thermal conductivity and expansion, volatility, and the smoothness of the surface may influence the crater's shape and size. Further studies are necessary to distinguish the prominent material properties that affect desorption.

To elucidate whether the AFM probe material influences the TELD mechanism, TELD was performed with a silicon nitride probe with the same spring constant (0.1 N/m) and the same force applied to the surface. The study was performed multiple times at various laser alignments to ensure the probe was bathed in the laser light. Upon height subtraction of the surfaces before and after TELD with the non-coated probe, no hole was measured as seen in Figure 2D. This suggests that the probe coating likely must absorb the laser wavelength fired at the probe. However, it is unclear whether after absorption, the energy transfer process is in the form of heat or a plasmonic event. If the energy transfer were plasmonic in nature, it is likely that the desorption crater geometry would be much smaller since the energy would be most enhanced at the apex of the tip. However, the desorption craters produced with a gold probe are much larger. It is thus likely that upon interaction with the pulsed laser, the metallized probe is quickly heated to a high enough temperature to vaporize the sample beneath the probe. To maintain correct for the change in normal force applied to the tip, the

probe indents into the surface leaving a crater behind in the shape of the square pyramidal probe.

SEM images were taken to monitor the effects of tip geometry after firing 230 μJ pulses directly onto the probe (Figure 3). After firing 10 pulses at the probe, the surface remained unchanged and deposited material that was present on the fresh probe was removed the probe surface. It is possible to fire a low number of pulses to clean the probe of any contamination on its surface, but further testing will be required to monitor this cleaning protocol with a more malformed probe. After approximately 150 pulses, clear malformation of the tip was localized to the surface face directly bathed by the laser light. This is most likely evidence of the gold coating reaching a high enough temperature to melt on the probe (1064 $^{o}$C) further corroborating that heating and indention is likely the underlying mechanism of TELD. After 1200 shots, the probe was completely malformed. However, the crater geometry remained unchanged after the 1200 shots malformation and remained intact until the probe was destroyed. While the probe was unable to measure very small features on the surface, it was possible to perform TELD until the tip destruction after approximately 30,000 shots. It is unclear whether firing smaller batches of pulses over longer periods of time may influence the lifetime of the probe. This phenomenon and other material properties of the probe will be explored in future studies.

### 3.2 Post-collection analysis via REMPI and MALDI

Desorbed material was collected and detected using two techniques with different detection sensitivities, REMPI-MS and matrix-free laser desorption ionization mass spectrometry (LDI-MS). For the REMPI study, a homogenous surface of indigo was desorbed with TELD, varying the numbers of shots fired and redeposited onto a graphite

sample bar. An image of the collected material on the graphite bar after collecting 0, 400, 200, and 100 shots of desorbed indigo can be seen in Figure 4A-D respectively. The sample bar was loaded into the experimental chamber to detect whether indigo was present along any location on the substrate. To monitor the location of the desorption laser on the bar, a video camera was attached to a telescope aligned along the path of the desorption laser. A resonant detection scan was performed measuring the number of ions detected in the TOF-MS with respect to desorption position, as seen in Figure 4. Through this study, it was found that only indigo was detected in the 400 shot redeposited area. Previous REMPI studies have shown a sensitivity of 1 ion of perylene detected for every $2x10^5$ molecules of desorbed from a substrate.[3] While the limit of detection of indigo has not been measured with REMPI, it should lie within the same order of magnitude as perylene. By assuming that purely indigo was removed from the surface due to TELD, it can be approximated through measurement of the crater volume that the crater formed from 400 shots removed approximately $3x10^7$ molecules from the surface. Resultantly, the TELD collection must have at minimum a 1% collection efficiency, otherwise the redeposited sample would lie below the limit of detection. Additionally, it is likely that negligible amounts of cross contamination into other spot occurred since no indigo was detectable on any other area of the sample bar.

TELD was also performed on a heterogenous surface of coronene and indigo to determine whether it was possible to simultaneously detect the two compounds with LDI-MS. Sample was similarly collected through the brass capillary sniffer and collected directly onto a 96-well MALDI plate. The LDI-MS spectrum of the collected mixed sample can be seen in Figure 5. Both coronene and indigo were detectable when desorbed from a crater formed with 400 laser shots with no evidence of fragmentation. Since there was no evident

fragmentation of the molecules, it is likely that after desorption with TELD, the surrounding atmosphere collides with the sample cooling the molecule fast enough to prevent any damage to the molecule. Additionally, characterization with a different technique from REMPI only required changing the substrate the material removed with TELD redeposits onto, showcasing the flexibility in the technique to produce highly spatially resolved samples for further off-line analysis.

## 4. Conclusion

Tip Enhanced Laser Desorption was developed, and a methodology was established to sample sub-micron areas from a sample surface for further off-line analysis with techniques such as REMPI and LDI-MS. It was found that to perform TELD, a tip coating that can absorb the laser light fired at the probe must be chosen, and no evidence of absorption directly by the surface has been found thus far. Analysis of the crater geometry suggests that the underlying mechanism of TELD is a heating and indention into the surface, but further studies varying properties of the laser, tip, and surface are necessary to fully determine the process. TELD samples made from a homogenous surface of indigo and a heterogenous surface of indigo and coronene were detected with REMPI and LDI-MS respectively, showcasing the flexibility of the off-line sample preparation technique. A minimum collection efficiency of 1% was established with REMPI, but further studies are necessary to determine the exact efficiency of TELD.

***Figures***

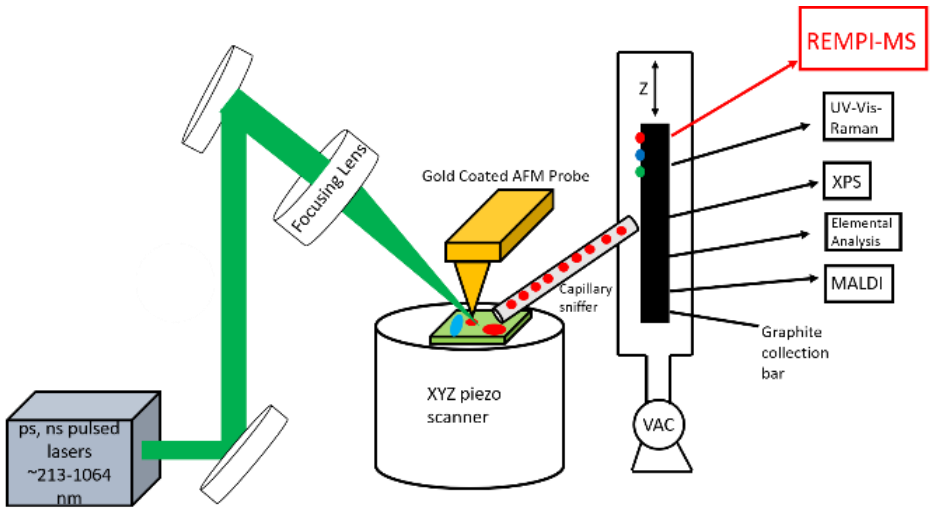


Figure 1: The overall schematic of TELD. Material is laser desorbed from the sample surface by directing a focused 532 nm pulse onto a gold coated probe. Through utilization of the lightning rod effect, desorption is localized to the area underneath the probe. The vaporized material is collected with a brass capillary sniffer and redeposited onto a new substrate for off-line analysis with a sufficiently sensitive chemical characterization technique.

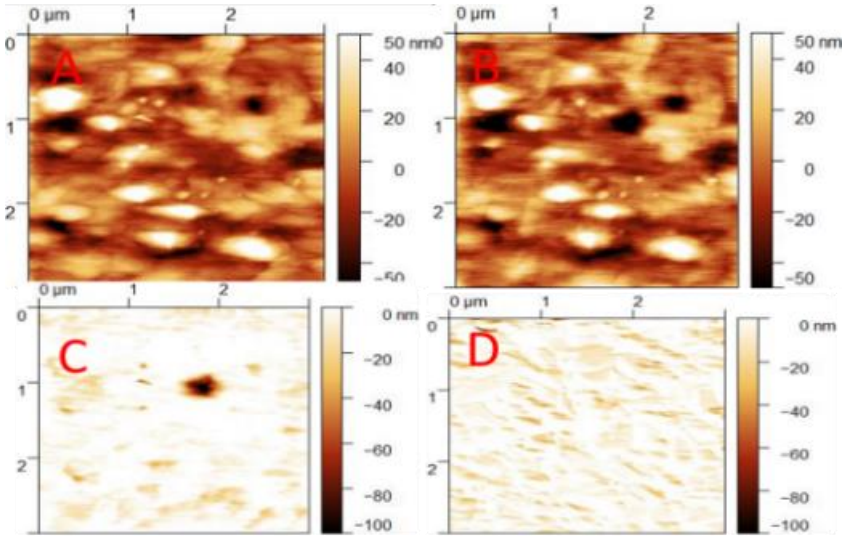


Figure 2: An image of an indigo surface before (A), and after (B) TELD was performed with a gold probe and a 532 nm laser pulse. The two images were shifted to correct image drift to produce a height subtracted image (C). The volume of the height subtracted image

measured 4.95 x $10^{-21}$ $m^3$. The study was reproduced with the same laser pulse and a silicon nitride probe and no crater was measurable in the difference image.

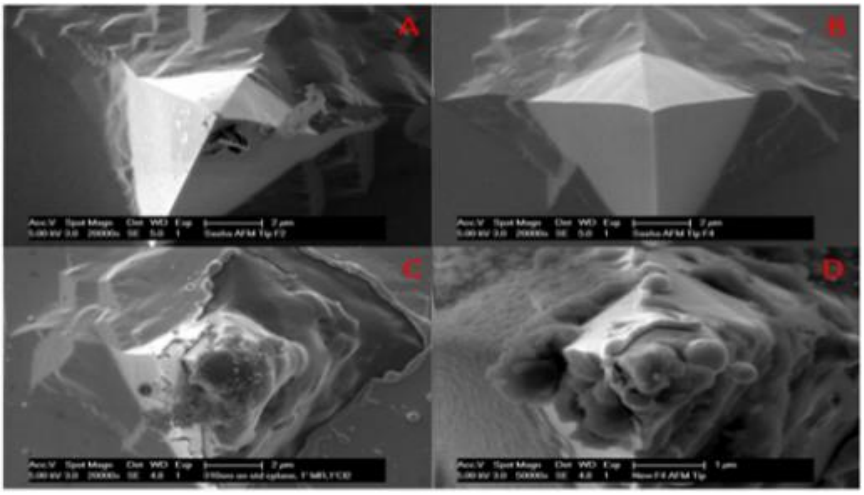


Figure 3: SEM images were taken of the gold coated probe after firing various numbers of 230 μJ laser pulses at the tip. At 0 shots (A), the probe remains intact and possibly collected material after imaging the surface. Firing the probe with 10 shots (B) resulted in no change in the surface and removal of the collected material on the exterior of the probe. 150 shots (C) show some malformation of the tip at the surface directly bathed in light by the laser. 1200 shots (D) results in complete geometry change of the probe, but no measurable effect on the TELD crater geometry.

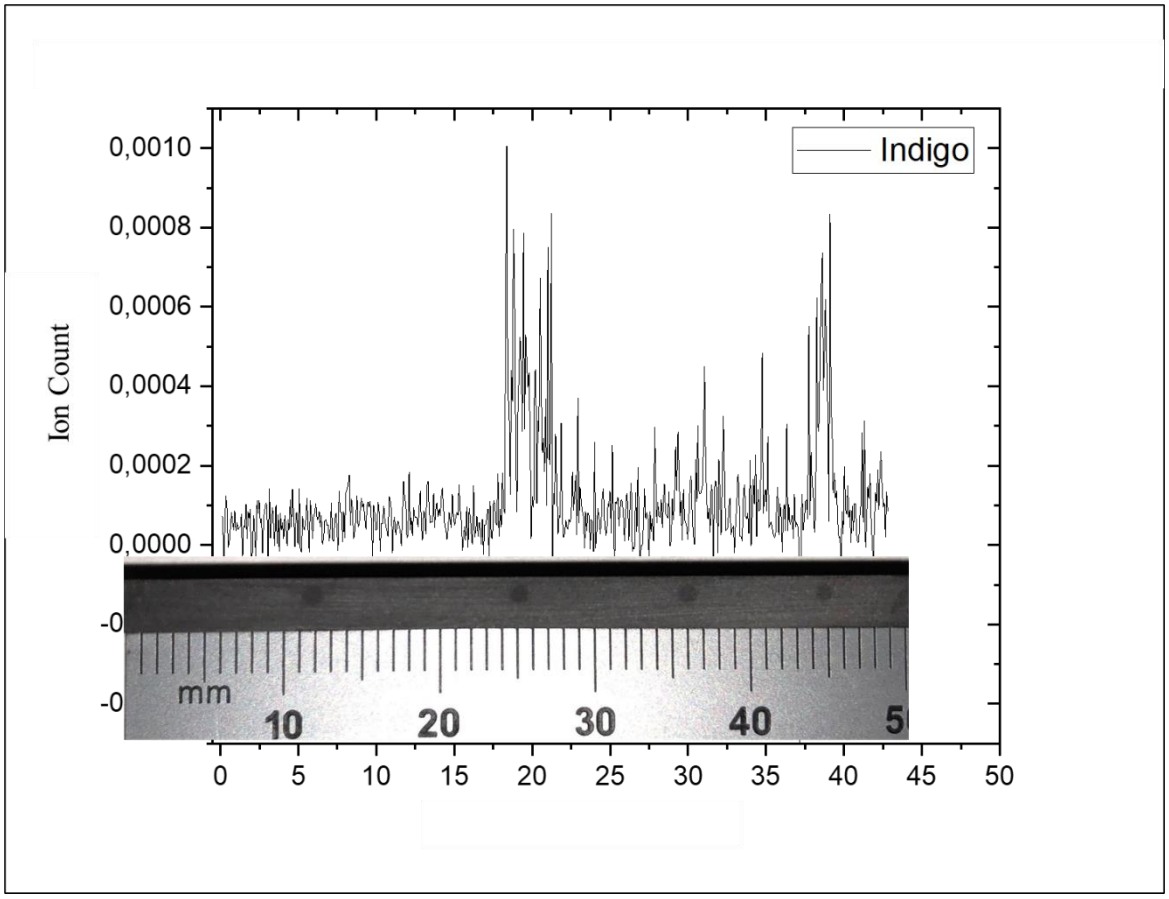


Figure 4: A single wavelength resonant detection scan of the graphite collection sample substrate. Craters were formed with 0 (A),400 (B), 200 (C), and 100 (D) laser pulses on a surface of indigo and collected onto distinct areas of the graphite bar. To detect the collected material, a single wavelength scan of indigo was first optimized with a test bar to ensure the highest sensitivity detection. The ion count formed after successful resonant excitation and ionization of indigo was measured while monitoring the area desorbed on the bar. Indigo was only detectable in the 400-shot crater.

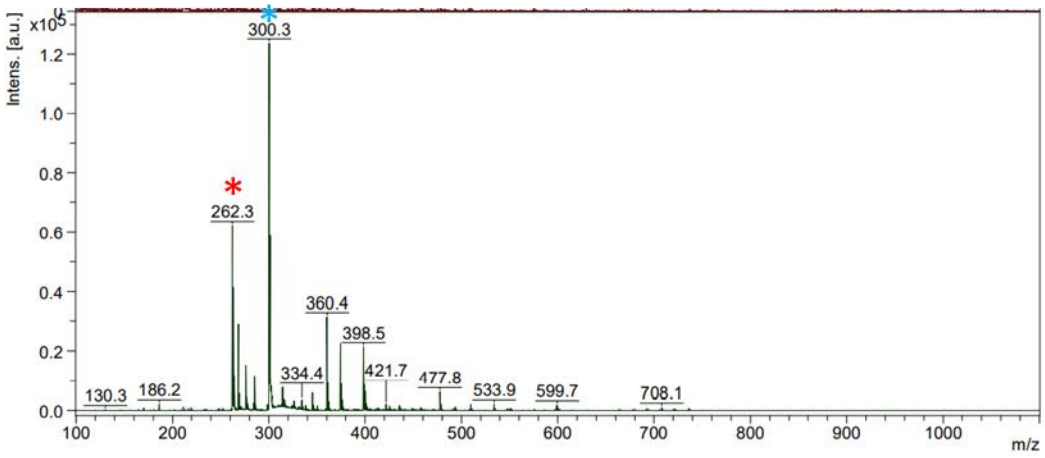


Figure 5: The MALDI spectra of a TELD sample collected from a heterogenous mixture of indigo and coronene. The coronene and indigo masses are marked with a red and blue star respectively.

***References***

**1.** Schmitz, T. A.; Gamez, G.; Setz, P. D.; Zhu, L.; Zenobi, R., Towards nanoscale molecular analysis at atmospheric pressure by a near-field laser ablation ion trap/time-of-flight mass spectrometer. *Anal Chem* 2008, *80* (17), 6537-6544.

**2.** 94. Zoric, Igor, et al. "Gold, Platinum, and Aluminum Nanodisk Plasmons: Material Independence, Subradiance, and Damping Mechanisms." *Journal of the American Chemical Society: Nanosciences*, vol. 5, no. 4, 2011, pp. 2535–2546.

**3.** Meijer, G.; de Vries, M. S.; Hunziker, H. E.; Wendt, H. R., Laser Desorption Jet-Cooling of Organic-Molecules: Cooling Characteristics and Detection Sensitivity. *Applied Physics B-Photophysics and Laser Chemistry* 1990, *51* (6), 395-403.

**4.** Owens, S. C.; Berenbeim, J. A.; Schmidt Patterson, C.; Dillon, E. P.; De Vries, M. S., Sub-Micron Proximal Probe Thermal Desorption and Laser Mass Spectrometry on Painting Cross-Sections. *analytical methods* 2014, *6* (22), 8940-8945.

5. Ghorai, S.; Seneviratne, C. A.; Murray, K. K. Tip-enhanced laser ablation sample transfer for biomolecule mass spectrometry. *J Am Soc Mass Spectrom* **2015**, *26* (1), 63-70. DOI: 10.1007/s13361-014-1005-x From NLM Medline.

6. Dazzi, A.; Saunier, J.; Kjoller, K.; Yagoubi, N. Resonance enhanced AFM-IR: a new powerful way to characterize blooming on polymers used in medical devices. *Int J Pharm* **2015**, *484* (1-2), 109-114. DOI: 10.1016/j.ijpharm.2015.02.046 From NLM Medline.

7. Morsch, S.; Lyon, S.; Greensmith, P.; Smith, S. D.; Gibbon, S. R. Mapping water uptake in organic coatings using AFM-IR. *Faraday Discuss* **2015**, *180*, 527-542. DOI: 10.1039/c4fd00229f From NLM PubMed-not-MEDLINE.

8. Morsch, S.; Liu, Y. W.; Lyon, S. B.; Gibbon, S. R. Insights into Epoxy Network Nanostructural Heterogeneity Using AFM-IR. *Acs Appl Mater Inter* **2016**, *8* (1), 959-966. DOI: 10.1021/acsami.5b10767.

# VI. Characterization of Novel Lasing Materials for Semiconductor Lasers

The demand for higher powered lasers at lower manufacturing and operating costs has quickly increased across a multitude of industries. Semiconductor lasers can be manufactured to produce a broad set of wavelengths of light ranging from the UV-IR, but some regions are not possible without the use of inefficient processes such as frequency up-conversion. The production and characterization of an InGaN/GaN quantum well is reported below. Pumping the material with a 355 nm pulsed laser resulted in lasing at 568 nm, a new lasing wavelength for semiconductor sources.

## *I. Demonstration of Yellow (568 nm) Stimulated Emission from Optically Pumped InGaN/GaN Multi-Quantum Wells*

Panpan Li[1], Haojun Zhang[1]*, Hongjian Li[1], Trevor Cohen[2], Ryan Anderson[1], Matthew S. Wong[1], Emily Trageser[1], Yi Chao Chow[1], Mattanjah de Vries[2], Shuji Nakamura[1], Steven P. DenBaars[1]

[1]Materials Department, University of California, Santa Barbara, CA, USA.

[2]Department of Chemistry and Biochemistry, University of California, Santa Barbara,

**Abstract**

We demonstrate room-temperature stimulated emission at 568 nm from low dislocation density InGaN/GaN multi-quantum wells. For a 1.4 mm long and 50 μm wide ridge bar optically pumped by a high-power pulsed laser, we observed an emission peak at 568 nm with a narrow spectral width of less than 2 nm at room temperature. The measured pumping threshold is less than 1.5 MW/cm$^2$ and the polarization ratio of the emission is over 90%.

This demonstration paves the way for the future development of electrically injected InGaN semiconductor yellow laser diodes.

## *1.* Introduction

Quantum well (QW) laser diodes (LDs) can be fabricated with a broad range of wavelengths, seamlessly spanning UV to mid-infrared depending on the choice of semiconductor material and structural design.[1, 2] Specifically, GaAs-technology enables the commercialization of LDs with wavelengths covering 630 nm to 1350 nm,[3, 4] whereas longer infrared wavelengths can also be accessed by InP and GaSb based structures.[5-7] GaN-based visible LDs from blue to green (400-530 nm) are already commercially available,[1, 8-12] yet reports about yellow semiconductor edge-emitting LDs are rare.[13] Nearly all yellow laser technology has been based on frequency conversion,[14] gas and ion lasers,[15] and dye lasers,[16] all of which are bulky, costly, and tremendously inefficient. Despite the scarcity of available yellow laser sources on the market, there is a fast-growing need for applications in advanced fields of biology and astrophysics.[17] Coherent and powerful yellow emission is an important component for use as a laser guiding star for astronomical observations.[18] With a direct-generation coherent yellow beam, quantum systems using heterogeneous integration of III-V LDs on silicon photonic platforms can be used to study photon entanglement,[19] which has not yet been realized due to the size constraints of current nonlinear yellow lasers.

Realizing high efficiency long-wavelength emission from InGaN QWs is still challenging, which can be obtained by increasing the indium composition in the InGaN QWs. [20-24] Additional indium in the InGaN lattice, however, requires a lower growth temperature and thus degrades epitaxial quality and dramatically decreases the internal

quantum efficiency (IQE).[20] The large lattice mismatch between InGaN QWs and GaN also results in a large piezoelectric field and a low IQE due to the poor electron and hole wavefunctions overlap, e.g. quantum-confined Stark effect (QCSE).[20, 21] The dispersion of GaN, InGaN and AlGaN materials has made it more challenging to achieve proper waveguiding and confinement of the photons, which is crucial for stimulated emission. Previous reports have shown the thickness of AlGaN cladding for adequate mode confinement in InGaN yellow LDs is beyond the critical thickness, and structures have been proposed to mitigate this issue.[25] For electrically pumped long-wavelength laser diodes, these challenges lead to a significant increase of threshold and prevent the lasing. In the optical pumping regime, however, issues such as carrier leakage and heat dissipation can be largely neglected and the optical gain from the material can be better exploited at a higher level.[26] However, there have not yet been reports about optically pumped lasing from edge emitting InGaN/GaN QWs.

In this study, we report a 568 nm yellow lasing from high crystal quality InGaN QWs grown on a bulk GaN substrate. Details of the materials growth, device fabrication, optically pumping experiment and lasing characterization are presented.

### *2. Methods*

The structure was grown on the *c*-plane bulk GaN substrate using atmospheric pressure metal organic chemical vapor deposition (MOCVD). Trimethylgallium (TMGa), triethylgallium (TEGa), trimethylaluminum (TMAl), trimethylindium (TMIn), bicyclopentadienyl ($Cp_2Mg$), disilane ($Si_2H_6$), and ammonia ($NH_3$) sources were used as precursors and dopants. The epitaxial structure consists of a 3 μm unintentionally doped (UID) GaN, a 1.5μm n-doped $Al_{0.06}Ga_{0.94}N$ as bottom cladding layer grown at 960℃, a 20 period $In_{0.12}Ga_{0.88}N$/GaN (1.5 nm/3 nm) superlattice (SL) as bottom waveguiding layer

grown at 920°C, a 6 period $In_{0.3}Ga_{0.7}N$ yellow QWs/AlGaN cap layers/GaN barriers (2 nm/2 nm/9 nm). The growth temperature of yellow QWs is 760°C. A 5 period $In_{0.12}Ga_{0.88}N$/GaN (1.5 nm /3 nm) superlattice as part of the top waveguiding layer grown at 920°C, and a 10 nm UID GaN as the cap layer. Our group has previously reported green and amber/red LEDs or micro-LEDs using similar active region growth conditions with a high external quantum efficiency.[22, 23]

Due to the nature of optical pumping, scattering loss and back-reflection could be a major source of photon loss during the pumping process, and the smoothness of the epitaxial surface is therefore crucial. Atomic force microscope (AFM) scanning exhibits a smoothness of the epitaxial layer with a roughness of 0.3 nm on a 5×5 $\mu m^2$ area as shown in Fig. 1(a).

Cathodoluminescence (CL) was used to measure the Threading dislocation (TD) density of the InGaN/GaN MQWs as shown in Fig. 1(b). The TD density was estimated to be ~$5\times10^7/cm^2$ by numerically counting the number of the black spots over a certain area, indicating a high crystal quality of InGaN/GaN MQWs. There still a lot of TDs generated during the epitaxy growth (bulk GaN has a TD of ~$10^6$ $cm^{-2}$) due to a low growth temperature and lattice mismatch in the InGaN yellow MQWs.

Due to the thickness limit of the high Al-content AlGaN layer that can be coherently grown on the GaN before relaxation occurs, it is not uncommon that in green or longer wavelength GaN LDs the optical mode is unsymmetrically skewed towards the substrate.[26] Such asymmetrical mode profile results in additional internal loss and lower modal gain due to weaker confinement. This issue would be exacerbated in the yellow (>560 nm) range due to the high dispersion of InGaN, which requires the top waveguiding layer to have near 10%

Indium composition and a thickness of more than 30 nm. To achieve better confinement, one can either increase the thickness of the cladding layer and replace it with a lower refractive index material or increase the refractive index of the waveguiding layer. In our experiment, a quarter-wave dielectric layer of $TiO_2$ on the top of the epitaxial growth was employed for symmetrical mode shaping. Compared with traditional epitaxial InGaN waveguiding and AlGaN cladding, the use of high refractive index of $TiO_2$ (near 2.6 at 580 nm)[27] on the top of active regions greatly improves the confinement in the vertical direction by attracting the mode upward, although such structure will not be valid for electrical injection of LDs. To further examine the validity of such a structure, mode simulation was conducted using the FIMMWAVE software (Fig. 2). In the structure using $TiO_2$ and $Ta_2O_5$, the center of the mode overlaps more with the active region.[28] It is worth noting that $TiO_2$ is also absorptive at the pumping wavelength (355 nm), yet when compared to high In-content InGaN, the absorption coefficient of $TiO_2$ is still lower. As seen from Table I, compared with a traditional structure with AlGaN cladding and high In-content InGaN waveguiding, the combined use of $Ta_2O_5$ and $TiO_2$ layers can enhance the confinement factor by nearly 25% while keeping the internal loss and single pass absorption of the pumping source still at the same level.

After the MOCVD growth, 38 nm $Ta_2O_5$ and 51 nm $TiO_2$ was deposited as cladding and waveguiding layers on the sample by using Ion Beam Deposition (IBD). The optical thickness of the $Ta_2O_5$ was also chosen as a quarter of the pumping wavelength to reduce the back reflection of the pumping beam while the $TiO_2$ thickness was determined to optimize the confinement factor and internal optical loss. Ridge patterns with different widths (20-50 μm) were formed by low power reactive ion etching to improve the sidewall

profile and reduce potential scattering loss. After fabrication, the sample was polished to 75 μm and cleaved into bars of different lengths ranging from 1 to 2 mm along the *m*-direction, as shown in Fig. 3. The cleaved *m*-plane facet shows a smooth surface that can be directly used for laser mirror without any optimization. The cleaved samples were then bonded onto a copper heat sink for testing.

The pumping source utilizes an EKSPLA PL2251 Series Nd:YAG pump laser with 1064 nm as fundamental wavelength. The beam is first sent through a second harmonic crystal combining two photons of the fundamental source to produce a 532 nm laser beam. Then this beam passes through a third harmonic crystal combining a 1064 nm and 532 nm pulse to produce the desired 355nm light output. The final pulse width is 30 ps firing at 10 Hz. Two 355 nm dichroic mirrors are used to filter out any residual light at the pumping wavelength. Finally, the beam passes through a cylindrical lens, focusing the spot into a narrow line of approximately 100 μm width (Fig. 4). Before each measurement, a power meter is also used to monitor the actual energy per pulse. A spectrometer (OceanOptics 2000) and a multi-mode fiber was placed near the facet and aligned in parrel with the ridges for spectrum and power collection.

Lasing action requires spontaneously emitted photons to be exponentially amplified by stimulated emission as they travel through the waveguide in the active medium, leading to a linear increase of the number of total photons. The generated photons are all coherent in space and frequency, and consequently, at the lasing threshold, an intense beam with spectral narrowing is expected from the facet of the device. The photon emission spectrum at roomtemperature with different pumping power densities is shown in Fig.5 (a). The peak emission wavelength was 568 nm with the spectral linewidth reducing from over 50 nm to

less than 2 nm at the measured pump-power of 1.5 MW/cm$^2$. The amplified spontaneous emission occurs at the peak of the broad spontaneous emission spectrum. The optical output power as a function of pumping power density (L-I curve) is also shown in Fig. 5(b), which exhibits a distinct "kink" of slope near $P_{th}$ of 1.25 MW/cm$^2$. Above threshold, the power of stimulated emission increases linearly with the pumping power density and gradually saturates at higher pumping level. Even though in practice electrically injected LDs have broader applications and impacts, an optically pumped device is undoubtedly a good indicator that the material quality is competent for future development and can be well regarded as a precursor to electrically injected LDs.

### *3. Results and Discussion*

To obtain a positive optical gain, Bernard-Duraffourg inversion condition must be satisfied. It is not only useful but also important to understand how the actual carrier density is correlated with the increasing pumping power density, as it will serve as a guidance for future design of electrically injected laser diodes. It has been observed that at the lasing threshold, the power density is 1.5 MW/cm$^2$. During one-pass of transmission, the generation rate can be given as:

$$G = P*\alpha 1*(1-e\alpha 2L)/h\omega Nt \quad (1)$$

Where $\alpha_1$ is the percentage of the pump beam absorbed in the active region, $\alpha_2$ is the absorption coefficient of $TiO_2$ at the emission wavelength, P is the pumping pulse peak power, t is the QW thickness and *N* is the total number of the QWs, ω is the emission wavelength. Considering that the incident 355 nm light has the photon energy very close to the band gap of

GaN, the generation rate during the pulse in the six QWs (2 nm each) is $6\times10^{29}$ $cm^{-3}$ $s^{-1}$. Knowing the generation rate, the carrier density can be determined from the carrier lifetime and more specifically, the relation between the generation rate and carrier density (n) under a steady pumping can be given as:

$$n = G\,\tau\,(1 - e^{-T/\tau}) \quad (2)$$

where τ is the carrier lifetime and T is the pulse width. Note that this correlation is only valid when the carrier lifetimes are longer than the pulse width. Under low level photoluminescence measurements, the carrier lifetime is often assumed be a few hundred ps, which is much longer as the pumping pulse used in this experiment. Carrier lifetimes, however, can also be significantly affected by the high-level pumping environment and apparently the pumping densities used here are orders of magnitude higher than in the previous photoluminescence measurements. Such effect could lead to a pronounced gain saturation and that might account for output power saturation in Fig. 5(b). Unfortunately, there is yet no good quantitative consensus on the carrier lifetime dependence on the pumping level in InGaN QWs. The carrier lifetime in the InGaN red MQWs is assumed to be higher than 2 ns[29, 30, 31] and then we can estimate the threshold carrier density in the QWs is over $3.9\times10^{19}$ $cm^{-2}$ per QW. This value is close to the previously reported transparency carrier densities in InGaN blue and green lasers as well as the condition to reach Mott transition of the excitons into electron-hole plasma.[28] It is thus likely that similar QW structure can be electrically injected to the lasing level if the injection efficiency is high and carrier leakage is circumvented.

To further confirm the lasing, the polarization of the emission was investigated and measured. Based on the simulation, the fundamental mode is always transverse electric (TE)

polarized due to its apparent lower optical loss, whose direction is pinned along the direction of the stripe (*m*-plane). The degree of polarization is given as $(I_{max} - I_{min})/(I_{max} + I_{min})$, where $I_{max}$ is the maximum and $I_{min}$ the minimum optical intensity, and can be measured by adding a polarizer to the collection beam path and varying the polarizer angle. The transverse electric (TE) and transverse magnetic (TM) emission spectra from the cleaved laser bar operating above threshold are shown in Figure 6. We observe that the stimulated emission is strongly TE polarized with the degree of polarization (P), over 90%.[12] It is also noted that the TE mode emission shows multiple peaks in the spectrum, which was also reported in GaN UV optically pumped multi-mode lasing and explained by the strain in the InGaN layer.[32]

### *4. Conclusion*

In conclusion, we have demonstrated yellow stimulated emission from an optically pumped InGaN edge-emitting laser structure at room temperature. This result demonstrates high crystal quality yellow InGaN/GaN MQWs and shows great promise towards the realization of electrically injected yellow InGaN laser diodes.

### *Figures*

| Cladding and waveguiding materials | Internal loss ($cm^{-1}$) | Confinement factor |
|---|---|---|
| AlGaN/InGaN | 19 | 5.6% |
| $SiO_2/TiO_2$ | 18 | 6.2% |
| $Ta_2O5/TiO_2$ | 21 | 6.8% |

Table I. Simulated parameters for laser structures with different cladding and waveguiding materials. The internal loss and optical mode confinement factor are obtained from mode solver simulations.

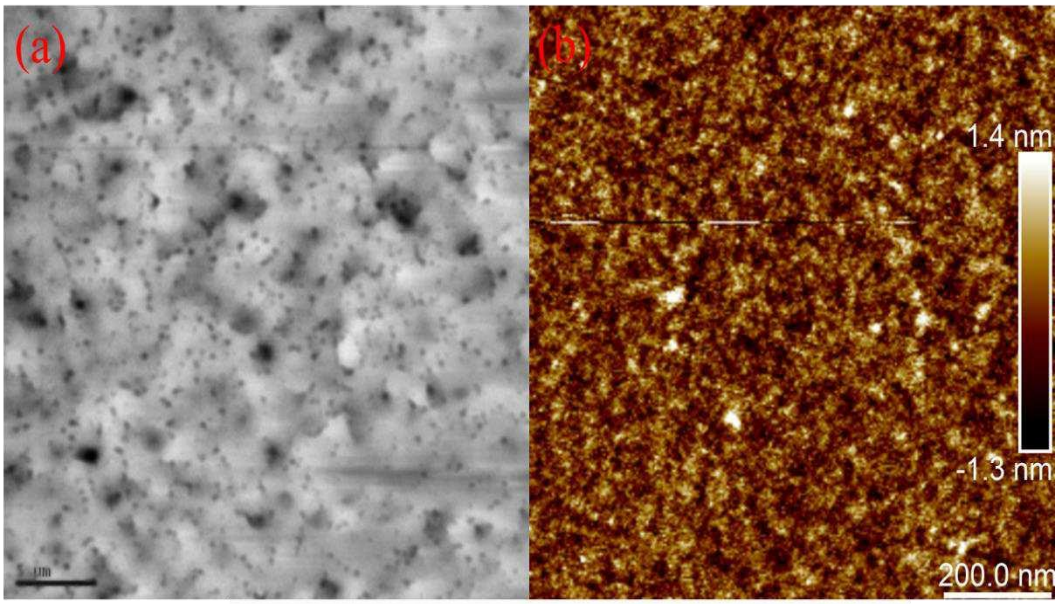


Figure. 1 (a) Monochromatic cathodoluminescence imaging of the epitaxial layer and (b) AFM image showing the smoothness of the surface before fabrication.

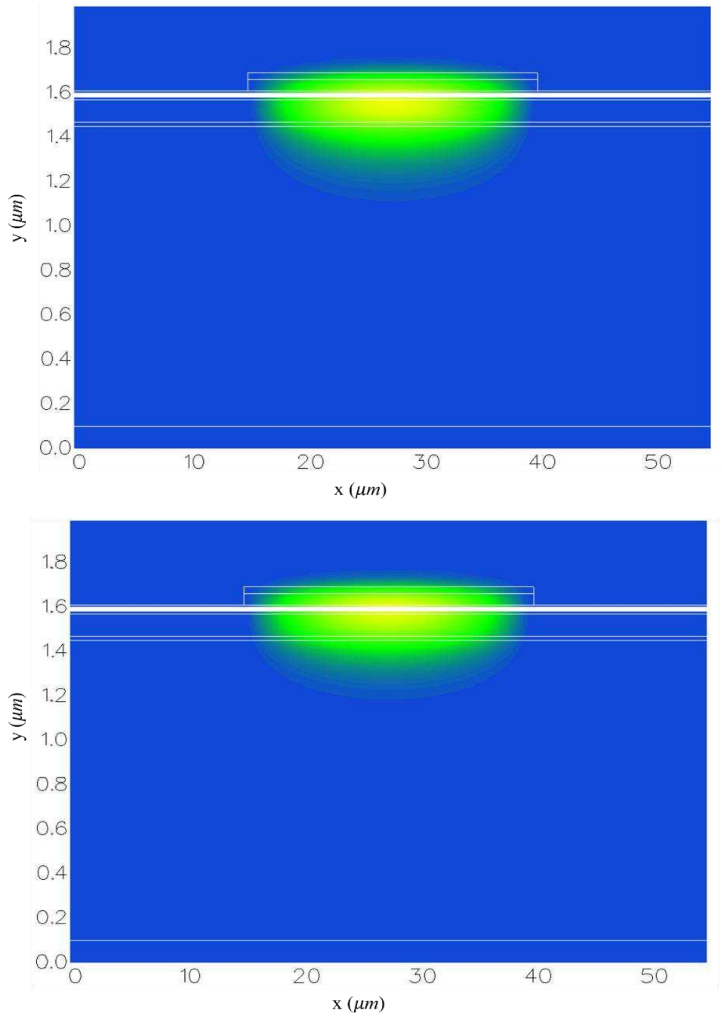


Fig. 2 Mode simulation of the slab structure with InGaN (top) and $TiO_2$ (bottom) as top waveguiding layer. Yellow area indicates the center of the mode, and on the right figure the mode is more centered at the gain-providing active region (white lines). The layers from bottom to top are GaN (substrate), AlGaN, InGaN (waveguide), InGaN/GaN QWs, $TiO_2$ and $SiO_2$.

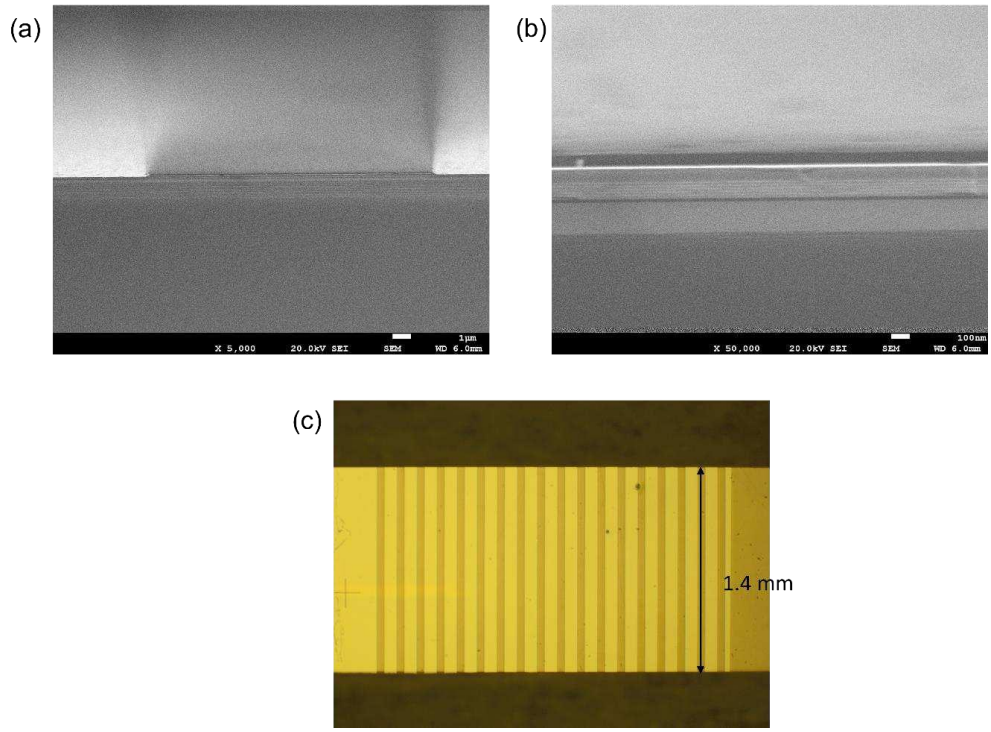


Fig. 3 (a) Cross-sectional view of a fabricated device for optical pumping; (b) magnified SEM images showing a smooth cleaved facet. (c) Microscopic top view of the device used for pumping experiment.

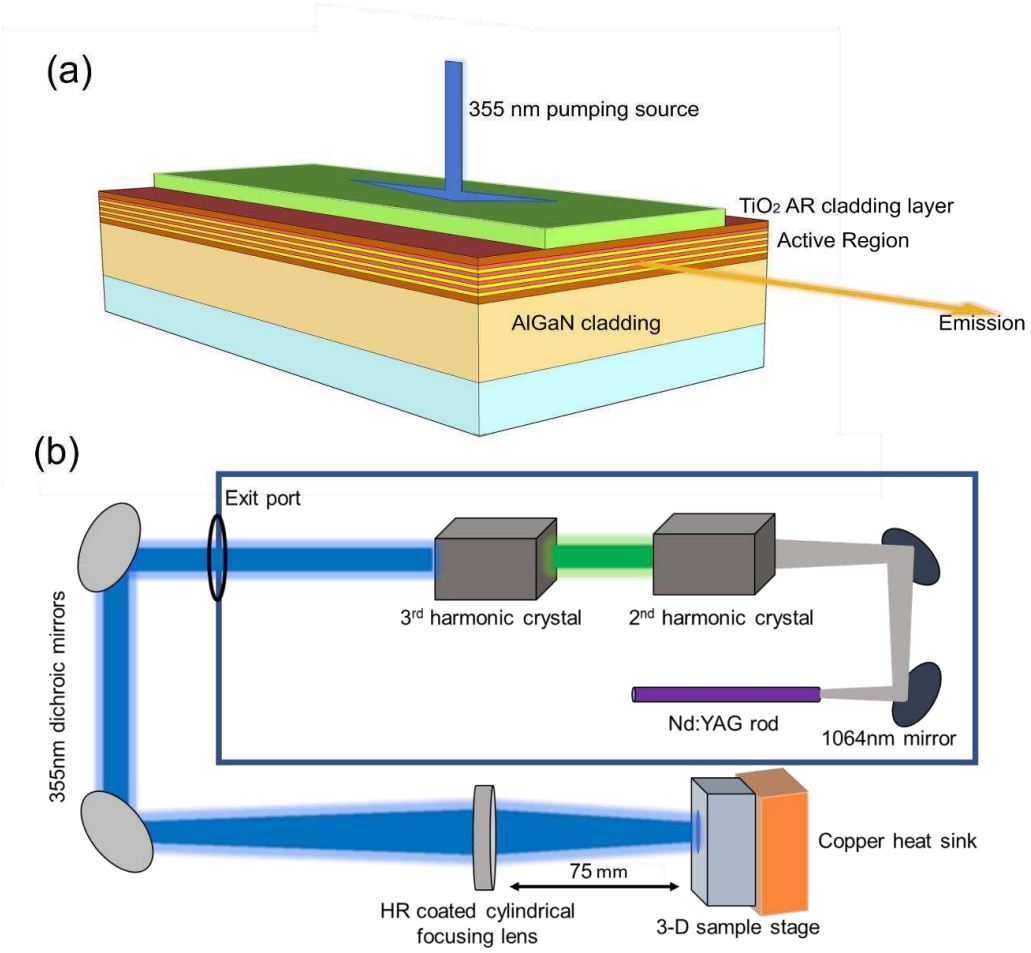


Fig. 4. (a) The pumping source setup and (b) testing setup overview.

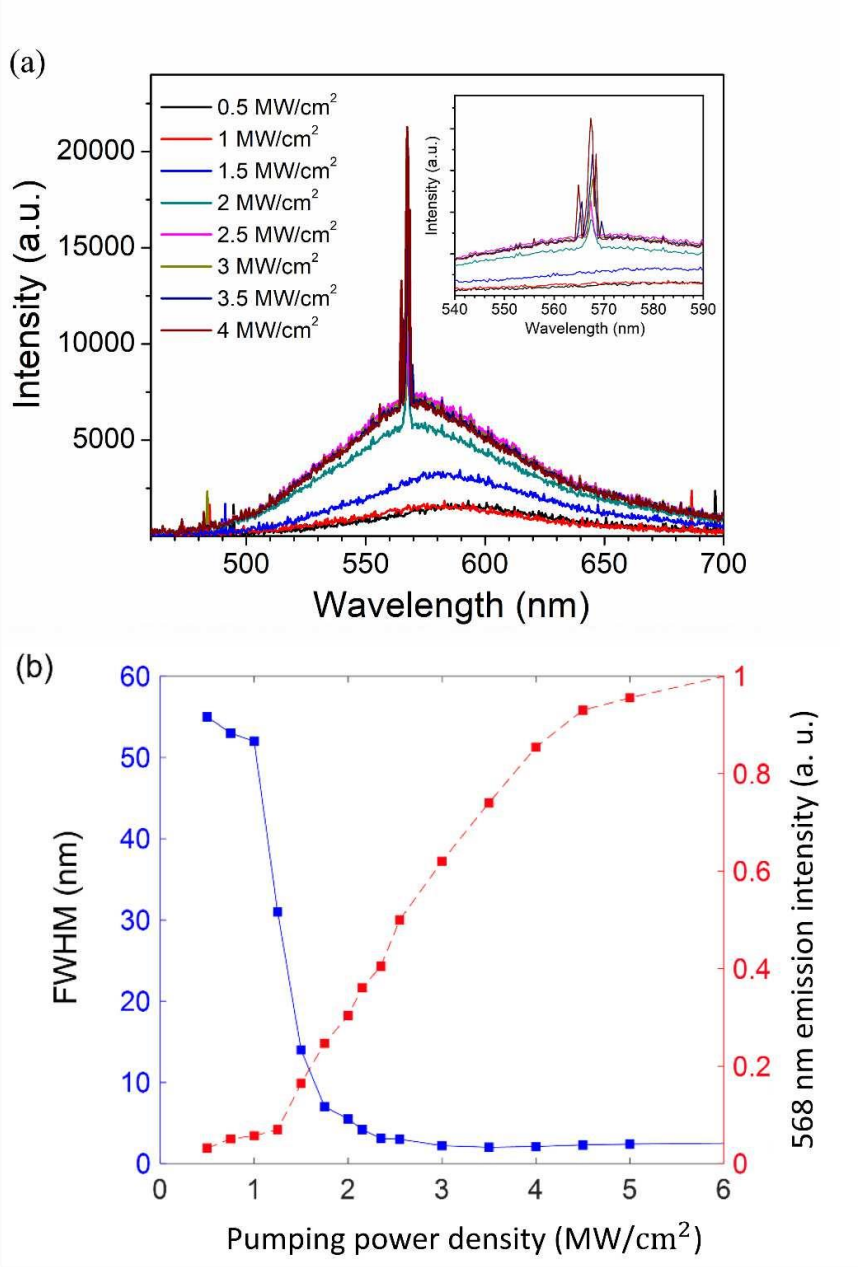


Fig. 5 (a) Spectra collected at the facet of the laser vs different pumping power densities (b) The FWHM and intensity of simulated emission as a function pumping power density. The inset of 5(a) shows the clear stimulated spectra.

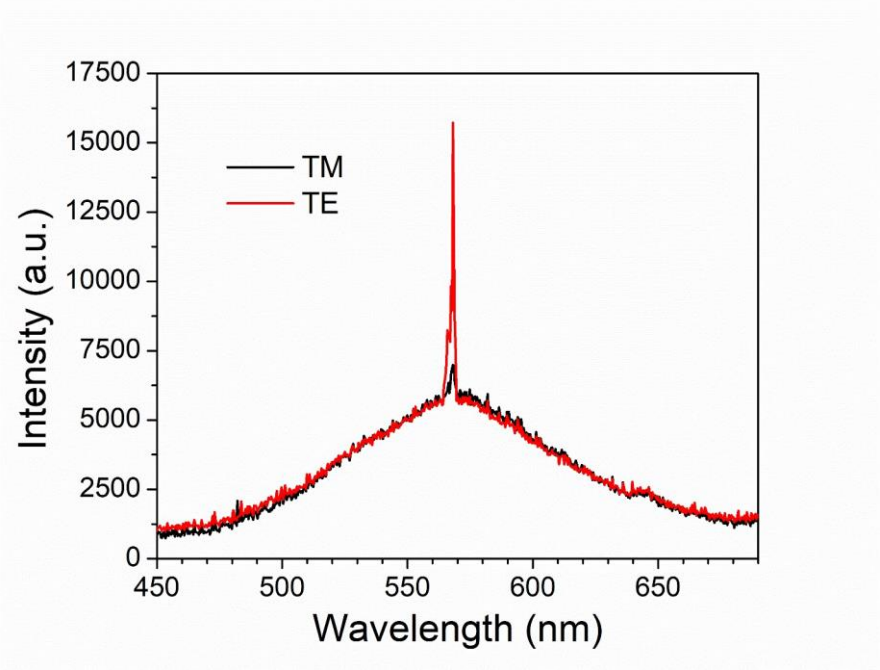


Fig. 6 Spectra of TE and TM mode at a pumping power density of 2.5 MW/cm$^2$.

**References:**

***1.*** K. Iida, T. Kawashima, A. Miyazaki, H. Kasugai, S. Mishima, A. Honshio, Y. Miyake, M. Iwaya, S. Kamiyama, H. Amano, Jpn. J. Appl. Phys. 43 L499(2004).

***2.*** J. I. Malin, J. R. Meyer, C. L. Felix, J. R. Lindle, L. Goldberg, C. A. Hoffman, and F. J. Bartoli, C.-H. Lin, P. C. Chang, S. J. Murry, R. Q. Yang, and S.-S. Pei, Appl. Phys. Lett. 68, 2976 (1996).

***3.*** T. Kitatani, K. Nakahara, M. Kondow, K. Uomi and T. Tanaka. Jpn. J. Appl. Phys. 39, L86 (2000).

***4.*** H. Hamada, R. Hiroyama, S. Honda, M. Shono, K. Yodoshi, T. Yamaguchi, IEEE J. Quantum Electron. 29, 1844 (1993).

***5.*** O. Delorme, L. Cerutti, E. Luna, G. Narcy, A. Trampert, E. Tournié, and J.-B. Rodriguez, Appl. Phys. Lett. 110, 222106 (2017).

***6.*** T. Hosoda, G. Kipshidze, G. Tsvid, L. Shterengas, G. Belenky, IEEE Photon. Technol. Lett. 22, 718(2010).

***7.*** R. Schwertberger; D. Gold; J.P. Reithmaier; A. Forchel, IEEE Photon. Technol. Lett. 14, 735 (2002).

***8.*** A. Tyagi, Y.-D. Lin, D. A. Cohen, M. Saito, K. Fujito, J. S. Speck, S. P. DenBaars and S. Nakamura, Appl. Phys. Express 1, 091103(2008).

***9.*** M. T. Hardy, C. O. Holder, D. F. Feezell, S. Nakamura, J. S. Speck, D. A. Cohen, and S. P. DenBaars, Appl. Phys. Lett. 103, 081103 (2013).

***10.*** H. Zhang, H. Li, P. Li, J. Song, J.S. Speck, S. Nakamura S. P. DenBaars, ACS Photon. 7, 1662 (2020).

***11.*** H. Li, P. Li, H. Zhang, J. Song, S. Nakamura S. P. DenBaars, ACS Appl. Electronic Materials 2, 1874 (2020).

***12.*** H. Zhang, D.A. Cohen, P. Chan, M.S. Wong, S. Mehari, S. Nakamura S. P. DenBaars, Optics Lett. 44 3106 (2019).

***13.*** Y. Mei, G. Weng, B. Zhang, J. Liu, W. Hofmann, L. Ying, J. Zhang, Z. Li, H. Yang, H. Kuo, Light Sci. Appl. 6, 16199 (2017).

***14.*** A. Sahm, N. Werner, J. Hofmann, R. Bege, K. Paschke, IEEE Photon. Technol. Lett. 30, 1878 (2018).

***15.*** Little, Christopher E. Metal vapour lasers: Physics, Engineering and Applications. 1999.

***16.*** C. V. Shank and A. Dienes, A. M. Trozzolo, J. A. Myer, Appl. Phys. Lett. 16, 405 (1970).

***17.*** K. Inagaki, K. Ohkoshi, S. Ohde, G. A. Deshpande, N. Ebihara, A. Murakami, Jpn. J. Ophthalmology 59, 21 (2015).

***18.*** X. Huo, Y. Qi, Y. Zhang, B. Chen, Z. Bai, J. Ding, Y, Wang, Z. Lu, Optics and Lasers in Engineering 134, 106207 (2020).

***19.*** T. Gasenzer, D.C. Roberts, K. Burnett, Phys. Rev. A 65, 021605 (2002).

***20.*** S. Nakamura, M. Senoh1, N. Iwasa, S. Nagahama, T. Yamada, and T. Mukai, Jpn. J. Appl. Phys. 34, L1332 (1995).

***21.*** J.-I. Hwang, R. Hashimoto, S. Saito and S. Nunoue, Appl. Phys. Express 7, 071003(2014).

***22.*** A.I. Alhassan, R.M. Farrell, B. Saifaddin, A., Mughal, F. Wu, S.P. DenBaars, S. Nakamura, and J.S. Speck, Optics Express, 24, 17868 (2016).

***23.*** P. Li, H. Li, H. Zhang, C. Lynsky, M. Iza, J. S. Speck, S. Nakamura, and S. P. DenBaars, Appl. Phys. Lett. 119, 081102 (2021).

***24.*** P. Li, A. David, H. Li, H. Zhang, C. Lynsky, Y. Yang, M. Iza, J. S. Speck, S. Nakamura, and S. P. DenBaars, Appl. Phys. Lett. 119, 231101 (2021).

***25.*** R. Anderson, D. Cohen, H. Zhang, E. Trageser, N. Palmquist, S. Nakamura, and S. P. DenBaars, Optics Express 30, 2759 (2022).

***26.*** S. Lutgen, A. Avramescu, T.Lermer, D. Queren, J. Müller, G. Bruederl, U. Strauss, Physica Status Solidi (a) 207, 1318(2010).

***27.*** L. Toikkanen, A. Härkönen, J. Lyytikäinen, T. Leinonen, A. Laakso, A. Tukiainen, J. Viheriälä, M. Bister, and M. Guina, IEEE Photon. Technol. Lett. 26, 384 (2013).

***28.*** G. Rossbach, J. Levrat, G. Jacopin, M. Shahmohammadi, J.-F. Carlin, J.-D. Ganière, R. Butté, B. Deveaud, and N. Grandjean, Phys. Rev. B 90, 201308(2014).

***29.*** D.D. Koleske, A.J. Fischer, B.N. Bryant, P.G. Kotula, J.J. Wierer, J. Cryst. Growth, 415, 57(2015).

***30.*** S. Ahmed Al Muyeed, W. Sun, M. R. Peart, R. M. Lentz, X. Wei, D. Borovac, R. Song, N. Tansu, and J.J. Wierer, J. Appl. Phys. 126, 213106 (2019).

***31.*** A. David and M. J. Grundmann, Appl. Phys. Lett. 96, 103504 (2010).

***32.*** M. Shan, Y. Zhang, T. B. Tran, J. Jiang, H. Long, Z. Zheng, A. Wang, W. Guo, J. Ye, C. Chen, J. Dai, and X. Li, ACS Photon. 6, 2387 (2019).